LUND UNIVERSITY

Lifetime Surface Phosphor Thermometry - Technique Developments, Sources of Error, and Applications

Feuk, Henrik

2023

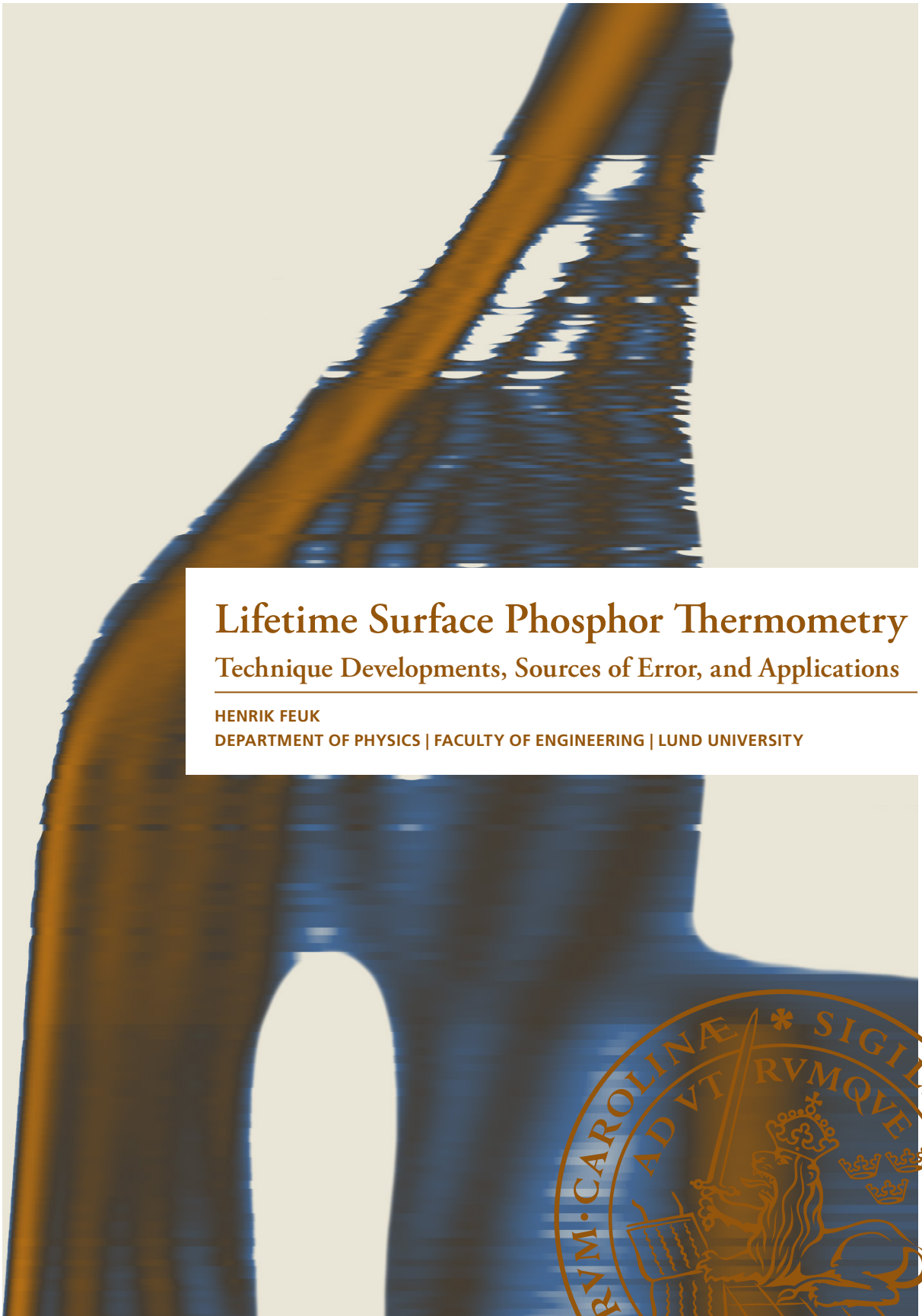

Lifetime Surface Phosphor Thermometry

Technique Developments, Sources of Error, and Applications

HENRIK FEUK
DEPARTMENT OF PHYSICS | FACULTY OF ENGINEERING | LUND UNIVERSITY

Printed by Media-Tryck, Lund 2023 NORDIC SWAN ECOLABEL 3041 0903

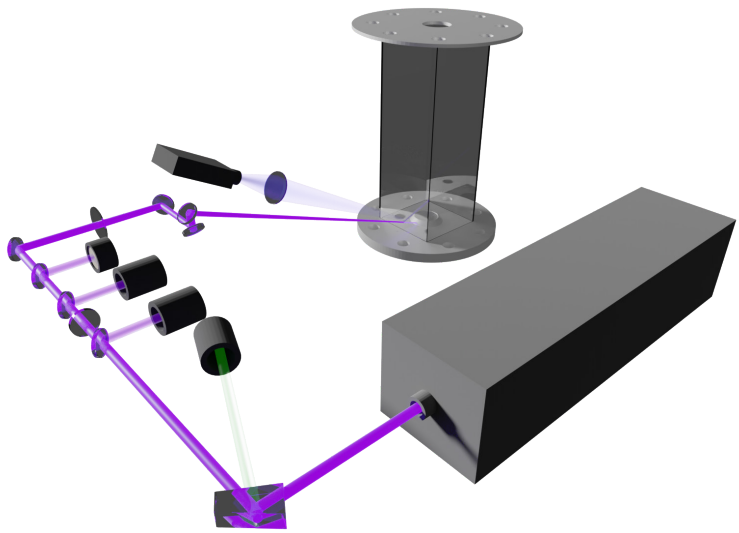

Faculty of Engineering
Department of Physics

LRCP-245
ISBN 978-91-8039-562-5
ISSN 1102-8718
ISRN LUTFD2/TFCP-245-SE

LUND UNIVERSITY

Lifetime Surface Phosphor Thermometry

Technique Developments, Sources of Error, and Applications

By Henrik Feuk

LUND
UNIVERSITY

DOCTORAL DISSERTATION

Doctoral dissertation for the degree of Doctor of Philosophy (PhD) at the Faculty of Engineering at Lund University to be publicly defended on 14th of April 2023 at 09.15 in the Rydberg hall, Department of Physics, Professorsgatan 1, Lund.

Faculty opponent

Brian Peterson

Organization: LUND UNIVERSITY

Document name: DOCTORAL DISSERTATION **Date of issue:** 2023-04-14

Author: Henrik Feuk **Sponsoring organization:**

Title and subtitle: Lifetime Surface Phosphor Thermometry

Technique Developments, Sources of Error, and Applications

Abstract:

Temperature is not only a fundamental aspect of everyday life, but it is also an essential metric for thermal conversion systems concerning efficiency, emissions, and component lifetime estimation. Therefore, a vast range of different methods to measure temperature has been developed. The technique of focus in this thesis is lifetime-based surface phosphor thermometry.

In phosphor thermometry, one leverages the changes in luminescence of materials called phosphors to measure temperature. The spectral changes can result from shifts in the relative intensity of emission lines in the spectra or shifts in emission line wavelength with temperature. In addition, changes in the lifetime of the phosphorescence signal with temperature can be utilized for thermometry. Inorganic phosphors are ceramic substances that can operate with a range of luminescence activators. Most often, the luminescence originates from trivalent lanthanide ions or transition metal ions doped in a host crystal [1].

Surface phosphor thermometry has the benefit of being a remote sensing technique, where one coats a phosphor on a surface of interest. This phosphor coating is then excited with a remote source, for example, pulsed laser light, and the phosphor luminescence is detected remotely. In this thesis, technology developments, error sources analysis, and applications of phosphor thermometry are presented. The technology developments present a high-temperature calibration system and a method for analyzing the lifetime components in the luminescence decay of phosphors in detail. An analysis of upconversion phosphors for temperature measurements beneath thermal barrier coatings and an investigation of high-temperature phosphors to 1900 K and their sensitivities to the oxygen content of the gas environment are also included in this work.

The investigations into potential error sources include how PMT nonlinearity effects can influence the measured lifetime with excitation frequency from 10 Hz up to 10 kHz. In addition, the phosphor luminescence decay time impact of high repetition excitation was also investigated and analyzed to see potential error sources for temperature measurements.

Phosphor thermometry was also used in two applications, including measuring the surface temperature of burning wood pellets and the surface temperature of a combustion nozzle in a down-scaled gas turbine combustor using hydrogen-enriched methane as fuel.

Keywords: Phosphor thermometry, thermographic phosphors, decay time, lifetime, laser-induced phosphorescence, thermometry, high temperature, surface thermometry, maximum entropy method, Kubelka-Munk

Classification system and/or index terms (if any): **Supplementary bibliographical information:**

Language: English **ISSN and key title**: 1102-8718

ISBN: 978-91-8039-562-5 (print) and 978-91-8039-563-2 (pdf)

Recipient's notes: **Number of pages**: 74

Price: **Security classification:**

Lifetime Surface Phosphor Thermometry

Technique Developments, Sources of Error, and Applications

By Henrik Feuk

LUND
UNIVERSITY

The front cover illustration is the decay time distribution of the Mg_4FGeO_6:Mn phosphor adapted from paper VIII.

The back cover illustration is the experimental setup figure adapted from paper VI.

This thesis work was financially supported by the Swedish Research Council/Swedish Energy Agency through project number 45400-01.

Faculty of Engineering, Department of Physics

ISBN: 978-91-8039-562-5 (print)
ISBN: 978-91-8039-563-2 (pdf)
LRCP: LRCP-245
ISSN 1102-8718
ISRN: LUTFD2/TFCP-245-SE

Printed in Sweden by Media-Tryck, Lund University
Lund 2023

Media-Tryck is a Nordic Swan Ecolabel certified provider of printed material. Read more about our environmental work at www.mediatryck.lu.se

MADE IN SWEDEN

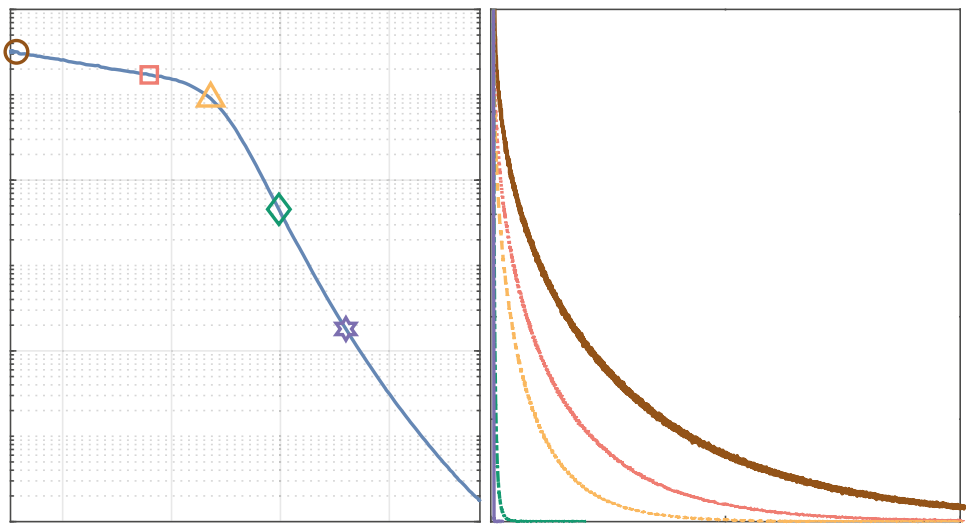

Table of Contents

Abstract

Temperature is not only a fundamental aspect of everyday life, but it is also an essential metric for thermal conversion systems concerning efficiency, emissions, and component lifetime estimation. Therefore, a vast range of different methods to measure temperature has been developed. The technique of focus in this thesis is lifetime-based surface phosphor thermometry.

In phosphor thermometry, one leverages the changes in luminescence of materials called phosphors to measure temperature. The spectral changes can result from shifts in the relative intensity of emission lines in the spectra or shifts in emission line wavelength with temperature. In addition, changes in the lifetime of the phosphorescence signal with temperature can be utilized for thermometry. Inorganic phosphors are ceramic substances that can operate with a range of luminescence activators. Most often, the luminescence originates from trivalent lanthanide ions or transition metal ions doped in a host crystal [1].

Surface phosphor thermometry has the benefit of being a remote sensing technique, where one coats a phosphor on a surface of interest. This phosphor coating is then excited with a remote source, for example, pulsed laser light, and the phosphor luminescence is detected remotely. In this thesis, technology developments, error sources analysis, and applications of phosphor thermometry are presented. The technology developments present a high-temperature calibration system and a method for analyzing the lifetime components in the luminescence decay of phosphors in detail. An analysis of upconversion phosphors for temperature measurements beneath thermal barrier coatings and an investigation of high-temperature phosphors to 1900 K and their sensitivities to the oxygen content of the gas environment are also included in this work.

The investigations into potential error sources include how PMT nonlinearity effects can influence the measured lifetime with excitation frequency from 10 Hz up to 10 kHz. In addition, the phosphor luminescence decay time impact of high repetition excitation was also investigated and analyzed to see potential error sources for temperature measurements.

Phosphor thermometry was also used in two applications, including measuring the surface temperature of burning wood pellets and the surface temperature of a combustion nozzle in a down-scaled gas turbine combustor using hydrogen-enriched methane as fuel.

Populärvetenskaplig Sammanfattning

Temperatursensorer används i allt från datorer, meteorologiska mätstationer, i kontroll av kemiska processer, förbränningssystem, och nästan alla moderna enheter man kan tänka sig. Detta visar vikten av temperatur i allt från vardagen till avancerade styrsystem. Till exempel så har yttemperaturer en fundamental påverkan på livslängd av komponenter och på verkningsgraden i förbränningsprocesser. Exakta temperaturmätningar i designstadiet kan minska utsläpp och öka verkningsgraden genom att validera modeller som används för att designa dessa system.

Elektrifiering är en viktig del för att minska det globala utsläppet av växthusgaser men 2020 stod förbränning för 90 % av den globala energiförsörjningen och 80 % av den globala energiförsörjningen kom från förbränning av fossila bränslen [2]. Enligt en rapport av International Energy Agency (IEA) så kommer förbränning av fossila bränslen fortfarande stå för cirka 14 %, och förbränning av biobränslen utgöra ungefär 20 % av den globala energiförsörjningen år 2050 i ett scenario med globalt nettonollutsläpp till 2050 [3]. I ett annat scenario där man antar att alla nationella löften om nettonollutsläpp är realiserade till fullo och i tid till 2050, utgör fossila bränslen enligt en IEA rapport 60 % av den globala energiförsörjningen och förbränning av biobränslen cirka 17 % år 2050 [3]. Med dessa relativt optimistiska scenarier, ur ett klimatförändringsperspektiv, kommer förbränning att utgöra mellan 34 och 77 % av energiförsörjningen år 2050 så forskning som kan förbättra förbränningssystem är väldigt viktigt för att minska bränsleåtgång och utsläpp. Dessa siffror på energiförsörjning inkluderar inte energilagringssystem som till exempel produktion och förbränning av ammoniak, vätgas och metallbränslen. Dessa system kan vara sätt att lagra energi som kan användas i transportindustrin eller när vind och solenergiproduktion är otillräcklig.

Med övergång till förnyelsebara bränslen i förbränningssystem så kommer även nya utmaningar. Till exempel vätgasförbränning är problematiskt på grund av dess vida brännbarhetsgräns och ammoniak är problematisk för dess snäva brännbarhetsgräns och emissionbildning. Diagnostikmetoder hjälper att förstå dessa processer som då leder till bättre designade förbränningssystem.

Yttemperaturer kan mätas med en rad tekniker såsom termoelement, IR-kameror, och tekniken som denna avhandling handlar om, laserbaserad fosfortermometri. Fosfortermometri är attraktiv för det är en beröringsfri mätteknik där en fosforbeläggning läggs på en yta av intresse. Denna fosfor är sedan belyst av en laserpuls och avger luminescens, också kallat fosforescens. Inom fosfortermometri utnyttjas förändringar i fosforescensen med temperatur för att utföra temperaturmätningar. Fokuset i denna avhandling är att använda förändringar i hur länge fosforer lyser efter belysning med temperatur för att mäta temperatur.

I denna avhandling presenteras teknikutveckling, felkällor och applikationer av fosfortermometri. I teknikutvecklingen presenteras ett högtemperatur-kalibreringssystem och en metod att i detalj analysera de livstidskomponenter som är del av fosforers luminescensfalltid. En analys av uppkonverteringsfosforer för temperaturmätningar inuti termiska barriärsbeläggningar, och en undersökning av högtemperatursfosforer till 1900 K och deras känslighet till syre andelen i gasmiljön är också en del av arbetet.

I arbetet om felkällor så presenteras hur PMT effekter kan påverka den livstiden som mäts med belysningsfrekvens från 10 Hz upp till 10 kHz för att ge bättre kunskap om potentiella felkällor. Högrepetitionsexcitation av fosforer var också undersökt och analyserat för att se potentiella felkällor för temperaturmätningar.

Fosfortermometri var också använt i två applikationer, inklusive för att mäta yttemperaturen på brinnande träpellets och yttemperaturen på en nedskalad gasturbinförbrännare med förbränning av vätgas berikat metanbränsle.

List of Papers

I. W. Weng, **H. Feuk**, S. Li, M. Richter, M. Aldén, and Z. Li, "*Temporal temperature measurement on burning biomass pellets using phosphor thermometry and two-line atomic fluorescence,*" Proc. Combust. Inst., vol. 38, no. 3, pp. 3929–3938, 2021.

II. **H. Feuk**, D. Sanned, M. Richter, and M. Aldén, "*Sources of error for single-shot PMT-based phosphor thermometry in harsh conditions*," Meas. Sci. Technol., vol. 32, no. 8, p. 84003, May 2021.

III. **H. Feuk**, S. Nilsson, M. Aldén, M. Richter, "*Investigating photomultiplier tube nonlinearities in high-speed phosphor thermometry using light emitting diode simulated decay curves*," Rev. Sci. Instrum., vol. 92, 2021.

IV. **H. Feuk**, S. Nilsson, and M. Richter, "*Automated phosphor thermometry lifetime calibration of multiple phosphors and emission lines to above 1900 K*," Meas. Sci. Technol., vol. 33, no. 12, p. 127003, 2022.

V. **H. Feuk**, S. Nilsson, and M. Richter, "*Laser excitation effects in lifetime-based high-speed phosphor thermometry*," J. Lumin., vol. 250, no. June, p. 119106, 2022.

VI. **H. Feuk**, F. Pignatelli, A. Subash, R. Bi, R. Szász, X. Bai, D. Lörstad, and M. Richter, *"Impact of Methane and Hydrogen-Enriched Methane Pilot Injection on the Surface Temperature of a Scaled-Down Burner Nozzle Measured Using Phosphor Thermometry," Int. J. Turbomachinery, Propuls. Power, vol. 7, no. 4, p. 29, 2022.*

VII. S. Nilsson, **H. Feuk**, and M. Richter, "*High Temperature Thermographic Phosphors YAG:Tm,Li and YAG:Dy in Reduced Oxygen Environments*," J. Lumin., vol. 256, no. November, p. 119645, 2023.

VIII. **H. Feuk**, S. Nilsson, and M. Richter, "*Temperature Resolved Decay Time Components of Mg_4FGeO_6:Mn using the Maximum Entropy Method*," The manuscript has been accepted for publication in Rev. Sci. Instrum. but has not been published.

IX. **H. Feuk**, S. Nilsson, and M. Richter, "*Upconversion Phosphor Thermometry for use in Thermal Barrier Coatings*," Meas. Sci. Technol., https://doi.org/10.1088/1361-6501/acc121.

Related Work

I. C. Binder, **H. Feuk**, and M. Richter, "*Phosphor thermometry for in-cylinder surface temperature measurements in diesel engines*," J. Lumin., vol. 226, p. 117415, 2020.

1 Introduction

Temperature measurements are conducted in everything from computers to meteorological measuring stations, control of chemical processes, combustion systems, and almost every modern device one can imagine. This shows the importance of temperature in everything from everyday life to advanced control systems. For example, surface temperatures fundamentally influence components' service life and the efficiency of thermal energy conversion processes, such as combustion. Therefore, accurate temperature measurements at the design stage can reduce emissions and increase efficiencies by validating models used to design these systems.

Electrification is an integral part of reducing global greenhouse gas emissions, but in 2020 combustion accounted for 90% of the global energy supply and 80% of the global energy supply came from fossil fuels combustion [2]. According to a report by the International Energy Agency (IEA), fossil fuel combustion will still represent approximately 14 %, and the combustion of biofuels will constitute roughly 20 % of the global energy supply in the year 2050 in a net-zero emission by 2050 scenario [3]. In another scenario, where one assumes that all of the current national net-zero emission pledges are fulfilled in full and on time by 2050, fossil fuels would, according to a report by IEA, still constitute 60 %, and combustion of biofuels approximately 17 % of the global energy supply [3]. With these relatively optimistic scenarios from a climate change minimization perspective, combustion will constitute between 34 and 77 % of the energy supply in 2050.

With the transition to renewable fuels in combustion systems come new challenges. For example, hydrogen combustion is problematic because of its wide flammability limit, and ammonia is problematic in exactly the opposite manner due to its narrow flammability limit. Diagnostic methods help to understand these processes, leading to better and more efficient combustion systems.

Surface temperatures can be measured with various techniques, such as thermocouples and IR cameras, but the technique of focus in this thesis is laser-induced phosphor thermometry. Phosphor thermometry is attractive because it is a remote and semi-intrusive (relatively non-intrusive) measurement technique where a phosphor coating is placed on a surface of interest. This phosphor is then excited by a laser pulse and emits luminescence, also called phosphorescence. In phosphor thermometry, changes in phosphorescence, such as spectral and temporal

characteristics with temperature, are used to perform temperature measurements. The spectral changes can result from shifts in the relative intensity of emission lines in the spectra or shifts in individual emission line wavelength with temperature. The lifetime of the phosphorescence signal also often reduces with increasing temperature, and this can be used for thermometry.

Inorganic phosphors are ceramic substances, often doped with either trivalent lanthanide ions or trivalent transition metals [1]. In this thesis, the basics of standard surface measurement techniques, including their advantages and disadvantages, are described. The fundamental working principles of thermographic phosphors are then briefly described, and the phosphor thermometry technique is then described in greater detail. This thesis uses changes in the phosphorescence lifetime with temperature to measure temperature.

After phosphor thermometry has been described and contextualized, the academic contributions of this thesis are covered. This work includes technology developments, error sources investigations, and applications of phosphor thermometry. The technology developments include a high-temperature calibration system and a method for analyzing in detail the lifetime components included in the luminescence decay of phosphors. An analysis of upconversion phosphors for temperature measurements beneath thermal barrier coatings and an investigation of high-temperature phosphors to 1900 K and their sensitivity to the oxygen content of the gas environment are also included in the work.

The error source investigations present how PMT effects can affect the measured lifetime and lead to temperature measurement errors with excitation frequencies from 10 Hz up to 10 kHz. Methods to mitigate the detector nonlinearities were also described. Phosphor excitation effects at high repetition rates was also studied to investigate potential error sources for temperature measurements.

Phosphor thermometry was also used in two applications, including measuring the surface temperature of burning wood pellets and measuring the combustion nozzle surface temperature in a down-scaled gas turbine combustor with hydrogen-enriched methane fuel.

2 Surface Temperature Measurement Techniques

In this section, a selection of relevant surface measurement techniques is described. The techniques are described in terms of their relative advantages and disadvantages.

2.1 Thermocouples

In a thermocouple, two wires of different alloys are connected at a junction. The voltage developed between these two wires depends on the junction's temperature and the alloys used in the wires. This phenomenon is called the thermoelectric or Seebeck effect [4]. Thermocouples use this effect to measure the temperature at the junction of the two wires and the wires can be made of various materials to allow different temperature measurement regions and temperature sensitivities.

Thermocouples are relatively cheap compared with the temperature measurement techniques covered later in this thesis. Using thermocouples is relatively easy and implementing them in systems is often quite easy due to their generally small size and sturdiness. They also do not require optical access to the surface temperature measurement location.

Thermocouples are relatively intrusive on the measured system as they require physical contact with the surface to allow surface measurements. Additionally, thermocouples have a response time due to their thermal inertia, making them unsuitable for temperature measurements in situations with rapid temperature changes. Also, radiation losses at high temperatures may be significant and must be corrected for accurate temperature measurements. Additionally, heat conduction through the wires of the thermocouple can affect the temperature at the junction. Thermocouples only make point measurements, and the possible temporal resolution is limited by the response time of the thermocouple in transient processes.

2.2 Pyrometry

In pyrometry, one uses the electromagnetic radiation emitted from all objects as a function of temperature. Planck's law describes this radiation:

$$R(\lambda, T) = \epsilon \cdot \frac{2hc^2}{\lambda^5} \cdot \left(\exp\left(\frac{hc}{\lambda kT}\right) - 1\right)^{-1} \tag{2.1}$$

Where ϵ is the emissivity, which is $\epsilon = 1$ for a blackbody, h is Planck's constant, c is the speed of light, T is the temperature, and k is Boltzmann's constant. The peak wavelength (λ_{max}) of this radiation shifts to shorter wavelengths with temperature increases according to Wien's displacement law:

$$\lambda_{max} = \frac{2.898 \cdot 10^{-3}}{T} \tag{2.2}$$

The total radiation intensity increases with temperature to the fourth power according to the Stefan-Boltzmann law:

$$I(T) = \epsilon \cdot \frac{2\pi^5 k^4}{15c^2h^3} \cdot T^4 \tag{2.3}$$

There are two main ways to use thermal radiation for thermometry:

- One-color pyrometers use the integrated spectral intensity within a spectral range to measure temperature. The device requires that emissivity ϵ is either assumed or given.
- Two-color pyrometers use the spectral intensity for two spectral ranges to measure temperature. The method allows for 2D measurements, and the method is also less prone to errors caused by unknown emissivity values ϵ. This is because when calculating the intensity ratio between spectral regions, the emissivity is canceled out; however, wavelength dependencies in emissivity are not easily corrected. Additionally, one needs to customize the spectral regions to achieve the highest temperature measurement sensitivity in the temperature region of interest.

Pyrometry is a remote and non-intrusive measurement technique that can give high spatial and temporal resolution. The signal strength increases with temperature and can, as a result, be used in very high-temperature environments. However, one requires optical access to the surface of interest for temperature measurements. The technique is also subject to temperature measurement errors caused by unknown or incorrect emissivity values which can be caused by the emissivity being temperature sensitive [5] and by being sensitive to both the emission wavelength and temperature [6].

Lower temperatures may be difficult to measure due to lower signals, as described in Equation (2.3). Background light will also negatively impact surface temperature measurements. For example, emissions from hot neighboring surfaces that reflect off the surface of interest would superimpose on the desired signal and result in inaccurate temperature measurements. Also, the thermal radiation from sooty flames is problematic. The technique is also sensitive to the absorption of electromagnetic radiation in the gas environment between the surface and the detector. For example, water and CO_2 absorb IR radiation very effectively. Although this thesis will not cover pyrometry more, blackbody radiation will be discussed in the context of an interfering background signal for phosphor thermometry measurements.

2.3 Thermal Paints

Thermal paints use irreversible color changes in the paint due to high-temperature exposure for temperature measurements. The purpose is to get the maximum operating temperature as a 2D map of the surface of interest. Historically, this temperature assignment relied on a skilled operator to assign temperature by optical inspection [7]. The technique requires no optical access for temperature measurements. Instead, the thermal paints are inspected after temperature exposure. Thermal paints can therefore be applied on moving objects, for example, turbine blades in a gas turbine, without additional experimental complexity.

The technique has poor temperature resolution compared to the other temperature measurement methods covered in this thesis. Thermal paints can only be used once as they undergo permanent changes after temperature exposure. Thermal paints are not only maximum temperature sensitive but also temperature exposure time-sensitive, meaning that a given color can be a result of a multitude of temperatures and exposure times [7]. Therefore, the calibration of the thermal paints requires knowledge of exposure time for accurate temperature measurements [7]. Additionally, one cannot know when the maximum temperature was achieved for the thermal paint as the temperature measurement technique has no temporal resolution. Even though the paints are often thin, typically thinner than 40 μm [7], some thermal insulation of the surface may occur due to the coating.

2.4 Surface Phosphor Thermometry

Surface phosphor thermometry, the technique of focus in this thesis, is based on a three-part process. First, the phosphor needs to be applied on the surface of interest to allow surface temperature measurements. A phosphor is typically a host crystal

doped with a transition metal ion or lanthanide ion activator [8]. Second, the phosphor must be excited to a higher energy state by, for example, UV radiation or X-rays [1]. In the work performed as part of this thesis, excitation was exclusively performed with pulsed laser light. Third, one needs to collect the luminescence from the phosphor, often referred to as phosphorescence, and leverage the temperature-sensitive characteristics of the phosphor for thermometry.

The most often utilized characteristics of phosphorescence are the lifetime change of the decay and the relative changes in the intensity of phosphor luminescence in different spectral regions with temperatures. Concerning these distinct characteristics, each phosphor has sensitivity in different temperature regions [9]–[11]. Therefore, an appropriate phosphor in terms of temperature sensitivity in the correct region must be selected.

The phosphor thermometry technique is semi-invasive in the same way thermal paint is, as a phosphor coating on the surface of interest is needed, but thinner coatings will affect the measured system less. Due to the three-part process of phosphor thermometry, it is a relatively expensive temperature measurement technique. However, it has the potential for high-temperature precision and high temporal resolution temperature measurements in the temperature range from cryogenic to 2000 K [12], [13], although not with the same phosphor. Optical access is required for temperature measurements as phosphor luminescence is a function of the current temperature the phosphor experiences. Additionally, surface phosphor thermometry can be used on moving components [14], [15]. Even though it is a relatively mature technique, phosphor thermometry still requires a skilled operator for accurate and precise temperature measurements. The phosphor thermometry measurement technique will be described in greater detail as part of this thesis.

3 Thermographic Phosphors

Phosphors are materials that emit luminescence after excitation by some source of external energy [8]. The first use of phosphors that may come to mind is the use of phosphors for lighting purposes, where they are used in LEDs and fluorescent lamps. The temperature dependence of phosphors, such as a decreased quantum efficiency with temperature, which is undesirable in those applications, can be leveraged for temperature determination [1]. Paul Neubert was the first to suggest using phosphors to measure temperature, with his two patents filed in 1932 [16]. In the more modern era, between 1980-2000, the basic techniques still used to this day were developed, including excitation with lasers and LEDs and using the lifetime and intensity ratio methods for thermometry [16].

The fundamental theoretical basis of phosphor luminescence is described in this chapter with a focus on concepts relevant to phosphor thermometry.

3.1 Fundamentals

Most phosphors consist of a host crystal doped with either a lanthanide ion or a transition metal ion activator [8]. In the doping process, ions in the crystal host are replaced by the dopants, also called activators or luminescence centers, for their luminescence characteristics. For example, doping the activator dysprosium into the host crystal Yttrium Aluminum Garnet (YAG), one replaces a small fraction of yttrium ions with Dy. YAG:Dy (2 %) means dysprosium replaces 2 % of the yttrium ions.

Lanthanides, which often take the form of trivalent lanthanides (Ln^{3+}) when doped in a host crystal, are interesting dopants in phosphors for phosphor thermometry because they fill the 4f orbitals, which are shielded by the $5s^2$ and $5p^6$ electrons [8]. The shielding leads to the electrons in 4f orbitals not participating in chemical bonding, which makes them relatively unaffected by the host crystal properties and behave similarly to free ions when doped in crystals at low concentrations. The relatively minor impact of the host crystals on Ln^{3+} makes 4f to 4f transitions result in sharp emission lines resembling those of free ions, as seen in Figure 3.1 (a) [17]. 4f to 4f transitions of free ions are forbidden by the Laporte selection rule, leading

to a relatively long decay time after excitation. This selection rule can relax for ions in crystals, which can increase the probability of transitions.

The lanthanides consist of the rare-earth metals, excluding yttrium and scandium. Lanthanum's trivalent lanthanide ion has no electrons in the 4f shell, and lutetium^{3+} has a filled 4f subshell, meaning they do not have 4f to 4f transitions. Table 3.1 shows an overview of the trivalent lanthanides with 4f to 4f transitions. The ground state configurations in Table 3.1 was determined according to Hund's rule.

Table 3.1: Overview of Lanthanides with 4f to 4f transitions and their trivalent cations' ground state electron configuration. [Xe] is Xenon's electron configuration. * - if less than half-filled and + if more than half-filled. The vertical arrows indicate spin.

Ions	Electron configuration	4f electrons orbitals, l							Ground state configuration			
		+3	+2	+1	0	-1	-2	-3	S=$\sum s$	L=$\sum l$	J=$(L\pm^{*}S)$	$^{(2S+1)}L_J$
Ce^{3+}	[Xe] $4f^1$	↑							1/2	3	5/2	$^2F_{5/2}$
Pr^{3+}	[Xe] $4f^2$	↑	↑						1	5	4	$^3H_4$
Nd^{3+}	[Xe] $4f^3$	↑	↑	↑					3/2	6	9/2	$^4I_{9/2}$
Pm^{3+}	[Xe] $4f^4$	↑	↑	↑	↑				2	6	4	$^5I_4$
Sm^{3+}	[Xe] $4f^5$	↑	↑	↑	↑	↑			5/2	5	5/2	$^6H_{5/2}$
Eu^{3+}	[Xe] $4f^6$	↑	↑	↑	↑	↑	↑		3	3	0	$^7F_0$
Gd^{3+}	[Xe] $4f^7$	↑	↑	↑	↑	↑	↑	↑	7/2	0	7/2	$^8S_{7/2}$
Tb^{3+}	[Xe] $4f^8$	↑↓	↑	↑	↑	↑	↑	↑	3	3	6	$^7F_6$
Dy^{3+}	[Xe] $4f^9$	↑↓	↑↓	↑	↑	↑	↑	↑	5/2	5	15/2	$^6H_{15/2}$
Ho^{3+}	[Xe] $4f^{10}$	↑↓	↑↓	↑↓	↑	↑	↑	↑	2	6	8	$^5I_8$
Er^{3+}	[Xe] $4f^{11}$	↑↓	↑↓	↑↓	↑↓	↑	↑	↑	3/2	6	15/2	$^4I_{15/2}$
Th^{3+}	[Xe] $4f^{12}$	↑↓	↑↓	↑↓	↑↓	↑↓	↑	↑	1	5	6	$^3H_6$
Yb^{3+}	[Xe] $4f^{13}$	↑↓	↑↓	↑↓	↑↓	↑↓	↑↓	↑	1/2	3	7/2	$^2F_{7/2}$

The coulombic interaction due to electron-to-electron repulsion in the 4f orbitals represents the largest separation in the spectra of the Ln^{3+}, typically in the order of 10^4 cm^{-1} [17]. These terms split into J-levels due to spin-orbit coupling with separations on the order of 10^3 cm^{-1} [17]. The free ion energy levels of Ln^{3+} are described by $^{(2S+1)}L_J$, where 2S+1 is the total spin multiplicity, L is the total orbital angular momentum, and J is the total angular momentum. Additionally, for Ln^{3+} doped in crystals, there is also crystal field splitting which is in the order of 10^2 cm^{-1} [17].

Figure 3.1 shows the emission spectra of YAG:Dy and a Dieke energy level diagram [10], [18]–[20] of Dy^{3+}. Ceramic crystals like YAG are stable and can often withstand high temperatures, which are desirable for high-temperature phosphor thermometry. Therefore, lanthanides doped in ceramic hosts are particularly well suited for high-temperature phosphor thermometry [21], [22]. The interaction between host crystal effects and the dopant is complex, and there are ways of modeling, but predicting the temperature dependence of phosphors is challenging

[22]. Judd-Ofelt theory is one method to predict the spectra of lanthanide ions doped in crystals [17], [23], [24].

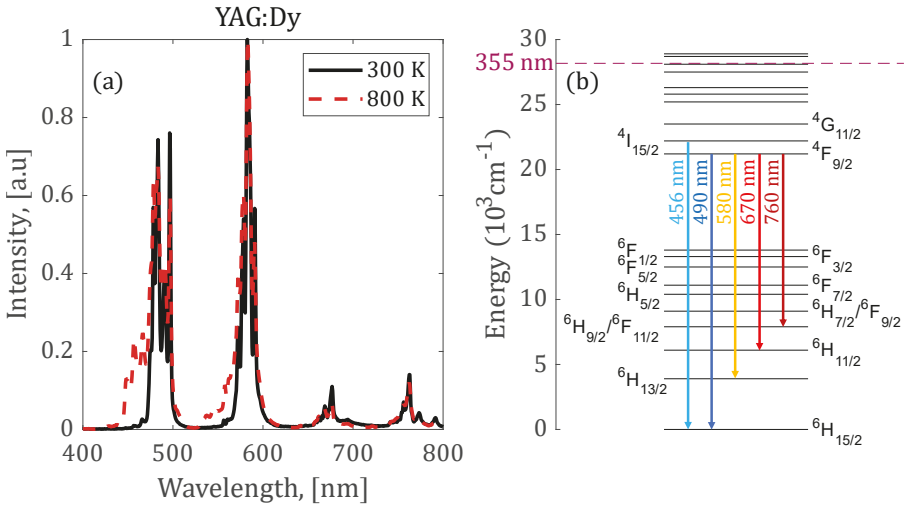

Figure 3.1: Emission Spectra of YAG:Dy in (a) and Dieke energy diagram of Dy^{3+} in (b). Emission spectra at two temperatures are shown for YAG:Dy to highlight the relative increase in emissions around 456 nm. The Dieke diagram only indicates a selection of emission lines in (b), and the energy corresponding to 355 nm light is also shown. Dy^{3+} energy levels and transition assignments are taken from [25], [26].

Transition metal atoms have an incompletely filled d subshell in their second outermost shell, and their outermost shell has two electrons in the s subshell. Their ions typically lose the electrons in the s subshell in the outermost shell. Therefore, the optically active electrons in the d subshell are not well shielded from crystal effects in the host. This results in the luminescence of phosphors doped with transition metals being more affected by the crystal field of the host crystal than lanthanide-doped phosphors [8]. The emission lines of transition metal doped phosphors are wider than lanthanide emissions with 4f to 4f orbital transition, as seen in Figure 3.2 (a) for Mg_4FGeO_6:Mn (MFG), due to the greater influence by the host crystal.

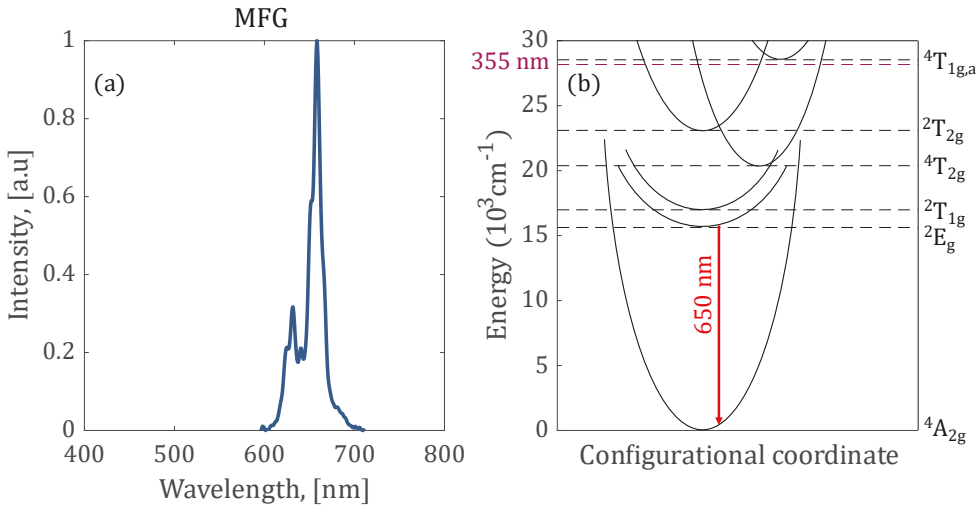

Figure 3.2: Emission Spectra of Mg_4FgeO_6:Mn (MFG) in (a) and the approximate configurational coordinate model for the [Ar] $3d^3$ configuration $Mg_4FGeO_6:Mn^{4+}$ in (b). The configurational coordinate model in (b) is adapted from [27].

Once phosphors have been excited to a higher energy level, they can deexcite through several avenues. The two main categories are radiative and non-radiative relaxation. With radiative relaxation, a photon is emitted in the deexcitation process. With non-radiative relaxation, no emission of photons occurs during deexcitation. A simplified configurational diagram shown in Figure 3.3 can qualitatively explain many phosphor-related phenomena. Figure 3.3 shows five scenarios for deexcitation. In the first scenario, the system initially relaxes to the lowest vibrational level of the excited state. From there, it relaxes to a high vibrational level of the ground state with a photon emission. The number of electrons in higher vibrational energy levels (n_e) compared with the number of electrons in the ground state (n_g) can be derived from the Boltzmann distribution [21]:

$$n_e = n_g \cdot \exp\left(-\frac{\Delta E}{kT}\right) \tag{3.1}$$

Where ΔE is the energy difference of the excited state from the ground state. From this high vibrational level, it deexcites non-radiatively to the lowest vibrational level of the ground state. The non-radiative transitions in scenario one result in the Stoke shift of the light emission. Scenario two, in Figure 3.3, is similar to the first scenario, but the radiative deexcitation takes place to a lower vibrational energy level in the ground state, resulting in more energetic photon emission. In scenario three, there is no photon emission as the deexcitation occurs through a common intersection point for the two states. In scenario four, the deexcitation is also non-radiative, and the deexcitation goes through the charge transfer state (CTS), which connects the crystal field with the activator's energy levels [28]. In scenario five, the vibrational

levels of both states overlap, and deexcitation occurs through non-radiative vibrational relaxation. The probability of the non-radiative transition occurring in scenarios three to five increases with temperature as higher vibrational energy levels in the ground state are populated. This is because excitation from higher vibrational energy levels in the ground state can reach higher vibrational energy levels in the excited state. Additionally, the probability of multi-phonon non-radiative transition between energy levels increases with temperature which explains the decay time sensitivity to temperature of some phosphors [22]. Not all these described factors may be present in all phosphors, but the simplified phenomena lead to the general behavior of phosphors where the probability of non-radiative deexcitation increases with temperature.

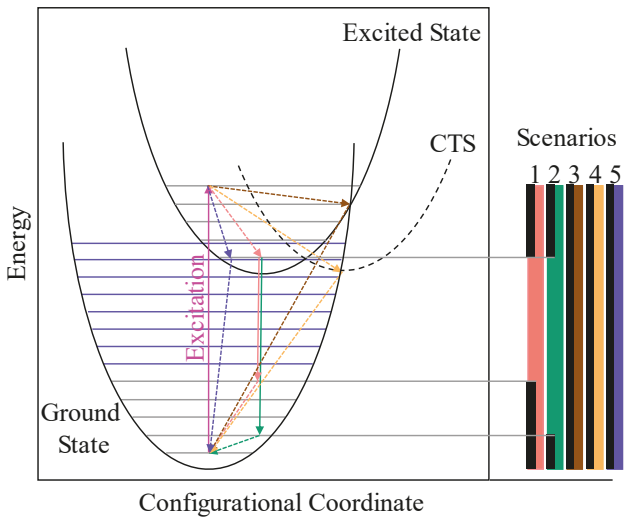

Figure 3.3: Configurational diagram of excitation from the ground state to the excited state and possible deexcitation pathways. The horizontal lines in the states represent different vibrational energy levels. Dashed lines represent non-radiative transitions and solid vertical lines represent radiative transitions.

After excitation to a higher energy level, the population in the excited state will decay over time, and as a result, the radiative emissions will also decrease over time. A mono-exponential decay is often used to approximate the decay of phosphor luminescence:

$$I(t) = I_0 \cdot e^{-\frac{t}{\tau}} \tag{3.2}$$

Where $I(t)$ is the emission intensity at time t for a decay time of τ and a peak intensity of I_0. The decay time, τ, of the phosphor luminescence can be written as [8]:

$$\tau = \frac{1}{W_R + W_{NR}} \tag{3.3}$$

Where W_R is the radiative and W_{NR} is the non-radiative transition probabilities. The temperature dependence of the non-radiative transitions results in the temperature sensitivity of thermographic phosphors [22].

3.2 Lifetime Changes

The increase in the non-radiative transition probability W_{NR}, with increasing temperature, leads to, in general, shorter decay time at higher temperatures, as described in Equation (3.3). The luminescence quantum efficiency of phosphors, therefore, also decreases as W_{NR} increases as less energy is converted to photon emissions. As a result, the integrated luminosity and the decay time decrease with increasing temperature. An example of the decrease in measured decay time and integrated luminosity is given for MFG in Figure 3.4 below.

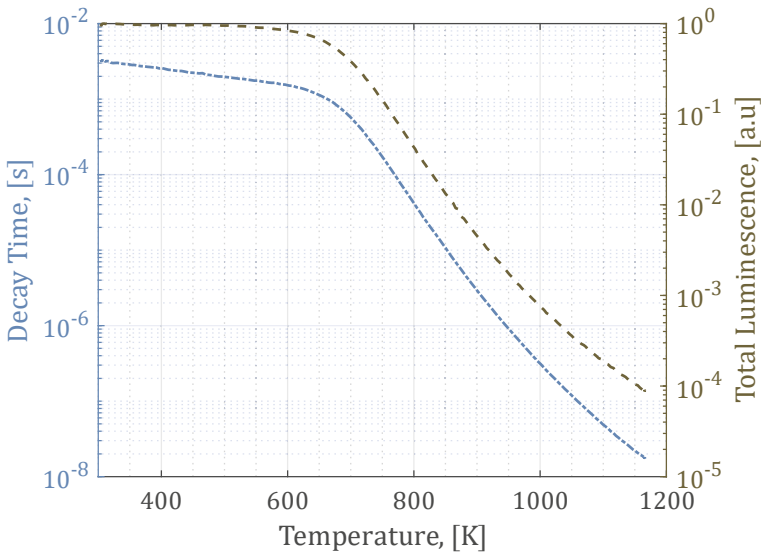

Figure 3.4: Measured decay time and integrated luminosity of MFG.

The onset of sensitivity for MFG occurs at approximately 650 K, where both the integrated luminosity and decay time start to reduce significantly. For a mono-exponential decay curve, the relationship between integrated luminosity and the decay time is:

$$I_{tot} = \int_0^{\infty} I_0 \cdot e^{-\frac{t}{\tau}} dt = I_0 \cdot \tau \tag{3.4}$$

Where I_0 is the same as in Equation (3.2), and τ is the decay time. At 1150 K, the integrated luminosity is only 0.01% of the integrated luminosity around 300 K for MFG. However, it is important to note that the peak signal value measured by the PMT used to collect the phosphorescence has a much weaker temperature trend, as seen in Figure 3.5. Consequently, the peak intensity of the phosphorescence (I_0) in Equation (3.4) is approximately constant with temperature, and the reduction in integrated luminosity is primarily due to a reduction in decay time for MFG. The phosphorescence peak intensity trend with temperature varies between thermographic phosphors and Figure 3.5 only serves as an example.

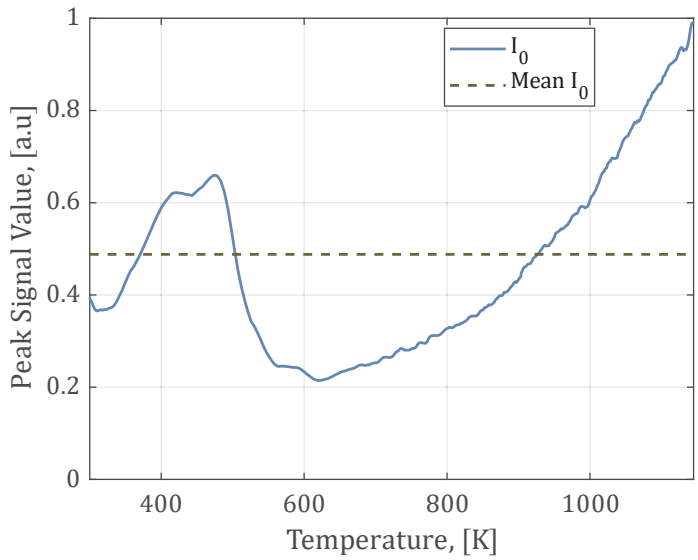

Figure 3.5: Peak phosphorescence intensity of MFG, I_0. The mean value of the peak signal level in the plotted temperature range is also shown.

3.3 Spectral Changes

As shown in Figure 3.1 (a), the emission spectra of phosphors can change with temperature and this can be leveraged for thermometry. A range of temperature induced changes can occur in the emission spectra of phosphors. One of them, as demonstrated in Figure 3.1 (a) and Figure 3.6 going from S2 to S1, is thermalization, where the population of higher vibrational energy levels according to the Boltzmann distribution [21] allows for more transitions to take place. A more significant

population in higher vibrational energy levels could, in turn, increase the emission intensity of an emission line with increasing temperature.

The general trend of broadening of the emission lines, as demonstrated in Figure 3.6, going from S2 to S4, can be the result of several mechanisms, including Doppler broadening, higher vibrational energy levels being more populated at higher temperatures, and broadening, due to expansion of the host crystal lattice [29].

Shifting the emission line to shorter, like BAM:Eu^{2+} emission [30], and longer wavelengths, which is more common, like ZnO:Zn [31], with increasing temperature can also occur. Going from S2 to S3 in Figure 3.6 demonstrates a shift of the emission line to shorter wavelengths. Thermal expansion of the host crystal with temperature can cause these shifts [29].

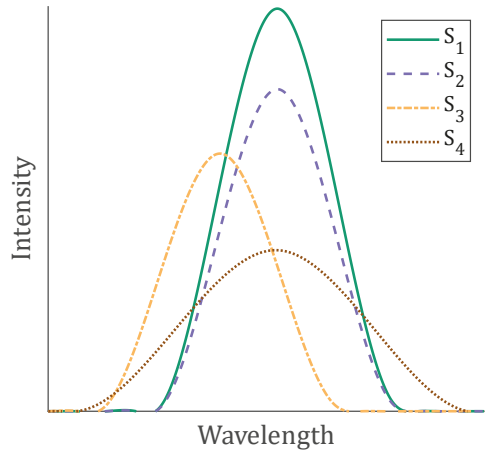

Figure 3.6: Demonstration of the basic principles for the intensity ratio method where S_1 to S_4 illustrate shifts in the emission spectra.

In general, the integrated luminosity of a phosphor reduces with temperature, as shown for MFG in Figure 3.4. Therefore, the intensity of all emission lines decreases with temperature, with a few exceptions, like some emission lines of La_2O_2S:Eu [28].

4 Phosphor Thermometry

Phosphor thermometry has been applied in a range of combustion applications, including on burning material [9], in biology applications [32], and more [1]. In phosphor thermometry, one leverages the change in the luminescence properties of phosphors to make temperature measurements. The two most used methods in phosphor thermometry are the lifetime and the spectral intensity ratio methods. In the lifetime method, one uses the change in the lifetime of the phosphor luminosity for temperature measurements. With the intensity ratio method, one uses relative changes in spectral regions of the phosphor luminescence for temperature measurements. Common for both methods is the need to use phosphors that are temperature sensitive in the relevant temperature region for the given technique.

Applying a phosphor coating to the surface of interest is required for both techniques for temperature measurements. One approach is to mix the phosphor powder with a binder appropriate for the temperature range that the coating will experience [33]–[36]. The mixture is often applied like a paint with an airbrush. The benefit of this application method is that it is relatively simple to apply the phosphor coating, and it is generally very well attached if applied correctly. Phosphors can also be applied with methods used to apply Thermal Barrier Coatings (TBC), including atmospheric plasma spray (APS), electron beam physical vapor deposition (EBPVD), and suspension plasma spray (SPS) [37], [38]. Sol-gel process could also be used to apply phosphors on surfaces.

The phosphor needs to be excited to induce phosphor luminescence. Standard excitation methods include pulsed lasers, LEDs, and diode lasers. Pulsed lasers are generally the more expensive option, but the often short pulses makes it so that one can study fast decay phenomena that could otherwise be obscured by the fall time of LEDs. Pulsed laser sources can have a wide range of repetition rates from singles of Hz to 100 kHz, which should be customized based on the desired temporal resolution. LEDs are more cost-effective than pulsed lasers, and the excitation frequency of an LED is often simpler to vary than pulsed laser sources. However, the often quite long rise times and fall times of LEDs limit the maximum repetition rate and lowest decay times that can be measured. It is also possible that the phosphorescence decay time puts limitations on the repetition rate possible without incomplete decay before the next excitation pulse. In such situations, one can look at the phase-shift between the phosphor signal and excitation signal [39] or look at the ratio of the minimum and maximum signal of the incomplete decay curves [40].

4.1 Lifetime Method

With the lifetime method, one uses the change in the lifetime of the phosphor luminosity with temperature for temperature measurements. Figure 4.1 (a) shows MFG's decay time for a range of temperatures. The temperature sensitivity is relatively low in the temperature region from 300 K to 650 K. Past this point, the decay time starts to reduce considerably more with temperature. For example, from 700 K to 1000 K, the decay time (seen in Figure 4.1 (a)) reduces from $5 \cdot 10^{-4}\ s$ to $3 \cdot 10^{-7}\ s$. This is a 1,700 times reduction in decay time over a 300 K temperature range. Therefore, the mean temperature sensitivity of the phosphor in this region is 2.5 %/K. The sensitivity of a phosphor is defined as:

$$S_\tau = -\frac{\frac{\partial \tau}{\partial T}}{\tau} \cdot 100\ \% \tag{4.1}$$

MFG's high temperature sensitivity shows the potential temperature resolution possible with phosphor thermometry. Figure 4.1 (b) shows the shape of the longer decay components of MFG's decay curves at a range of temperatures.

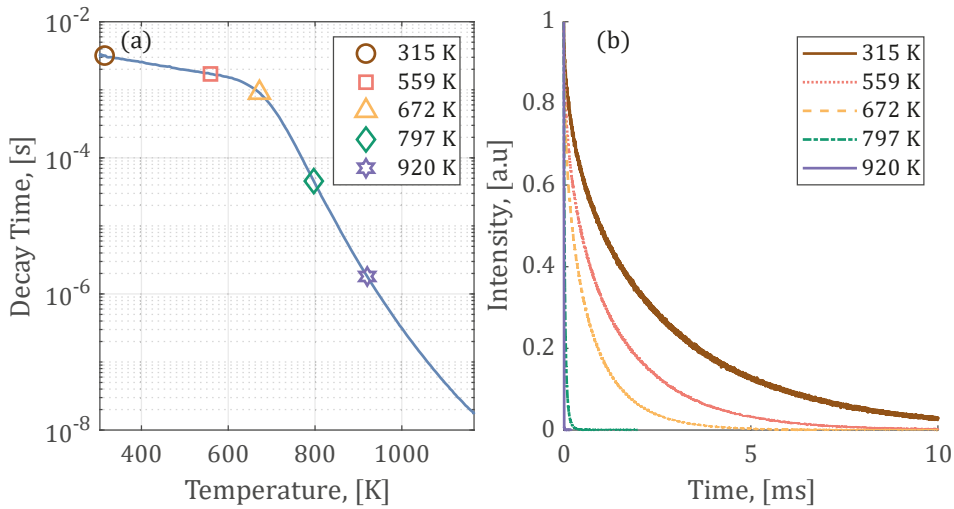

Figure 4.1: MFG's decay time and decay curve at different temperatures. Calibration curve in (a) and example decay curves at different temperatures for MFG in (b).

The lifetime behavior of MFG in Figure 4.1 (a) shows the general lifetime trend of many phosphors. At low temperatures, the decay time is insensitive to temperature. When reaching the onset of sensitivity temperature, the decay time starts to reduce with temperature, and lifetime-based phosphor thermometry measurements are most sensitive above that temperature. The onset of sensitivity temperature and lifetime sensitivity to temperature vary between phosphors. Additionally, some phosphors

have the same decay time for all emission lines, like YAG:Dy, seen in Figure 5.5, and other phosphors, like La_2O_2S:Eu have different lifetimes for their emission lines [41].

For 2D measurements, one could use high-speed cameras to sample a decay curve multiple times during its decay over an entire surface [42]–[45]. One could also use a dual-gate method with a double-shutter camera or high-speed camera to sample the decay curve twice to measure the decay time [46], [47]. Both these methods are more restrictive in decay times that they can measure compared to a PMT. With a high-speed camera, the shortest resolvable lifetime is limited by the repetition rate of the camera. For the dual-gate method, the exposure and timings of the gates need to be optimized for the decay time range [46], [48]. The choice of 2D or point measurements depends on the desire for 2D measurements and equipment availability.

Phosphor thermometry measurements could be conducted with single-shot measurements and with averaging. With averaging one can achieve higher signal-to-noise-ratio (SNR) than single-shot measurements which may be necessary in situations with a weak phosphorescence signal. However, single-shot measurements allow for higher repetition rate temperature measurements.

For point measurements, a PMT, photodiode, or alternative luminescence intensity measurement device is used to collect the phosphor luminescence. The signal from these devices is often digitized by an oscilloscope or similar and saved for later decay time analysis. There are a variety of sources of error for incorrect temperature measurement with systems like these, including detector nonlinearities, phosphor sensitivities to gas oxygen concentration, phosphor pressure sensitivities, and phosphor sensitivities to laser pulse energy. This thesis will explore some of these factors in more detail. Additionally, the manner in which a phosphor lifetime is analyzed and measured from a decay curve is not always trivial. Poor decay time fitting practices could result in poor temperature measurement precision and accuracy.

4.1.1 Lifetime Fitting

Determining lifetime from a decay curve is not always trivial due to the multi-exponential nature of many phosphors [49]–[51]. One relatively simple approach is described in Figure 4.2. First, any constant background signal is identified and removed from the decay signal. Then the maximum value of the decay curve, I_0, and the point in time where the peak occurred are determined. The fitting window start, and endpoints are set as percentages of this maximum peak value, I_0, with I_{start}= start percentage and I_{end}= end percentage of fitting. With the fitting window determined, an initial decay time, τ_0, decay intensity, a_0, and offset, c_0, value are calculated using a rapid lifetime determination (RLD) method [52], [53]. The fitting

window and initial estimates of fitting parameters are then sent to a trust-region-reflective least-squares least-square algorithm to get the final decay time.

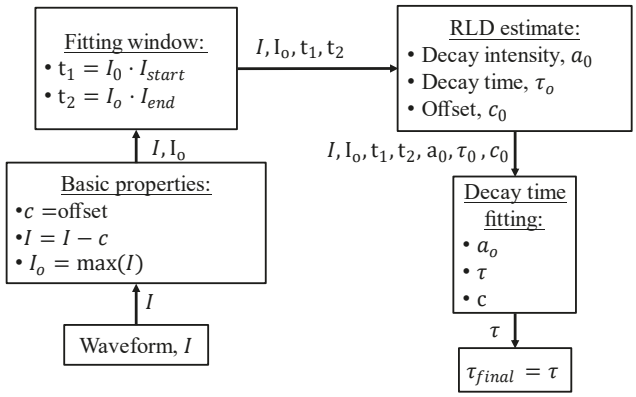

Figure 4.2: Basic operation of the non-iterative decay time fitting algorithm.

This decay curve fitting algorithm is relatively quick and robust for decay time determination. An example of fitting a decay curve to MFG at 900 K can be seen in Figure 4.3 below, with I_{start}= 30 % and I_{end}= 1 % as the start and end point intensity values for decay time fitting.

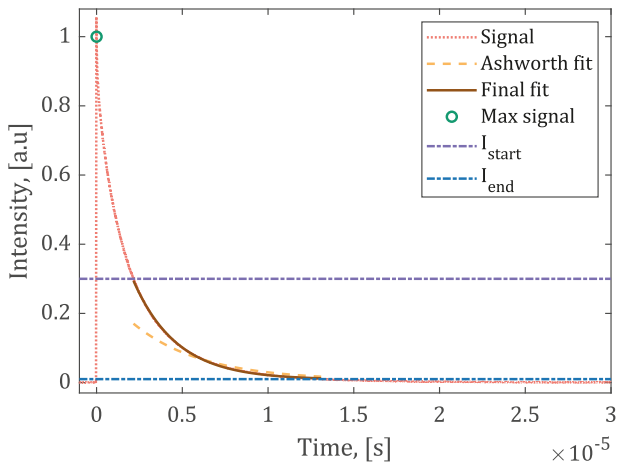

Figure 4.3: The decay curve of MFG at 900 K with RLD fit and the final fit using the non-iterative algorithm.

The downside of the non-iterative fitting window algorithm just described is that it does not minimize the impact of multi-exponential decay on the decay time analysis unless the user specifies I_{start} and I_{end} to regions where the decay curve is dominated by a single lifetime, which is usually in the later parts of the decay curve

[54], [55]. An iterative window method can be used, which shifts the decay curve fitting boundaries to regions where the measured decay time is more likely to be dependent on a single decay component [54], [55]. Figure 4.4 describes the basic operation of the fitting algorithm.

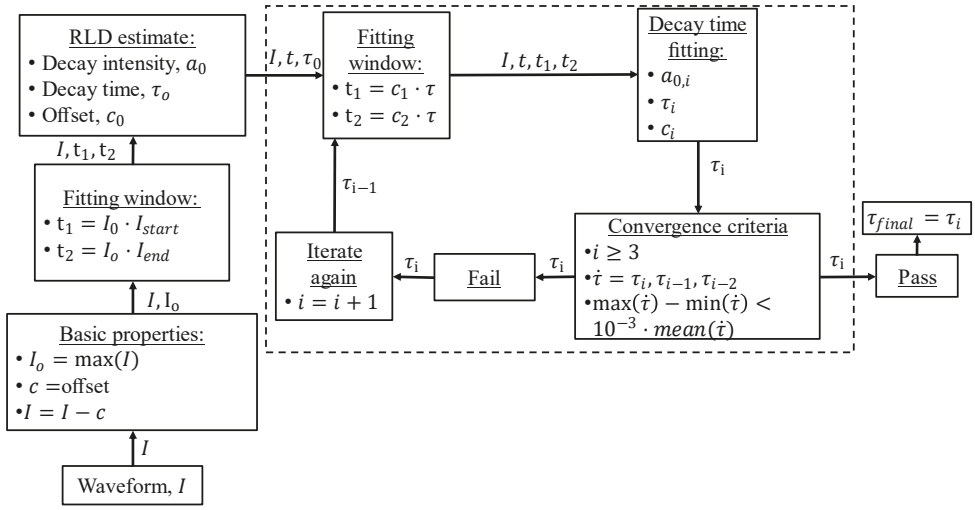

Figure 4.4: Basic operation of iterative fitting window algorithm. Based on work in [54], [55].

The start of the iterative fitting window algorithm in Figure 4.4 is the same as the non-iterative fitting algorithm described in Figure 4.2. The main difference is that the algorithm iterates the fitting window and measured decay time until it finds a stable decay time solution. The time from the peak of the decay curve until the start of the fitting window is $t_1 = c_1 \cdot \tau$ and the time at the end of the fitting window is $t_2 = c_2 \cdot \tau$. Where τ is the decay time estimate from the RLD fit for the first iteration and all other iterations, τ is the measured decay time from the previous iteration. The fitting window parameters c_1, c_2, were set to $c_1 = 1$ and $c_2 = 4$ (as recommended in [54]) for the decay curve-fitting on the MFG data in Figure 4.5. The $c_1 = 1$ and $c_2 = 4$ values mean that the decay curve fitting is performed one measured decay time after the decay curve peak until four measured decay times after the decay curve peak. The decay curve fitting convergence criteria used as part of the work in this thesis was that the maximum difference in measured decay time between the past three iterations, $\dot{\tau}$, needs to be smaller than 0.1 % of the mean of the three past iterations, as described in Figure 4.4.

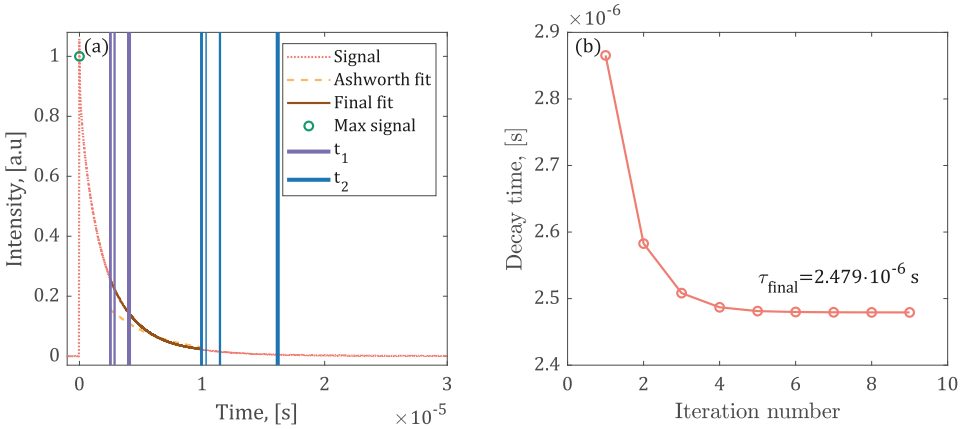

Figure 4.5: Decay curve of MFG at 900 K with iterative decay time fitting window with an intentionally long initial decay time estimate. The lines for t_1 and t_2 become thinner and more transparent as the iteration number increases. The broadest lines with no transparency are the t_1 and t_2 boundaries based on the RLD estimate.

Figure 4.6 shows the situation where the initial RLD estimate is artificially made to give a shorter decay time than the final decay time. The two examples in Figure 4.5 and Figure 4.6 shows that the iteratively adapted fitting window algorithm can find the same decay time with different initial guesses of the decay time from the RLD algorithm.

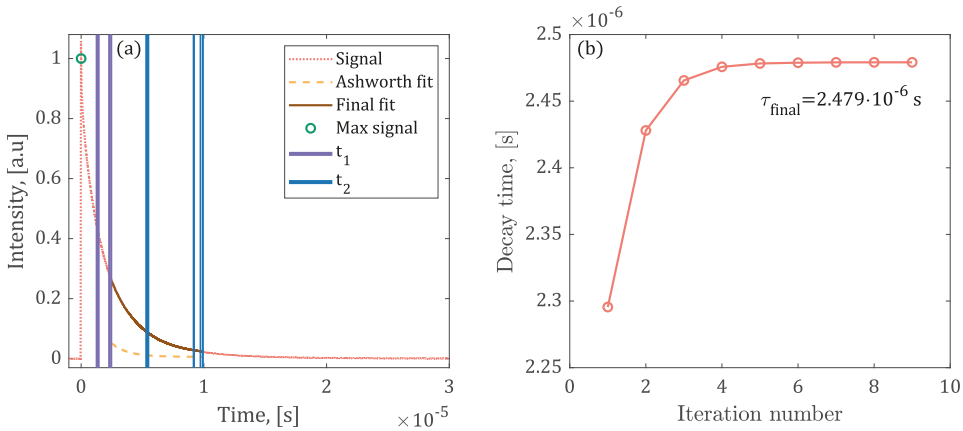

Figure 4.6: Decay curve of MFG at 900 K with iterative decay time fitting window with an intentionally short initial decay time estimate. The lines for t_1 and t_2 become thinner and more transparent as the iteration number increases. The broadest lines with no transparency are the t_1 and t_2 boundaries based on the RLD guess.

Bi-exponential decay time fitting is sometimes used for decay curve fitting. This is quite common practice for YAG:Dy [49], [50], Figure 5.6 shows the reason for this. However, this thesis did not use bi-exponential fitting to simplify the determination of a singular decay time of the phosphor luminescence, as ultimately, one desires a

single lifetime to correspond to a unique temperature for lifetime phosphor thermometry.

4.1.2 Sampling of Decay Curves

Using the maximum available sampling rate is highly advantageous for precise temperature measurements and measurements made with low SNR. However, data with many sample points can make data management more troublesome as 25 MS waveforms results in a lot more data than using 2.5 kS waveforms. In addition, the additional computational time needed to analyze decay curves with high sampling rate is significant. However, as the determination of a single decay time of a decay curve is generally very fast, increasing the evaluation time of 100 decay curves from 10 seconds to 10 minutes can be a worthwhile sacrifice for increased measurement precision.

To demonstrate this fact, a 3.3 ms mono-exponential decay curve was simulated, and the fitting window was set from the peak of the decay curve until 19 ms later. A fixed fitting window was used because it becomes difficult to separate the decay curve features from noise for decay curves with low sampling rates, and high noise. As a result, accurate peak determination which is needed to decide the start and end of the decay time evaluation becomes more complex, and for this to not impact the presented results, they were predefined. Therefore, the simulations presented here only illustrate errors induced in the decay curve fitting procedure.

The noise was added as Gaussian noise to an artificial 25 MS decay curve. With this, SNRs from 1 to 400 were tested. In addition, sampling rates from 1.25 GS/s to 50 kS/s and total decay curve sampling between 25 MS and 1 kS were tested with ten decay curves variants for each configuration. All ten variants of each sampling rate and SNR combination used a unique random number generation (RNG) seed for the noise addition to the data. A total of ten unique seeds were used for all configurations and different SNRs were achieved by using different standard deviations with the same RNG seed. Different sampling rates were achieved by down sampling the highest sampling decay curve.

The results in Figure 4.7 show that with 1 SNR, the 25 MS data had a percentage standard deviation in the decay time of 0.1 %, whereas the 250 kS data had 1 %. The data in Figure 4.7, in general, suggests that a two-order-of-magnitude increase in sampling rate results in an order-of-magnitude reduction in the standard deviation. This shows the potential increase in measurement precision by just changing the decay curves' sampling rate with no other experimental difficulties.

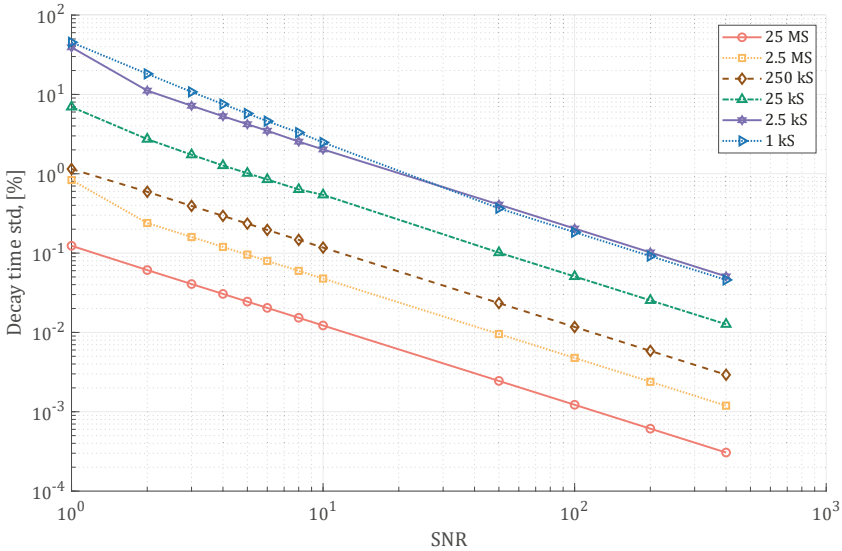

Figure 4.7: Impact of SNR on the standard deviation of the measured decay time. The percentage standard deviation is relative to the 3.3 ms simulated decay curve.

The results in Figure 4.8 show that with 1 SNR, the 25 MS data had a percentage error in the mean decay time of 0.03 %, whereas the 250 kS data had 0.6 %. The data in Figure 4.8, in general, suggests that a two-order-of-magnitude increase in sampling rate results in an order-of-magnitude reduction in the decay time measurement error. This shows the potential increase in measurement accuracy by just changing the decay curves' sampling rate, with no other experimental difficulties.

The simulated scenarios illustrate the potential benefit of high sampling rate decay curves, but one could also reduce the oscilloscope's bandwidth to reduce the influence of high-frequency noise. However, this requires prior knowledge from the operator of the lifetimes to be measured, as limiting the oscilloscope's bandwidth could also distort the shape of captured decay curves.

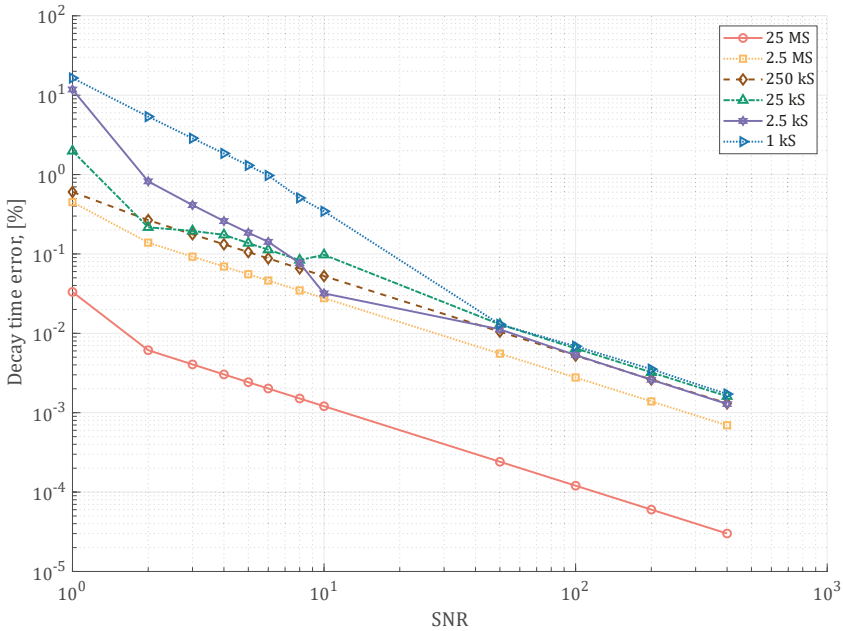

Figure 4.8: Impact of SNR on the error of the measured decay time. The percentage error relative to the 3.3 ms simulated decay curve is used.

One could also do a moving average of the captured waveforms with post-processing to reduce the computational time to analyze decay curves while reducing noise's influence. Using a moving average may achieve similar benefits as a high sampling of decay curves, but ultimately, capturing high sample rate decay curves gives the user much more flexibility in the decay time analysis process. The influence of SNR and sampling rate was also studied on a decay curve of MFG captured at room temperature, where artificial noise was added to the decay curve to achieve different SNRs. That study resulted in a similar result as in Figure 4.7 and Figure 4.8, but the trends presented here were clearer, probably primarily due to MFG's multiexponential decay. Therefore, only the simulated data was presented as a part of this thesis.

4.2 Spectral Intensity Ratio Method

With the intensity ratio method, one uses relative intensity changes in spectral regions of phosphor luminescence for temperature measurements. This is demonstrated in Figure 4.9 (b) with a fictional phosphor emission spectrum, and different spectral changes in the spectral regions I_1 and I_2. Note that the temperatures T_1 to T_4 in Figure 4.9 (b) only show possible spectral variations and

not a typical change in emission spectra with temperature for phosphors. The intensity method works by assigning an intensity ratio of the two spectral regions, I_1/I_2 to a unique temperature through a calibration, as demonstrated in Figure 4.9 (a).

Going from T_1 to T_2, the change in emission intensity of one spectral region, in this case I_2 relative I_1, with temperature is used for thermometry. Emissions in spectral regions could increase with temperature relative to other emission lines, as the 456 nm emission of YAG:Dy (Figure 3.1 (a)) or decrease in intensity with temperature. Going from T_1 to T_3, the emission line in the I_2 spectral region shifts and reduces in intensity with temperature such that part of the emission is outside of the spectral integration region. Going from T_1 to T_4, the emission line in the spectral region, I_2, broadens with temperature and leads to a lower intensity in the spectral region.

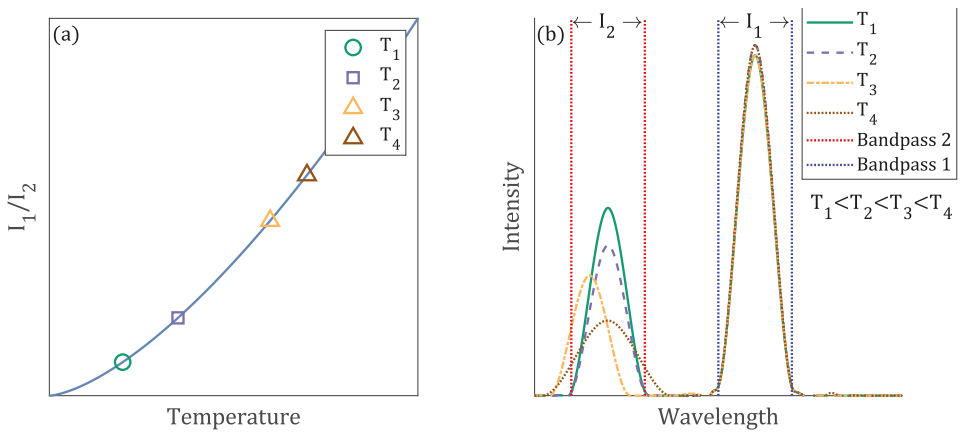

Figure 4.9: Demonstrates the basic principles for the intensity ratio method for thermometry. A calibration curve is shown in (a), and (b) shows a simplified emission spectrum.

The intensity ratio method requires one to capture the phosphor luminescence in two or more spectral regions. This can be performed using two cameras, each with a different bandpass filter [29], [56], [57]. One then excites the phosphor-coated surface, looks at the phosphor luminescence intensity in the two spectral regions and calculates the ratio of the intensities. To measure surface temperature from the intensity ratio, one needs a calibration curve like in Figure 4.9 (a). The intensity method more easily allows for 2D measurements than the lifetime method. However, the technique is, in general, more background sensitive as even a constant optical background signal which is equal in both spectral regions I_1 and I_2 in Figure 4.9 (b) will lead to an incorrect intensity ratio and therefore measurement temperature error. Although the uncertainty of intensity ratio measurements has improved in recent work [58], [59], the lifetime method is the focus of this thesis due to its superior ability to measure higher temperatures [12], [60].

5 Technique Developments

This section is a summary of the phosphor thermometry technique developments that were undertaken as a part of this thesis. The work includes the development of a high-temperature lifetime calibration system, characterizing the multi-exponentiality of phosphors, evaluating phosphors for temperature measurements beneath a Thermal Barrier Coating (TBC), and evaluating high-temperature phosphors, including their oxygen sensitivity. This chapter covers material from papers IV, VII, VIII, and IX.

5.1 High-Temperature Thermographic Phosphor Calibrations

The difficulty of high-temperature measurements is partly due to strong blackbody background radiation with which the phosphor luminescence competes in the signal collection. Blackbody radiation follows Planck's law and Wien's displacement law. Together they state that the radiation intensity scales with the temperature to the fourth power and that the central radiation wavelength shifts to shorter wavelengths with higher temperatures. Figure 5.1 shows this effect in the 300 nm to 1000 nm spectral region (the spectral region studied for phosphors in this thesis). For example, at 2000 K, the blackbody radiation at 456 nm is 55 % less than the blackbody radiation at 483 nm, which is why YAG:Dy's emission around 456 nm is so superior for high-temperature lifetime thermometry. See Figure 3.1 (a) for the emission spectra of YAG:Dy.

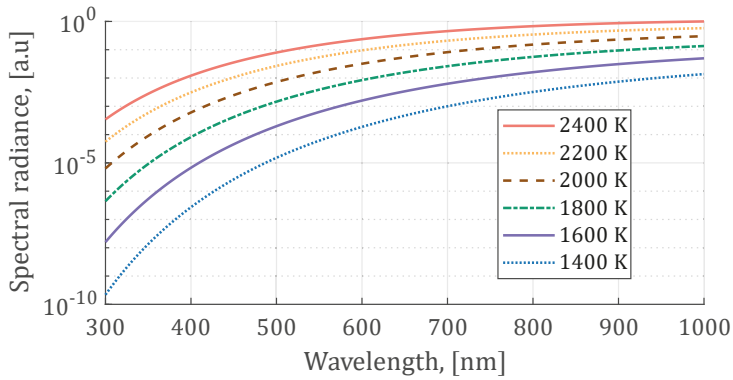

Figure 5.1: Blackbody radiation intensity versus wavelength for different temperatures. Note that the y-axis uses a logarithmic scale.

Blackbody radiation worsens the SNR of the decay signal and leads to lower precision of temperature measurements. Additionally, if the background is too strong, it may negatively affect detector linearity and lead to errors in decay time measurement. The fact that, having phosphor luminescence in the blue region is critical at higher temperatures is also demonstrated in Figure 5.2, which shows lines of constant blackbody radiation intensity. For example, the blackbody radiation intensity at 2000 K and 350 nm is as intense as the blackbody radiation at 1200 K and 700 nm.

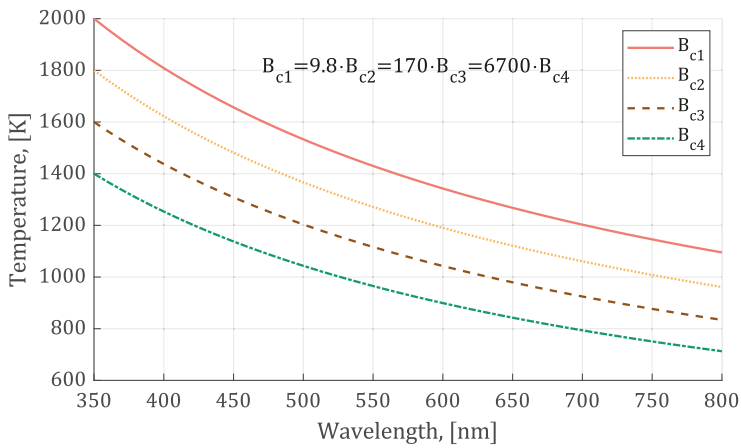

Figure 5.2: Lines of constant blackbody radiation intensity. Note that the plot also shows each line's relative blackbody radiation intensity (B_C).

Investigating potential thermographic phosphors and their emission lines for lifetime phosphor thermometry measurements can become time-consuming,

especially when a conventional calibration method is used where the operator needs to wait until the phosphor sample is in thermal equilibrium for each data point [1], [10], [61], [62]. Abou Nada et al. [63] developed an automatic calibration routine that significantly improved the time efficiency of phosphor calibrations and reduced errors caused by interpolating between calibration points due to increased data density. This automated routine can potentially cut the experimental time by a factor of four. However, this method could only calibrate one phosphor at a time.

A new automated calibration procedure for high-temperature lifetime calibrations was introduced in work as part of this thesis. This method allows for the simultaneous calibration of multiple phosphors, with the option of investigating multiple emission lines of each phosphor. The experimental setup is depicted in Figure 5.3 and the galvo system was used to focus the excitation laser on the desired spot on the alumina oxide substrate to excite the desired phosphor as demonstrated by the zoomed-in alternative view in Figure 5.3. Different emission lines of phosphors could be investigated with the motorized filter wheel in front of the PMT. The reference temperatures for the phosphor calibrations were measured by thermocouples attached into indentations of the phosphor coated substrate.

Phosphor lifetimes have previously been calibrated up to nearly 2000 K using doped crystals [12] and phosphors in powder form [62], but the maximum temperature in a surface coating was 1800 K prior to this work [35]. The work presented in this thesis is unique in that multiple surface-coated phosphors and emission lines can be calibrated simultaneously to temperatures above 1900 K using an automated process.

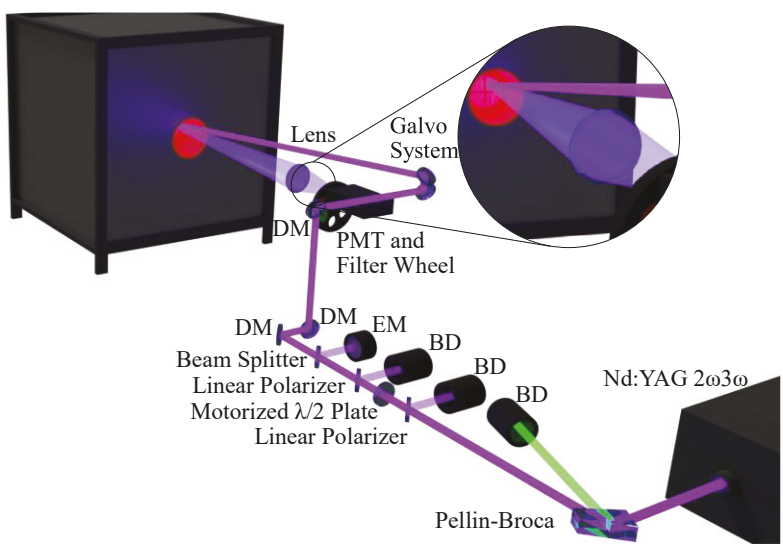

Figure 5.3: Experimental setup. EM—energy meter, DM—dichroic mirror, BD—Beam Dump. The zoomed-in alternative view image shows how the galvo system excites the phosphor in the upper right quadrant.

This method has the main advantage of ensuring that all phosphors and emission lines are calibrated with the same environmental history. As a result, this is a powerful tool for comparing phosphor sensitivities to environmental factors. The motorized λ/2 plate allows for custom laser energy for all configurations, which may be useful when each phosphor requires a different excitation energy. The algorithm procedure is depicted in Figure 5.4, and the MATLAB program is available at https://doi.org/10.17605/OSF.IO/XTZN4 [64]. Although the program was written to work with the equipment used in this thesis, it could be modified to work with other types of lab equipment, and the overall methodology could be useful to phosphor thermometry practitioners.

Following data collection, the decay time was measured using an in-house developed decay curve analysis software. The program analyzes the data collected from the previously mentioned data collection program, measures the decay time and generates plots to provide the user with an instant overview of the decay curve fitting quality. The MATLAB program is available at https://doi.org/10.17605/OSF.IO/XTZN4 [64].

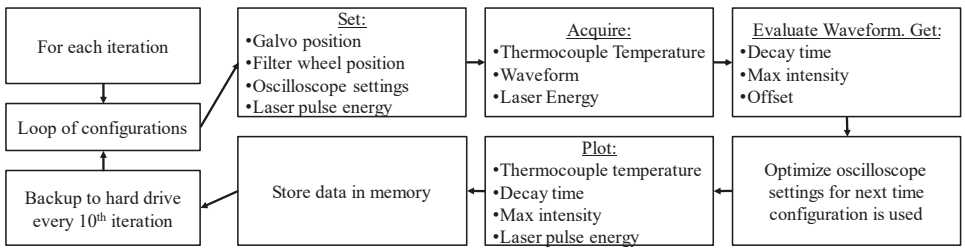

Figure 5.4: Flowchart of the algorithm used to acquire decay curves from multiple phosphors and emission lines. The order of the phosphors and emission line configurations can be randomized for each iteration.

The calibration data of YAG:Dy and YAG:Dy,Ce in Figure 5.5 includes calibrations of multiple emission lines from each phosphor from the same automated calibration run. Note the significant differences in background radiation due to Planck radiation for the various bandpass filters.

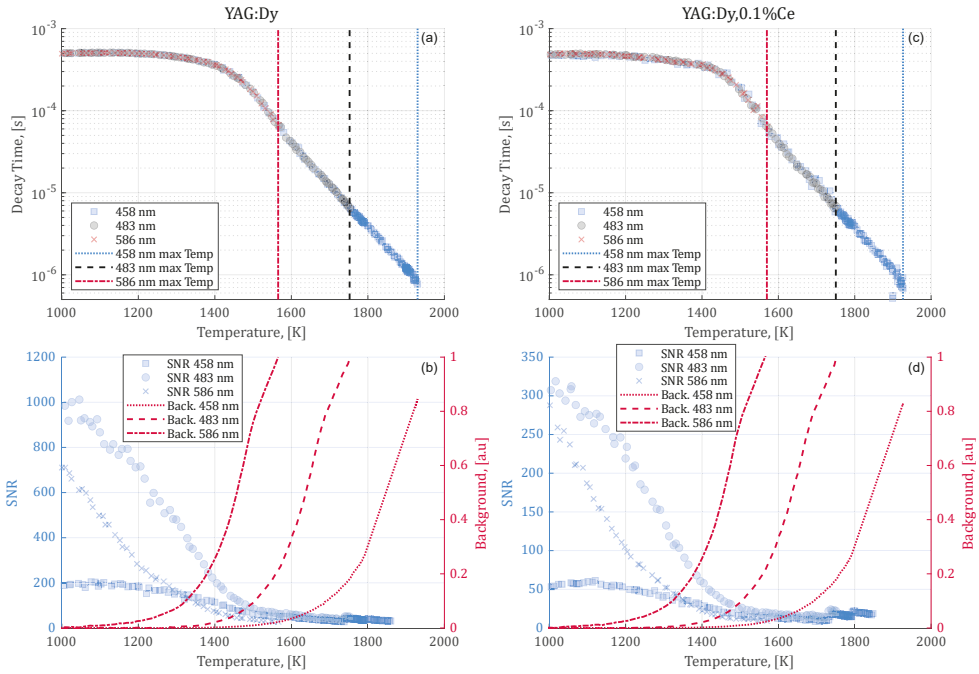

Figure 5.5: Calibration curves of YAG:Dy (a), (b) and YAG:Dy,0.1 % Ce (c), (d). The legend in (a), (c) refers to the bandpass filter used. The vertical lines in (a), (c) show the maximum calibration temperature for the bandpass filter with the same color. "Back." is the background signal measured by the PMT. Bandpass filters at shorter wavelengths extend to higher temperatures due to lower blackbody radiation intensity at those wavelengths, as seen in (b), and (d).

5.2 Maximum Entropy Method

The lifetime behavior of most thermographic phosphors is not mono-exponential; instead, they consist of several decay time components. For example, with YAG:Dy, a bi-exponential decay time fit is sometimes used for lifetime determination [49], [50]. This is because YAG:Dy's two longest lifetime components are quite closely located in the decay time distribution seen in Figure 5.6. Therefore, mono-exponential fitting on the long-lifetime components will be influenced by more than one decay time component. This can be seen by the vertical line in Figure 5.6, as the measured decay time is located between the two longest lifetime components.

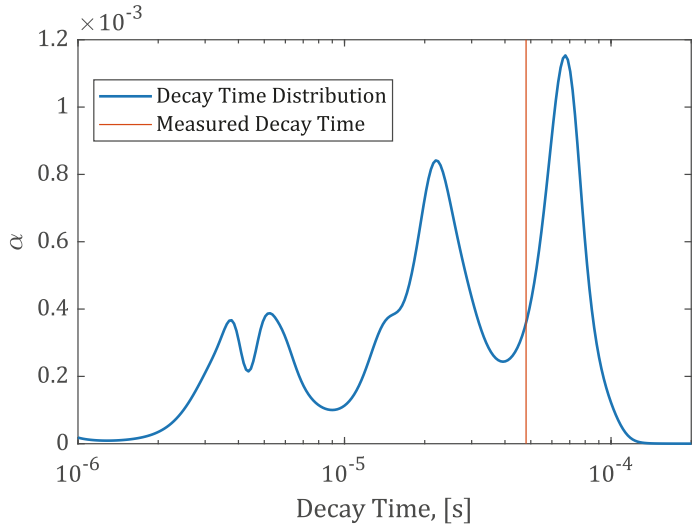

Figure 5.6: Decay time distribution of YAG:Dy at 1600 K showing only the longest lifetime components. The "Measured Decay Time" line shows the measured lifetime using mono-exponential lifetime fitting with $c_1 = 1$ and $c_2 = 4.5$. The measured decay time is influenced by the two longest decay time components.

The multi-exponential nature of phosphor decay and work published by Fuhrmann et al. [51] inspired a more in-depth investigation into the decay time distributions of phosphors. Of particular interest was how the decay time distribution varies with temperature.

The Maximum Entropy Method (MEM) was used to resolve the decay time distribution of MFG. Due to the long evaluation time, using large data sets with millions of data points in the MEM evaluation is impractical. As a result, dynamic down sampling was applied to the decay curve data, similar in concept to [63]. Figure 5.7 depicts the sampling of decay curves with various lifetimes at a sampling rate of 10 GS/s (the maximum sampling rate of the oscilloscope used in this thesis). The figure shows that for a lifetime of 5 ms, there are $1.5 \cdot 10^8$ data points during three lifetimes (15 ms) without down sampling. With dynamic down sampling, this number is reduced to $6 \cdot 10^4$ data points which is manageable for the MEM algorithm. In the dynamic down sampling algorithm, the maximum sampling rate of the oscilloscope is retained for the early parts of the decay curve. The sampling rate of the decay curve is then progressively reduced from the oscilloscope's sampling rate through down sampling to a minimum sampling rate of 4 MS/s. The MEM problem is formulated similarly to [51],[65] but with the computational approaches in [66], [67]. The MATLAB algorithm used for MEM analysis can be seen at https://doi.org/10.17605/OSF.IO/XTZN4 [64]. The same experimental setup was used as the high-temperature phosphor calibration shown previously.

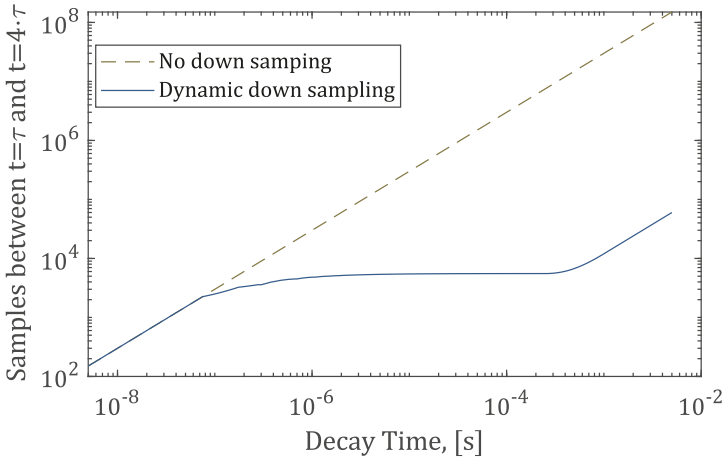

Figure 5.7: The number of sampling points between t=τ and t=4τ for decay times from 5 ns to 5 ms. The number of sampling points with and without dynamic down sampling are shown.

Figure 5.8 shows the result of using MEM to obtain the significant decay time components of MFG from 305 K to 1150 K. To better resolve the weighting, α, of the various lifetime components, the color bar is in log scale. A high α value indicates that the lifetime is significant in the luminescence decay. The sum of all α at a given temperature is always 1 ($\sum \alpha = 1$). The lower bound of the amplitude factor alpha was set as 10^{-5} for the plot and color bar to only to show relevant decay time components and to improve the color contrast for the alpha values shown. Figure 5.8 also shows the result of a mono-exponential decay curve fitting strategy using the widely recommended iterative decay time fitting scheme $c_1 = 1$ and $c_2 = 4$ [54] to resolve the long decay time component, here called θ. This mono-exponential fitting scheme has very little influence from decay components in MFG's decay other than the θ component.

The three longest decay time components at 305 K in Figure 5.8 are similar to those by Fuhrmann et al. [51]. The three decay components of MFG at room temperature were: 3.65/3.55, 1.28/1.03, and 0.318/0.265 ms in Fuhrmann et al.'s work depending on the laser fluence. The three longest decay time components at 305 K measured as part of this thesis were 3.42, 1.06, and 0.24 ms, which are very similar. Because calibration data was not collected below 305 K, a comparison at room temperature was not possible.

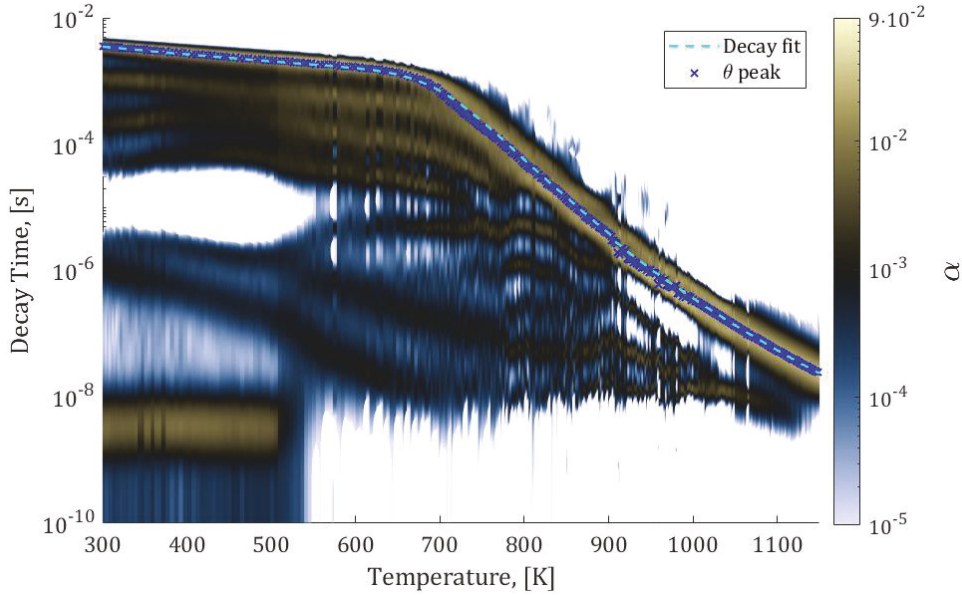

Figure 5.8: MFG's decay time distribution from 305 K to 1150 K. The lifetime weighting values, α, in the decay time distributions are represented by the color bar. Note that the color bar is in log scale. The dashed line depicts the outcome of mono-exponential fitting to the decay data, and the scattered plot shows the result of tracking the θ peak.

The decay time spectrum in Figure 5.8 shows the relative weighting of decay time components, but it does not show the strength of the integrated luminescence of each decay time component. This is shown in Figure 5.9, where the integrated luminosity is found by multiplying the weighting of each lifetime by its lifetime as the integrated luminosity (I_{lum}) of a decay curve with a decay time τ is:

$$I_{lum} = \int a \cdot e^{-\frac{t}{\tau}} = a \cdot \tau \tag{5.1}$$

In the integrated luminosity plot in Figure 5.9, longer decay times become, as expected, relatively stronger than shorter ones. The vertical lines at long lifetime components between 700 and 1050 K result from relatively shallow troughs in the decay time distribution being magnified due to the decay time multiplication.

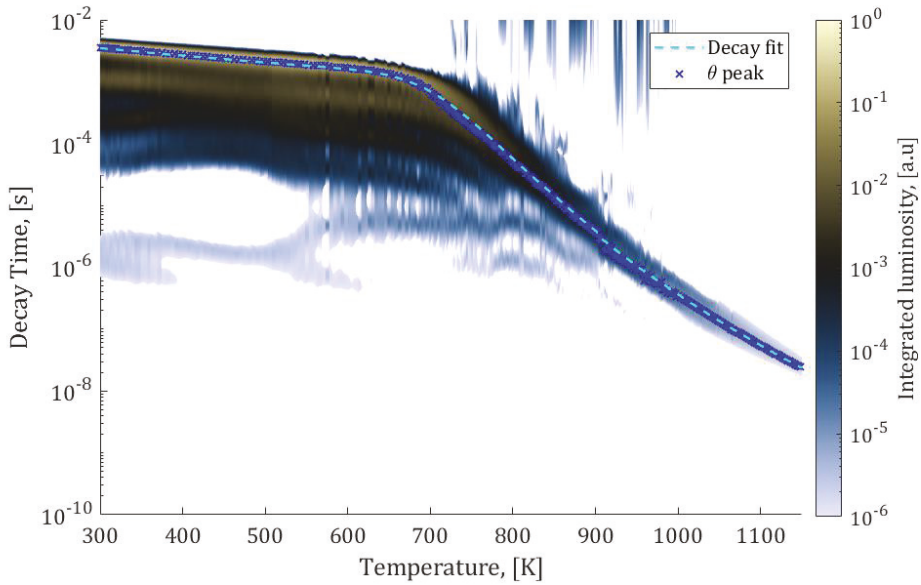

Figure 5.9: MFG's integrated luminosity of the decay time distribution from 305 K to 1150 K. The color bar shows the integrated luminosity in the decay time distributions. Note that the color bar is in log scale. The dashed line depicts the outcome of mono-exponential fitting to the decay data, and the scattered plot shows the result of tracking the θ peak. The lower bound of the integrated luminosity was set to 10^{-6} for the plot and color bar.

5.3 Upconversion Lifetime Phosphor Thermometry for use in TBCs

Thermal Barrier Coatings (TBCs) are typically composed of a Yttria Stabilized Zirconia (YSZ) topcoat attached to a metal substrate with a bond coat. TBCs are used to protect the metal substrate from high temperatures which allows for higher operating temperatures. Higher operating temperatures result in higher efficiency for gas turbines; however, if component temperatures become too high, TBC-coated components' lifetime can be significantly reduced [68]. Therefore, accurate temperature measurements in TBCs at the bond coat and the TBC surface can be used to balance system efficiency with component lifetime.

Because of the absorption and scattering of laser excitation light and phosphor luminescence as they propagate through the TBC, it is not easy to measure the temperature below the surface of the TBC with a thin phosphor layer. Upconversion, i.e., excitation wavelength longer than emission wavelength, phosphor thermometry, which was investigated as part of this thesis, could be one way to increase phosphor luminescence. It is appealing because using longer excitation

wavelengths reduces the absorption and scattering in TBCs as 8 % weight YSZ (8YSZ) generally has lower scattering and absorption coefficients for light around 1000 nm than at 532 and 355 nm. Therefore, the feasibility of upconversion phosphor thermometry was compared with downconversion phosphor thermometry in their ability to measure the temperature at the bottom of a TBC.

Downconversion measurements have been conducted on fully lanthanide-doped TBC layers [69], [70]. In addition, downconversion phosphor thermometry has also been used for phosphor layers embedded on top of the bond coat and on the surface of TBCs [71]–[74]. However, to the authors' knowledge, no prior studies had evaluated upconversion phosphor thermometry for temperature measurements in a TBC.

The study began with an experimental study of several phosphors, which were excited via downconversion by pulsed 355 nm, 532 nm laser light, and through upconversion with 965 nm laser light. Figure 5.10 (a) depicts the upconversion excitation spectra. The peak excitation wavelength was determined to be 965 nm, which is the expected excitation peak for YSZ doped with Yb^{3+} [75], [76]. Figure 5.10 (b) shows the emission spectra with an excitation wavelength of 965 nm.

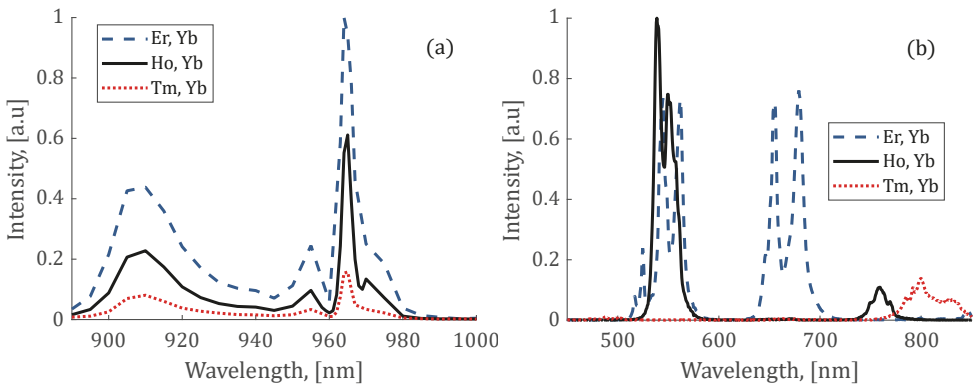

Figure 5.10: Upconversion excitation spectra of the 8YSZ phosphors in (a). The upconversion emission spectra of the phosphors with excitation at 965 nm are shown in (b).

The ground state absorption (GSA) of the Yb^{3+} ion from ground state $^2F_{7/2}$ to excited state $^2F_{5/2}$ with the 965 nm excitation laser light, shown in Figure 5.11, enables the upconversion process of YSZ:Ho,Yb. This energy is then transferred to the Ho^{3+} ion through energy transfer upconversion (ETU). The phosphor then decays with wavelengths shorter than the excitation wavelength. The same process occurs in Figure 5.11 for YSZ:Er,Yb, but direct excitation of the Er^{3+} ion with 965 nm excitation is also possible through GSA and excited state absorption (ESA) processes [77]–[80].

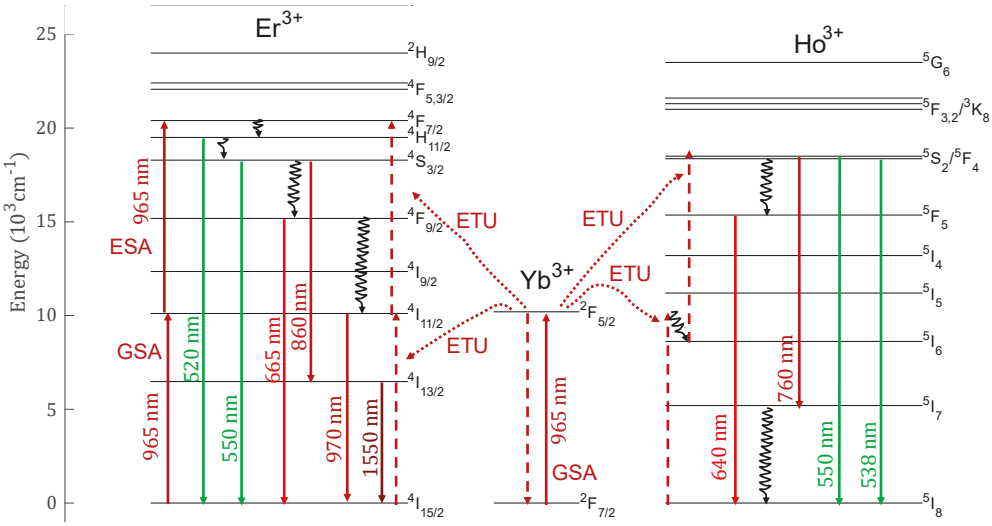

Figure 5.11: Energy level diagram of Er^{3+} and Ho^{3+} with simplified energy transfer dynamics for upconversion luminescence. The transitions are based on [78], [81]–[83].

When excited through upconversion, YSZ:Er,Yb and YSZ:Ho,Yb have long rise times in their lifetime behavior, as shown in Figure 5.12. This rise time component is resolvable for YSZ:Ho,Yb over the entire temperature range, but it could not be measured for YSZ:Er,Yb above 920 K. This is because YSZ:Er,Yb luminescence has a short lifetime component with a nanosecond rise time, which masks the relatively slow increase in luminescence intensity at higher temperatures. This short lifetime component of YSZ:Er,Yb is visible in the zoomed-in view in Figure 5.12 (a, c). In contrast, no short-lived luminescence is visible for YSZ:Ho,Yb in Figure 5.12 (b, d).

The rapid initial rise in luminescence for YSZ:Er,Yb followed by a short decay is caused by the direct population of Er^{3+}, as shown in Figure 5.11, via GSA from ground state $^4I_{15/2}$ to $^4I_{11/2}$ and then an ESA from $^4I_{11/2}$ to $^4F_{7/2}$ [77]–[80]. As a result, direct population of Er^{3+} without transitions from Yb^{3+} ions is possible. Populating higher energy levels through this method is much faster than the slow rise time due to energy transfer upconversion (ETU) from the $^2F_{5/2}$ to $^2F_{7/2}$ transition of the Yb^{3+} ion [84]. YSZ:Ho,Yb does not have this quick initial luminescence peak and subsequent decay. Because Ho^{3+} cannot be directly excited by the 965 nm laser light, it only has a relatively slow rise time component due to the ETU from the Yb^{3+} ion.

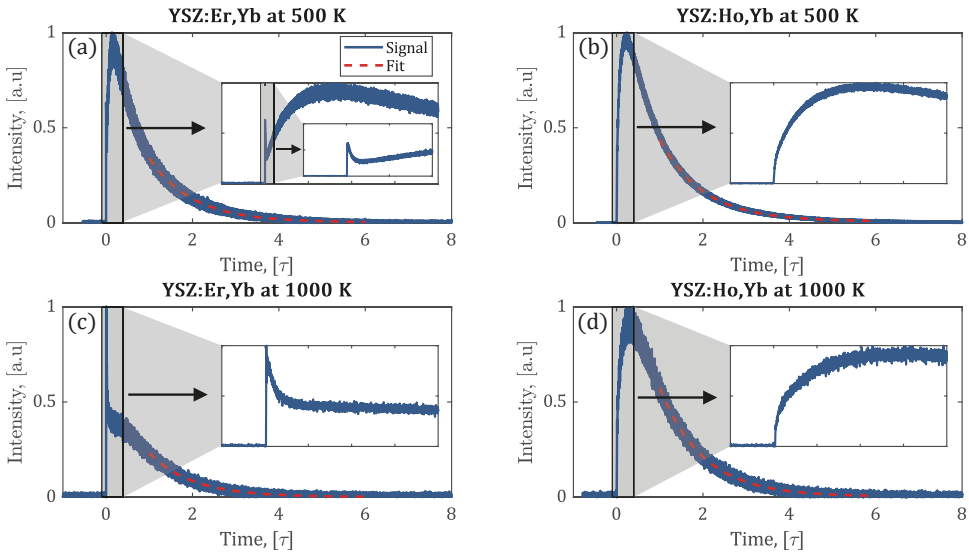

Figure 5.12: Shape of the upconversion decay curves. YSZ:Er,Yb at 500 K in (a) and at 1000 K in (c). YSZ:Ho,Yb at 500 K in (b) and at 1000 K in (d). The x-axis time scale was normalized based on the measured lifetime. To enhance the visibility of the phosphor luminescence, the short-lived signal around time 0 s was removed.

The experimentally obtained optical phosphor characteristics were then used with Kubelka-Munk theory to simulate laser light and phosphor luminescence propagation in TBCs. This was done to compare the signal strength with upconversion and downconversion excitation. Kubelka-Munk simulations have been used to describe the propagation of laser light and downconversion phosphor luminescence propagation in TBCs [72], [85]–[87]. These models have been used to predict the temperature sensing depth with fully lanthanide-doped TBC coatings and temperature gradients in the TBC [85]. The Kubelka-Munk equations were solved using an in-house developed MATLAB code based on work by Fouliard et al. [85]. The boundary conditions used in the simulation are described in [85], [86]. The algorithm is available at https://doi.org/10.17605/OSF.IO/XTZN4 [64].

Kubelka-Munk simulations were conducted with a 200 µm thick 8YSZ TBC with a phosphor-doped 8YSZ layer in the bottom 20 µm. The absorption and scattering coefficient values for the deposition techniques APS, EBPVD, and SPS, were taken from the literature [88]–[90]. Two excitation wavelengths were simulated for each TBC application process: 965 nm and 532 nm. From the Kubelka-Munk simulations, the fraction of the excitation light reaching the bottom of the TBC to excite the phosphor layer and the fraction of the stimulated phosphor luminescence reaching the TBC surface are estimated. However, to determine the optimal excitation wavelength for an embedded thin phosphor coating, whether 532 nm or 965 nm, the efficiency with which the phosphor is excited by the laser light also needs to be considered. Accounting for relative phosphor luminescence intensity

between YSZ:Er,Yb, YSZ:Ho,Yb, and YSZ:Er, and the fraction of phosphor luminescence reaching the TBC surface it was found that the 965 nm excitation of YSZ:Ho,Yb was consistently the most luminous configuration, as seen in Figure 5.13. The relative phosphor luminescence intensity was accounted for by experimentally gathered relative peak luminescence intensity values (covered in paper IX) for the three phosphors and two excitation wavelengths in the temperature range from 450 K to 1200 K.

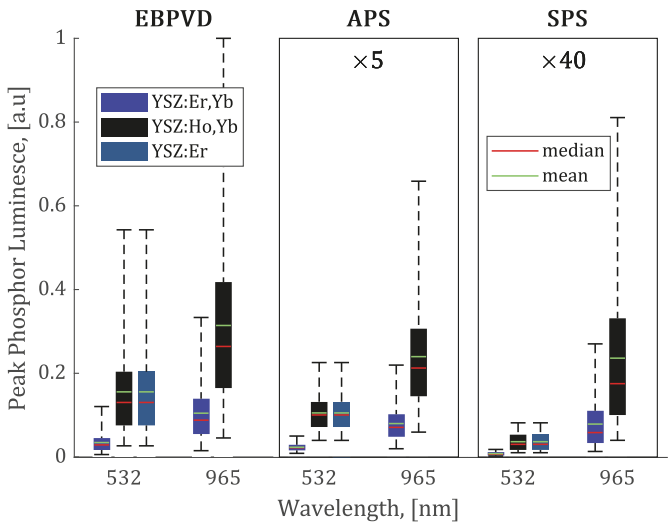

Figure 5.13: The peak phosphor luminescence intensity leaving the TBC. The plots show the minimum, maximum, lower and upper quartiles, mean, and median peak phosphor luminescence leaving the coating. The luminescence values are multiplied by 5 for the APS coating method and 40 times for the SPS method.

5.4 YAG:Tm,Li, and YAG:Dy at High Temperatures and Reduced Oxygen Environment

Yttrium aluminum garnet (YAG) is an attractive host lattice partly due to its high melting temperature of 2200 K and is therefore used for phosphors such as YAG:Dy, YAG:Tm, and YAG:Pr, all of which have emission lines in the blue region and have been used for thermometry [34], [35], [38], [91]–[97]. Co-doping has been studied to improve the luminosity of phosphors, which can increase luminescence and change the decay time [49], [93], [98]–[102]. Li^+ has previously been investigated as a sensitizer, and co-doping luminescence enhancement was attributed to increasing the crystallite size and breaking dopant-ion pairing [98], [103]–[106]. Up to a 100 % increase in emission intensity was found in these studies for phosphors co-doped with Li^+.

As shown in Figure 5.14, YAG:Tm, YAG:Tm,Li, and YAG:Dy were calibrated to high temperatures. Figure 5.14 (a) shows the peak phosphorescence signal of the lifetime component used for decay-time fitting (I_0 in Equation (3.2)). Adding Li^+ increased the peak signal of YAG:Tm,Li in the temperature range from 1100 K to 1800 K on average by 50 % compared with YAG:Tm, while having minimal impact on the decay time. The peak phosphorescence signal is approximately one order of magnitude greater for YAG:Tm,Li than YAG:Dy (see Figure 5.14 (a)). The higher peak signal consequently increases the SNR and the precision of temperature measurements.

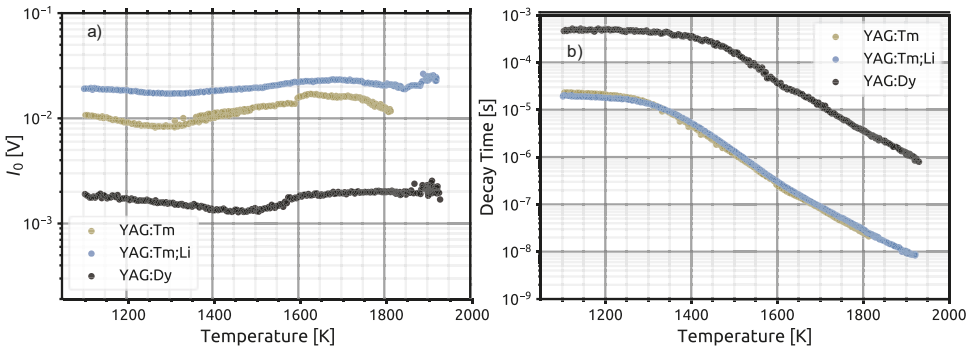

Figure 5.14: YAG:Dy and YAG:Tm,Li were calibrated in air to 1930 K using a 458 ± 10 nm bandpass filter. YAG:Tm was calibrated to 1810 K with the same bandpass filter. The parameter I_0 from Equation (3.2) is shown in a). The decay time vs temperature of the phosphors using $c_1 = 0.5$ and $c_2 = 4$ is shown in b).

The gas oxygen concentration sensitivity of thermographic phosphors has been investigated [50], [107]–[110]. However, no gas oxygen sensitivity study has been conducted over 1400 K, the temperature region of interest for thermometry purposes for YAG:Dy and YAG:Tm,Li. Therefore, the oxygen sensitivity of YAG:Tm,Li, and YAG:Dy was investigated at 1600 K in Figure 5.15 with the same fitting strategy ($c_1 = 0.5$ and $c_2 = 4$) as in Figure 5.14. The gas flow was initially set to normal air, and the oxygen content was gradually reduced to pure nitrogen in 5% increments every 20 minutes before returning to the initial conditions. Both phosphors were investigated concurrently in this study. Ideally, the determined lifetime should increase slightly when the gas flow is turned on due to the cooling effects of the gas flow, then remain constant for different oxygen concentrations, and then return to the initial condition when the gas is turned off. The reduced oxygen environment appears to have irreversible effects on the phosphors, as seen in Figure 5.15, but the impact on temperature measurements is less than approximately 0.5 % for YAG:Tm,Li, and 2 % for YAG:Dy. The error bars in Figure 5.15 (a) and Figure 5.15 (b) demonstrate the superior precision of YAG:Tm,Li over YAG:Dy. The analyzed decay curves were collected through averaging 100 single-shot decay curves.

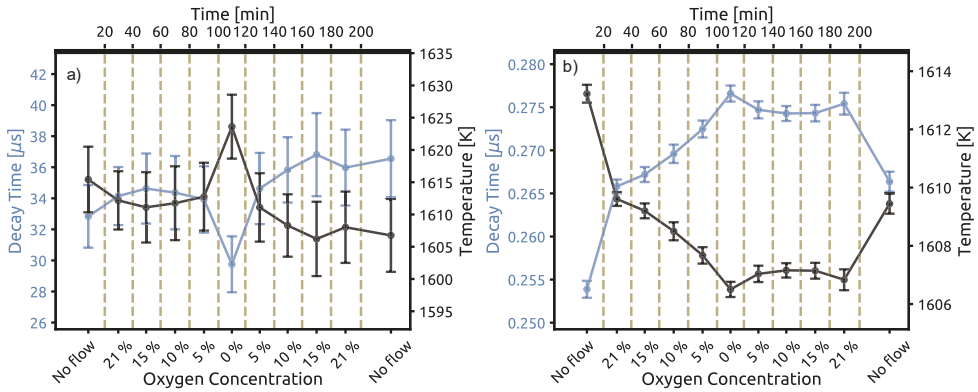

Figure 5.15: Measured phosphor lifetimes of the phosphors using a short fit with $c_1 = 0.5$ and $c_2 = 4$. (a) shows the measured decay time for YAG:Dy with error bars corresponding to the standard deviation. (b) shows the measured decay time for YAG:Tm,Li with error bars corresponding to the standard deviation. Note the difference between the temperature scales of the two phosphors on the right sides of the plots.

The effect of changes in oxygen concentration can be reduced by employing a customized decay-time fitting strategy; however, this comes at the expense of reduced measurement precision. Figure 5.16 shows the same data as in Figure 5.15 but performs the fit on a later part of the decay curve, with $c_1 = 1$ and $c_2 = 4.5$. The effect of reduced oxygen concentration is significantly reduced for YAG:Tm,Li, and the effect appears to be reversible, implying that the shorter decay components are mostly affected. Thermocouple data showed the same temperature trend as in Figure 5.16 (b) where the temperature was lower with gas flow, due to the cooling effect. The gas environment effect was also reduced for YAG:Dy, but changes in oxygen concentration still had a noticeable effect.

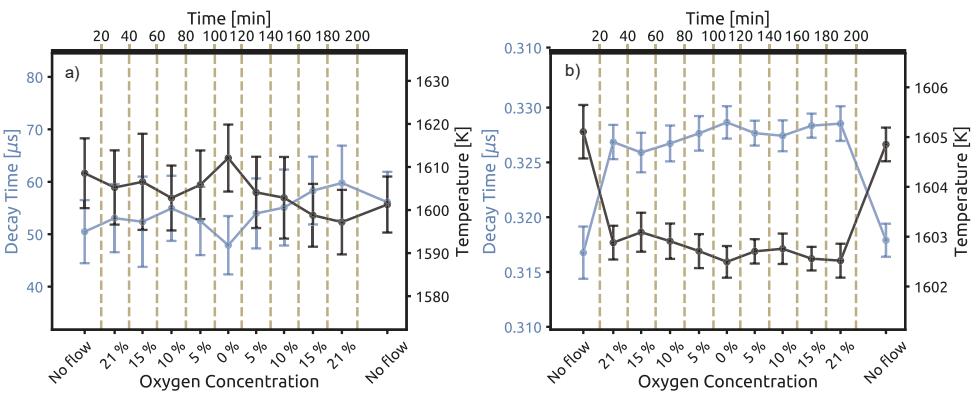

Figure 5.16: Measured phosphor lifetimes of the phosphors using a long fit with $c_1 = 1$ and $c_2 = 4.5$. (a) shows the measured decay time for YAG:Dy with error bars corresponding to the standard deviation. (b) shows the measured decay time for YAG:Tm,Li with error bars corresponding to the standard deviation. Note the difference between the temperature scales of the two phosphors on the right sides of the plots.

The decay curves were analyzed using MEM to determine the significant decay time components shown in Figure 5.17. The figure shows the average decay time distribution for the intervals of 21 %, 5 %, and 0 % oxygen concentration. The dashed vertical lines in Figure 5.17 (a) and (b) for the long and short fits are the mean measured lifetimes at 0 % oxygen for each respective fitting strategy and phosphor. A zoomed view in Figure 5.17 (a) shows two decay time components on either side of the two lifetime fits, indicating that both components were used for fitting. When the oxygen concentration is reduced from 21 % to 0 %, the lifetime component on the right side of the measured lifetime decreases by 18 % compared to 21 % oxygen, resulting in a shorter determined lifetime for both fitting windows for 0 % oxygen compared to 21%. Similarly, the two rightmost components in the zoomed view in Figure 5.17 (b) are those used for lifetime determination when using a mono-exponential fitting. However, at 5 % and 0 % oxygen concentrations, the two leftmost components in the zoomed view in Figure 5.17 (b) decrease in relative weighting and shift to longer decay times, while the rightmost component does not shift with oxygen concentration. With the long fit, YAG:Tm,Li's decay time is almost entirely dependent on one lifetime component, and the peak of that lifetime component does not change with oxygen concentration. The singular lifetime dependence is evident as the long fit coincides quite well with the decay time peak corresponding to the longest lifetime component in the zoomed view in Figure 5.17 (b). This shows that the lifetime oxygen sensitivity is highly dependent on the decay time analysis methodology.

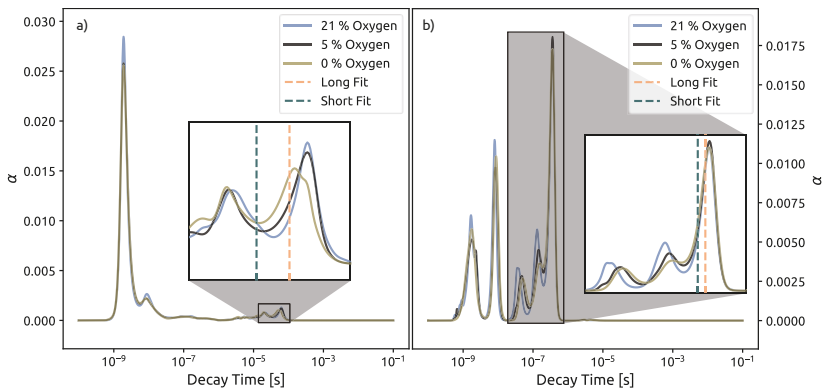

Figure 5.17: Decay time distribution of YAG:Dy in (a) and YAG:Tm,Li in (b). The decay time distributions were averaged for each interval when going from 21 %, 5 %, and 0 % gas oxygen concentration.

6 Sources of Error

It is crucial to consider sources of error with measurements to make accurate and reliable temperature measurements. One crucial factor to consider is detector effects which could create systematic temperature measurement errors. One such factor is the linearity of the intensity response of PMTs to variations in the phosphor luminescence intensity. Ultimately one wants to avoid this dependence to ensure that signal fluctuations due to excitation pulse and phosphor luminesce extinction do not alter the measured decay time. Optical extinction can be due to the scattering and absorption of photons in regions with, for example, high levels of soot. Differences in signal intensity could also occur due to calibrating with signal levels different from the measurement environment. Two papers, II and III, were dedicated to quantifying the possible impact detector linearities have on PMT-based lifetime phosphor thermometry measurements.

Another source of error studied as part of this thesis was laser excitation effects when exciting phosphors at 10 Hz and in the kHz range. This work, published in paper V, was performed to evaluate the impact of phosphor sensitivity to laser fluence and laser repetition rate on practical phosphor thermometry measurements.

6.1 Impact of PMT Nonlinearities on Phosphor Luminescence Decay Curves

Previous research has shown that nonlinear PMT effects can cause significant errors in measured decay time when the phosphorescence intensity changes. This is especially an issue for single-shot measurements where high SNR values necessitates strong phosphor luminescence signals which have the potential for PMT nonlinearity effects impacting the shape of the decay curve.

Previous detector studies have only looked at detection system effects at fixed or slightly varying decay times. Furthermore, the effects of changing phosphorescence intensity, PMT gain, and laser fluence were not always sufficiently decoupled in these studies [111]–[113]. When studying the relationship between laser fluence and measured decay time [61], [114], the importance of decoupling these factors becomes clear. The effects of changing phosphorescence intensity on detector nonlinearity are best studied by attenuating the phosphorescence signal in a

controlled manner. For example, if one changes the phosphorescence intensity by changing the excitation pulse's fluence, it is unclear if detector effects or changes in the phosphorescence cause changes in measured decay time. Therefore, neutral density filters were used to change the phosphor luminescence intensity.

The phosphors YVO_4:Tm and MFG were used to provide luminescence decay curves for the PMT nonlinearity investigation. MFG was chosen because of its widespread use in the phosphor thermometry field and its long decay time at room temperature. YVO_4:Tm was selected for its stronger phosphorescence than MFG at decay times below 10^{-5} s. Their combined decay times span multiple orders of magnitude while maintaining sufficient phosphorescence signal intensities for this study.

The impact of two different peak signal levels is analyzed in Figure 6.1 for YVO_4:Tm decay curves with decay times around 7 µs, where the collected phosphor luminescence was varied with an ND filter. In the 470 mV case, the higher signal level causes more significant space charge accumulation at the anode and the last few dynodes. Space charge accumulation disrupts electron propagation, reducing anode current and lengthening the signal, resulting in a longer perceived decay time [115]. Due to the reduced accumulation of space charges, the lower 100 mV signal has a shorter decay time.

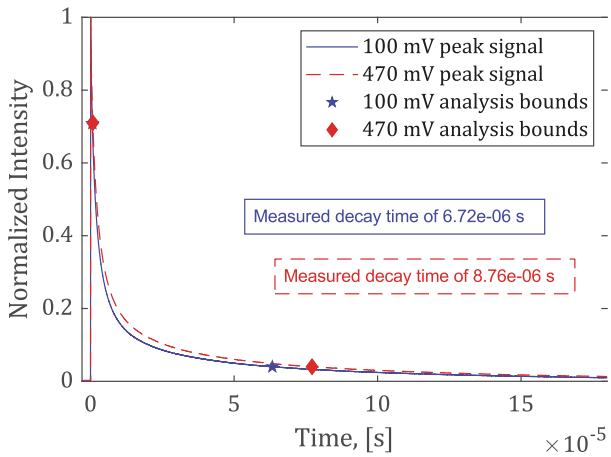

Figure 6.1: PMT nonlinearity impact on the shape of YVO_4:Tm's decay curve with a decay time around 7 µs. The decay curve was collected with a PMT control voltage of 0.3 V for the H11526-20-NF PMT.

In particular, for long decay times, high average phosphor luminosity intensity can lead to photocathode bleaching or dynode chain depletion in PMTs. The rapid decrease in signal intensity for the 300 mV signal after about 2 ms in Figure 6.2 can be attributed to photocathode bleaching. After bleaching, it takes some time for the photocathode to recover and return to a linear response [115]. However, the effect

may also be due to charge depletion in the PMT's dynode chain [116]. Due to space charge effects, the 300 mV decay curve is higher than the 100 mV signal until 2 ms, as shown in Figure 6.2. After 2 ms, the photocathode bleaching, or dynode chain depletion, takes over as the dominant source of nonlinearity, and the signal intensity rapidly decreases. It appears that the photocathode or dynode chain recovers towards the end of the decay curve as the 300 mV signal moves closer to the 100 mV signal over time.

The mean PMT anode current is a function of the oscilloscope input resistance ($\Omega_{oscilloscope} = 50\Omega$), peak signal level (voltage, I_0), decay time (τ) and repetition rate ($f = 10Hz$), and background luminosity intensity (voltage, $I_{background}$):

$$I_{anode} = \frac{\tau \cdot I_0 \cdot f + I_{background}}{\Omega_{oscilloscope}} \tag{6.1}$$

The maximum recommended average output anode current specified for the PMT used in this investigation is 100 µA. With the decay times in Figure 6.2, the average anode current was approximately 70 µA for the 100 mV peak signal decay curve and 140 µA for the 300 mV peak signal decay curve.

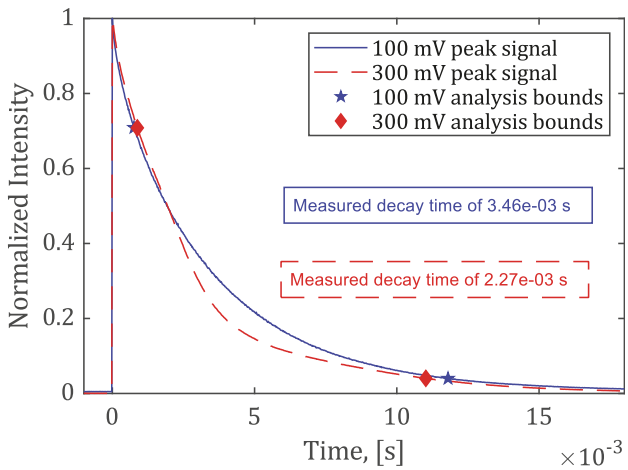

Figure 6.2: PMT nonlinearity impact on the shape of MFG's decay curve for decay times around 3 ms. The decay curve was collected with a PMT control voltage of 0.4 V resulting in a gain of $4 \cdot 10^3$ for the H11526-20-NF PMT.

In general, the PMT showed improved linearity with an increase in gain for a given peak signal level and decay time. In particular gains below the recommended gain of the PMTs resulted in worse linearity. However, higher gains resulted in worse decay time precision due to needing lower luminescence signal intensity (lower signal) at the photocathode to result in the same peak signal level as a lower gain setting. Thus, the choice of gain should be made based on a balance between precision and accuracy for a given application. Another way to combat temperature

errors caused by detector nonlinearities is to use higher sensitivity phosphors as a percentage change in measured decay time results in a smaller percentage temperature error with a more temperature sensitive phosphor.

6.2 Simulated High-Speed Phosphor Luminescence Decay Curves to Investigate PMT Nonlinearities

High-speed phosphor thermometry measurements have been conducted [114], [117], [118], and they are attractive because they can resolve transient events with fast-changing temperatures. Prior to this work, there had been no research on PMT nonlinearity effects relevant to phosphor thermometry with repetition rates in the kHz range. PMT nonlinearity effects relevant for single-shot high-speed lifetime phosphor thermometry were studied by light emitting diode (LED) simulated decay curves at repetition rates from 1 Hz to 10 kHz. Two decay times were simulated with the LED: one at ~11.5 μs and one at ~100 μs.

For the 11.5 μs decay time decay curves, the repetition frequency ranged between 1 Hz and 10 kHz, and for the 100 μs decay time decay curves, it ranged between 1 Hz and 1 kHz. The maximum repetition rate for the 100 μs decay time was limited to 1 kHz to ensure that one decay curve had ended before emitting the next, avoiding issues with incomplete decay curves [119]. Because of the LED and LED driver's limited time response, decay curves less than 11.5 μs could not adequately be reproduced.

LEDs are appealing because of how easily the repetition rate and decay time can be changed. In comparison, changing a laser system's repetition rate from 1 Hz to 1 kHz is difficult to do quickly without affecting the laser pulses' output characteristics. However, the main motivator to use an LED instead of phosphor luminescence is to avoid the effects caused by laser heating and phosphor excitation flux dependencies. As a result, detector effects are isolated by simulating decay curves with an LED. The decay curve radiant flux reaching the PMT was altered in the study using neutral density filters and never by changing the LED driving current. This was done to investigate detector sensitivity to radiant flux fluctuations at various LED repetition rates.

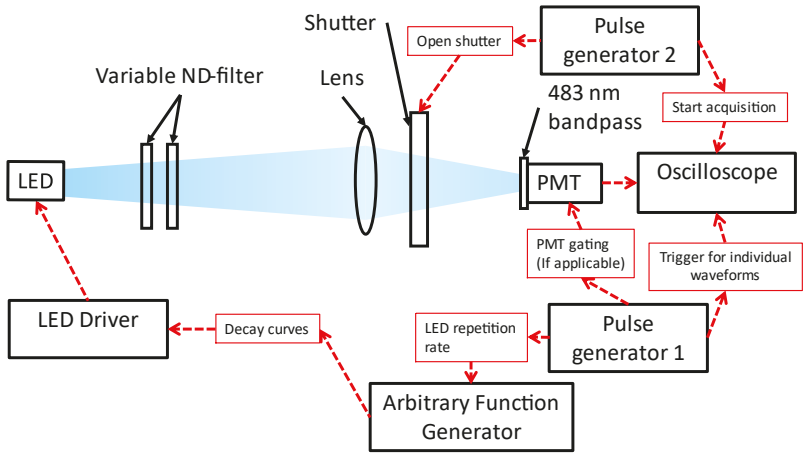

Figure 6.3: Experimental setup using an LED to simulate phosphor luminescence. For this purpose, a Thorlabs M490L4 LED with a 490 nm center wavelength was used.

All data collections began with the LED operating at a fixed repetition rate before data acquisition to guarantee steady operation. An activation pulse from pulse generator 2 in Figure 6.3 was then used to activate the oscilloscope, which was followed by a pulse to the shutter, which opened 8 ms after the oscilloscope was activated. The shutter opened after the oscilloscope began collecting data to record the transient behavior of the PMT as it became exposed to the radiant flux sources. During data collection, the shutter remained open, and no LED or background light was detected after it was closed. 500 decay curves were recorded for each data acquisition to assess how the PMTs' reactions varied over time.

The effect on the peak signal level of the decay curves with different LED repetition rates for the 500 consecutive decay curves can be seen in Figure 6.4. In the less intense decay curves in Figure 6.4 (a), there is no reduction in peak signal level; instead, the peak signal level increases marginally with the repetition rate. This is most likely due to the light flux altering the interstage voltage and increasing the detector's gain [120]. The more significant reduction in peak signal level with increasing LED repetition rate in Figure 6.4 (b) is primarily attributed to photocathode bleaching. Note that the peak signal levels appear to tend towards the voltage measured at 1 Hz, but 500 consecutive waveforms are not sufficient to allow the PMT to reach a steady state condition in its peak signal level.

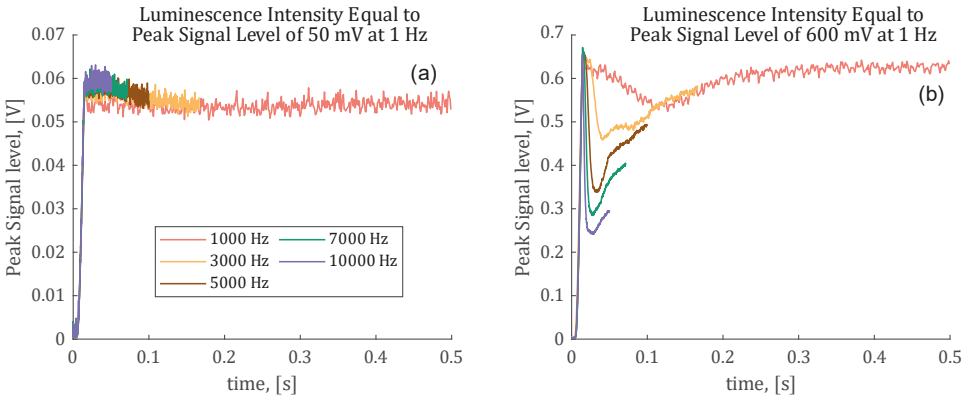

Figure 6.4: The peak signal saturation for 11.5 µs decay time decay curves and $4 \cdot 10^3$ gain. 50 mV 1 Hz peak signal in (a) and 600 mV in (b).

For the peak signal level in Figure 6.5 and decay time in Figure 6.6, the average of the last 200 recorded waveforms was utilized. The error bars in Figure 6.5 and Figure 6.6 represent the standard deviation in the single-shot peak signal levels and decay times, respectively. The peak signal level shown in Figure 6.5 (a) and (b) is the normalized average of the peak signal level for LED simulated decay curves with 11.5 µs decay time. The 100 µs decay time data is shown in Figure 6.5 (c) and (d). Radiant flux levels were normalized by dividing peak signal levels at a 1 Hz LED repetition rate since this reflects the circumstance with the lowest photon flux to the detector for a particular decay curve radiant flux level and, as a result, should minimize detector nonlinearity. Comparing the relative saturation in the peak signal level by different LED decay curve intensities becomes easier through peak signal normalization.

In Figure 6.5, a completely horizontal line linking the data indicates perfect intensity linearity of the detector. Increased LED repetition rates lowered the recorded peak signal level with low detector gain (Figure 6.5 (a) and (c)) and high radiant flux levels. Higher gain settings exhibited reduced intensity nonlinearity (Figure 6.5 (b) and (d)). With a lower detector gain, higher radiant flux is needed on the photocathode to result in a given peak signal level than with higher detector gain. The higher photon flux at lower gains makes photocathode bleaching more likely, leading to more significant nonlinearity for the lower gain in Figure 6.5.

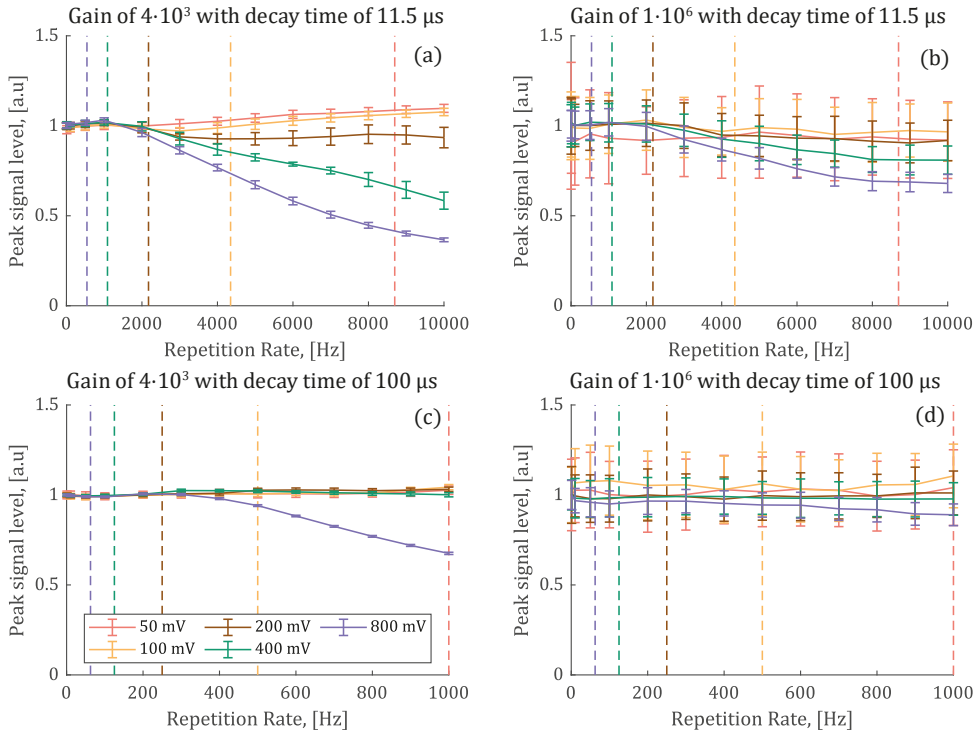

Figure 6.5: Peak signal level of decay curves vs LED repetition rate with 11.5 µs decay time for (a) and (b) and 100 µs decay time for (c) and (d). Each data point is the mean of 200 single-shot measurements. The error bars show the standard deviation in the single-shot measurements' peak signal level. The voltages in the legend show the measured peak signal level at a 1 Hz LED repetition rate. The dashed vertical lines depict the repetition rate when the mean anode current is 100 µA for the data with the same color.

Figure 6.6 (a) and (b) depict the decay time sensitivity to changes in peak signal levels at different repetition rates for an 11.5 µs decay time and for 100 µs decay time in (c) and (d). The peak radiant flux corresponding to a peak signal level for a given gain can change for a given measurement situation due to, for example, absorption and scattering. Therefore, it is of interest to see how changes in peak signal level result in detector nonlinearity. In Figure 6.6, an ideal detector would have a horizontal line linking the decay times, indicating that the detector is insensitive to variations in radiant flux. Additionally, the repetition rate should not affect the performance of an ideal detector.

At high radiant flux levels and high repetition rates, the PMT's low gain setting performance (Figure 6.6 (a) and (c)) is poor. At first glance, the PMT's high gain behavior appears to also exhibit severe nonlinearities (Figure 6.6 (b) and (d)); however, the short decay time at low peak signal levels is due to the signal being too noisy for accurate decay time fitting. Additionally, both detectors perform well with high gains at higher peak signal levels. The fact that the decay time and peak

signal level remain very stable when the repetition rate is changed for low LED radiant flux levels reaching the PMT, and good signal-to-noise ratios confirms that the decay curves generated by the LED do not change based on the repetition rate.

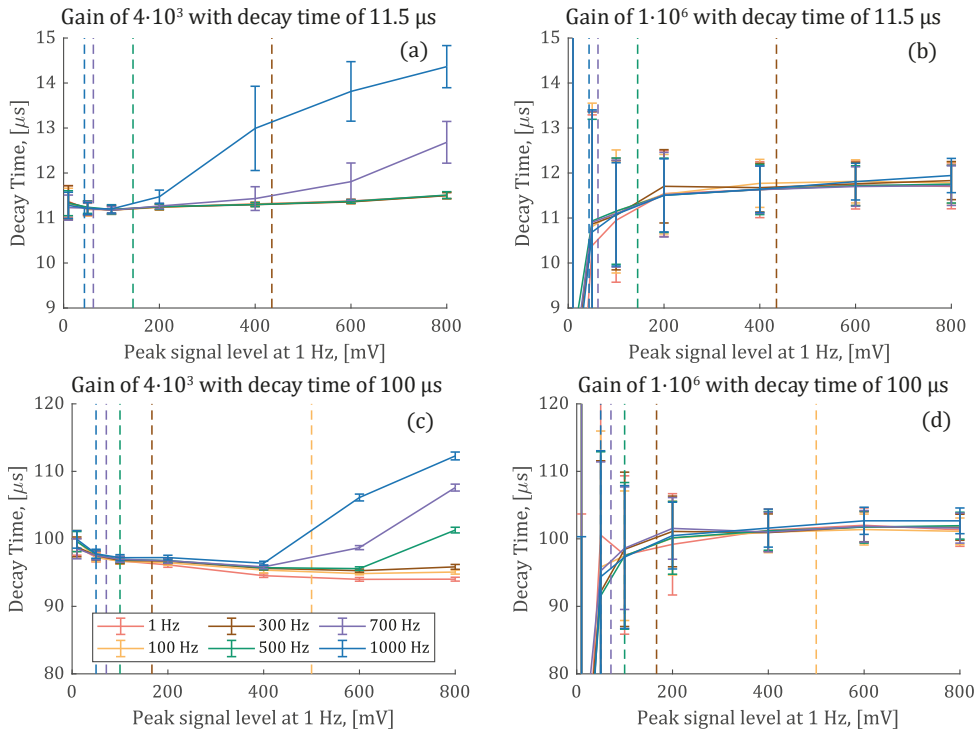

Figure 6.6: Decay time of decay curves vs LED repetition rate with 11.5 µs decay time for (a) and (b) and 100 µs decay time for (c) and (d). Each data point is the mean of 200 single-shot measurements. The error bars show the standard deviation in the single-shot measurements' decay time. The repetition rates in the legend show the LED repetition rate used. The dashed vertical lines depict the repetition rate when the mean anode current is 100 µA for the excitation frequency with the same color.

The potential for decay time measurement error increases when going from 10 Hz lifetime phosphor thermometry using PMTs to kHz measurements. The results show that to minimize detector nonlinearity effects one should have relatively high gain and low photon flux. However, to maximize measurement precision one wants high photon flux which necessitates lower gain. Therefore, to achieve a balance between measurement precision and detector nonlinear effects, one should use the lowest gain possible (above the recommended gain of the detector to avoid the wide range of issues that may occur at these gains [121]), where the detector is linear, and the oscilloscope can use its full vertical resolution. The effect of varying the radiant flux intensity on any given PMT will vary. However, the methods presented here may be utilized by phosphor thermometry practitioners to assess and enhance the temperature measurement accuracy of high-speed lifetime measurements.

6.3 High-Speed Phosphor Laser Excitation Effects

As high-speed phosphor thermometry becomes more widely used [114], [122], [123], a better understanding of laser-induced measurement errors is required. Reduction in decay time in phosphor thermometry measurements due to increases in laser fluence has, in some studies, been attributed to laser heating [114], [124]. However, some studies have attributed it to decay time cross sensitivities in phosphors to the excitation laser energy [51], [125]. The MFG and YVO_4:Tm phosphors were used in this study to investigate the impact of high-speed laser excitation effects on temperature measurement errors with the lifetime method.

Most laser excitation sensitivity studies have been restricted to repetition rates around 10 Hz. This includes laser excitation sensitivity investigations with both the lifetime [61] and intensity ratio [30], [124], [126] methods. Laser excitation sensitivities for high-speed phosphor thermometry have been studied, but only at a single laser repetition rate [114].

The third harmonic from an Edgewave HD40I-OE Nd:YAG laser (355 nm) with repetition rates of 1, 5, and 10 kHz was used to excite the phosphors. The laser's pulse duration was approximately 5 ns. All three high-speed laser repetition rates were used at the two temperatures studied per phosphor. For both phosphors, both temperatures, and the three laser repetition rates, the laser pulse fluence was scanned from 0.01 mJ/cm^2 progressively up to 0.91 mJ/cm^2 resulting in a mean irradiance of 0.1 W/cm^2 and 9.1 W/cm^2 at 10 kHz, respectively.

The laser fluence was scanned using two polarizers with a rotatable half-wave plate between them and never by changing the pumping or Q-switch parameters of the laser. This was to ensure the same laser pulse characteristics for all measurements. Before all measurements, the temperature of the furnace and the phosphor-coated disc were ensured to be at steady state conditions. In addition, the peak signal level of the phosphorescence measured by the PMT was ensured to be constant as the laser fluence was scanned using neutral density filters in front of the PMT. This was done to guarantee that the variations in the decay curve were produced by phosphor effects rather than detector nonlinearities, which might obscure laser excitation effects [121].

MEM was utilized to investigate the phosphorescence decay curves' underlying decay time components and better understand the decay changes. This is because it will shed light on the origins of variations in decay time, which is difficult using mono-exponential fitting methods since the measured decay time is inherently biased depending on the parameters utilized.

For MFG excited at 10 kHz, the decay curve has two distinct decay time distribution peaks at low laser fluence, which transitions to three peaks at high laser fluence, as seen in Figure 6.7 (a) and (b). An increase in laser fluence strengthens the shortest

visible decay component relative to the longest decay time, which is consistent with Fuhrmann's work [51].

At the lowest laser fluence of 0.09 mJ/cm^2, the longest decay component is stronger than the shortest decay component for MFG at both ambient temperatures and all repetition rates in Figure 6.7. However, for the highest laser fluence of 0.91 mJ/cm^2 and repetition rate of 10 kHz, seen in Figure 6.7 (a) and (b), the shortest decay component becomes stronger than the longest component. Similarly, an investigation into the effect of the duration of pulse excitation on the decay of phosphors revealed that it could impact the relative strength of shorter and longer decay time components of some phosphors [127].

The decay time distribution of the 1 kHz excited data in Figure 6.7 (e) and (f) showed relatively minor changes in the distribution of decay time components with laser fluence. The trends for increases in laser fluence for MFG with 5 kHz excitation in Figure 6.7 (c) and (d) show a weaker fluence sensitivity than at 10 kHz but more substantial than at 1 kHz. This demonstrates that the change in the decay time distribution for MFG is strongly correlated with the mean irradiance of the laser excitation.

If the laser heating caused the decay time distribution changes, the relative weighting of the lifetime components in the distribution should not change as they are relatively constant between 850 and 950 K, other than the shift to shorter decay times with higher temperatures. As a result, the difference in observed decay time cannot be attributable to laser heating. This study shows the MEM's capability by demonstrating that the primary source of the observed decay time variation is changes in the decay's multi-exponential behavior rather than laser heating.

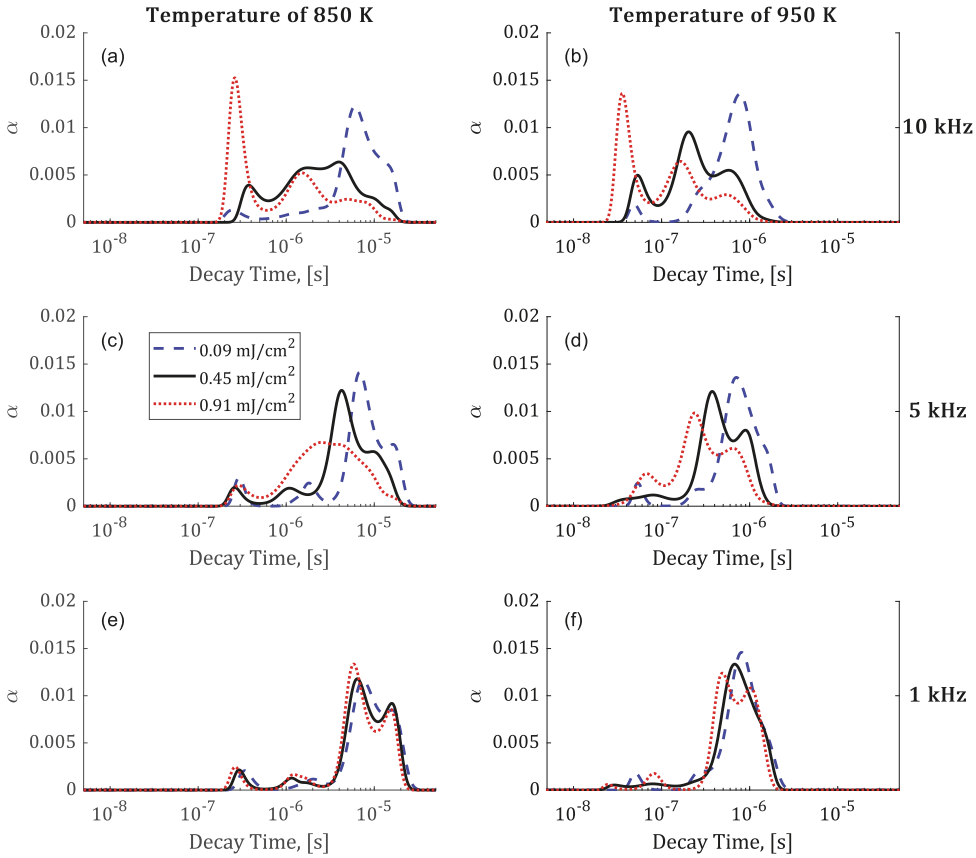

Figure 6.7: Decay time distributions of MFG. At 850 K, decay time distributions are shown for 10 kHz (a), 5 kHz (c), and 1 kHz (e). At 950 K, decay time distributions are shown for 10 kHz (b), 5 kHz (d), and 1 kHz (f). Each decay time distribution is performed on the average of 400 single-shot decay curves for each laser fluence. The sum of the weighting factor α in each decay time distribution is one.

For YVO_4:Tm at the ambient temperature of 400 K and excitation rate of 10 kHz (Figure 6.8 (a)), three distinct and similarly strong decay time components are evident for the lowest laser fluence, which reduces to a single very strong decay time peak with a few minor decay time peak contributions at higher laser fluences. This change in decay time multi-exponentiality has a similar trend at 5 kHz (see Figure 6.8 (c)) and 1 kHz (see Figure 6.8 (e)), meaning that the change in decay time multi-exponentiality is primarily a function of the laser pulse fluence.

The lowest fluence of 0.02 mJ/cm^2 for an ambient temperature of 510 K, shown in Figure 6.8 (b), (d), and (f), is dominated by a single decay time peak, with minor contributions from a longer decay time component. As the fluence increases, the peak values shift to shorter decay times, and the trend is the same for all laser repetition rates.

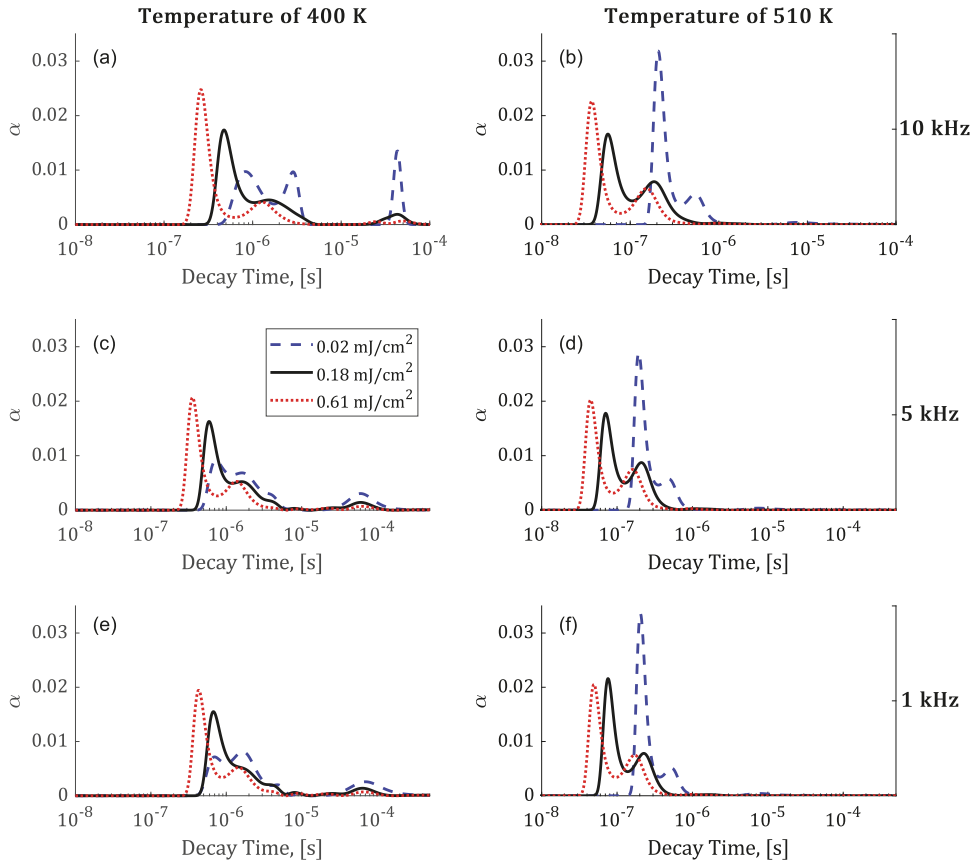

Figure 6.8: Decay time distributions of YVO_4:Tm. At 400 K, decay time distributions are shown for 10 kHz (a), 5 kHz (c), and 1 kHz (e). At 510 K, decay time distributions are shown for 10 kHz (b), 5 kHz (d), and 1 kHz (f). Each decay time distribution is performed on the average of 400 single-shot decay curves for each laser fluence. The sum of the weighting factor α in each decay time distribution is one.

MFG and YVO_4:Tm have vastly differing laser fluence sensitivities, raising questions about their origin. MFG decay time variation was directly related to laser irradiance but only indirectly to laser fluence. YVO_4:Tm, on the other hand, demonstrated high sensitivity to laser fluence and low sensitivity to laser irradiance. The opposite response of the two phosphors demonstrates that sensitivity to excitation conditions may work by different mechanisms in the two phosphors. This shows that even at the high-speed repetition rates and mean irradiances examined, the data do not indicate laser heating as a significant contribution to decay time changes. Additionally, the sensitivity to excitation conditions is an important quality in deciding how suitable a phosphor is for use in lifetime thermometry.

7 Applications

As a part of this thesis work, surface phosphor thermometry was used in two applications. In one work, the surface temperature of burning biomass pellets was measured, and in another, the surface temperature of a combustion nozzle was measured. The data collection method is based on the calibration algorithm described in section 5.1 and the general format of the data collection program allows for point-wise scanning for temperature measurements across a surface. This chapter covers the material published in papers I and VI.

7.1 Surface Temperature Measurement on Burning Biomass Pellets

Individually burning biomass pellets were studied [128]–[130] with the aim of better understanding the combustion process [131], [132]. Thermocouples have been used for surface temperature measurements surface of biomass samples [132]–[134]. However, heat transfers and catalytic reactions from the thermocouple wires cause perturbations. Pyrometry has also been used for surface temperature measurements of biomass pellets[130], [132], but the technique is sensitive to interfering background signals and low signals at lower temperatures. As a result, phosphor thermometry was used, for the first time, to provide an accurate surface measurement of biomass pellets across the whole burning history. In this study, two phosphors, MFG and YAG:Tb (Phosphor Technology Ltd.), were utilized using the lifetime method to measure the surface temperatures of burning pellets from 300 K to 950 K and 850 K to 1300 K, respectively. The experimental setup for phosphor thermometry is shown in Figure 7.1 (b). The surface measurement position was at the side of the pellet, as seen in Figure 7.1 (b).

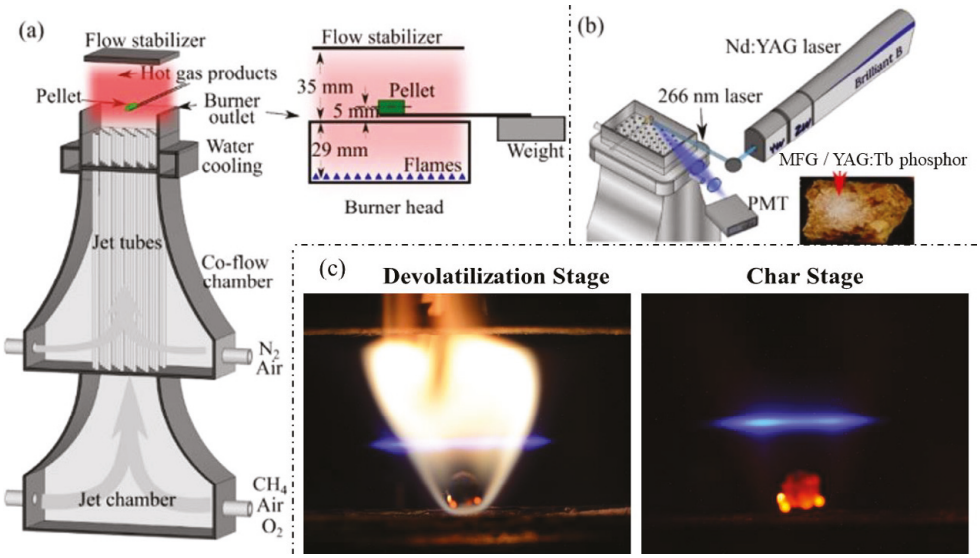

Figure 7.1: Schematics of the multi-jet burner (a), phosphor thermometry experimental setup (b), and images of the burning wood pellet at the devolatilization and char stage (c).

A laminar flame burner, shown in Figure 7.1 (a), was used to provide hot gas environments [135]. Figure 7.2 depicts the surface temperature of individually burned biomass pellets in various hot gas conditions. The burning process was divided into two phases, devolatilization and char stages, as shown in Figure 7.2 by the vertical dashed lines. The visual appearance of the two stages is shown in Figure 7.1 (c). The gas temperature in the legends in Figure 7.2 was determined using two-line atomic fluorescence thermometry with indium atoms [136].

The pellets were heated by placing them in the hot gas flow, and the surface temperature climbed from ambient temperature to 600 K in the first 10 seconds (Figure 7.2). Decomposition occurred in the wood pellet when the temperature exceeded 600 K, releasing volatile gases [137]. Because this is an endothermic process, only a minor surface temperature increase was observed until the devolatilization stage concluded at approximately 60-70 s.

Higher surface temperatures were measured for the conditions with 4.5% oxygen compared to the conditions with 0.5% oxygen (Figure 7.2) because volatile gases burning above the pellets under the former conditions (Figure 7.1 (c)) supplying extra heat to the pellets. The surface temperatures for wood and straw pellets were comparable (Figure 7.2 (a) and (d)).

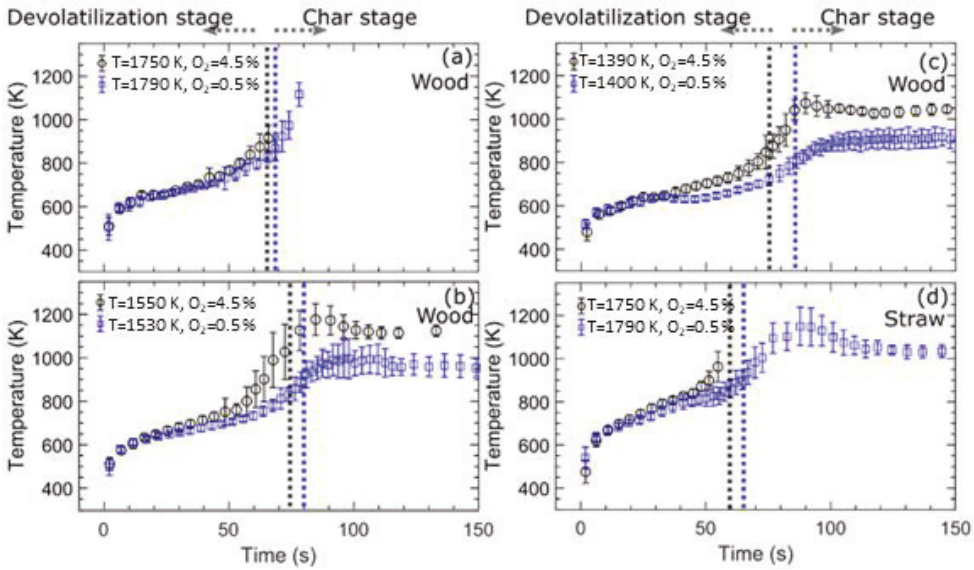

Figure 7.2: Surface temperature of individually burning biomass pellets in different hot gas environments over the burning time. Vertical dash lines separate the devolatilization stage and the char stage. The temperatures and oxygen concentration in the legend indicate the gas temperature and oxygen concentration 5 mm above the burner outlet.

Following the devolatilization phase, the surface temperature quickly increased, and char burning began. The surface temperature stayed approximately constant during the char-burning stage and was approximately 500 K lower than the hot surrounding gas. The lower surface temperature implies that the burning char lost substantial heat due to thermal radiation and heat conduction through the holders. It should be highlighted that the surface temperature of the burning chars is absent for two cases, one case in Figure 7.2 (a) and one in (d), because the measured decay period was less than the calibration data. However, the surface temperature may be approximated at around 1400 K by extrapolating existing information from previous calibrations on the YAG:Tb phosphor in the literature [9].

7.2 Surface Temperature Measurements on a Down-Scaled Gas Turbine Combustor

The surface temperature of a burner nozzle in a down-scaled gas turbine combustor designed to simulate the Siemens DLE (Dry Low Emission) burner was measured using lifetime phosphor thermometry with the ZnS:Ag phosphor. The combustor operated with either methane or hydrogen-enriched methane (H_2/CH_4: 50/50 in volume %). The combustion chamber (Figure 7.3) was installed on top of a metal base plate with a truncated cone-shaped pilot nozzle in the center. The combustion chamber liner was composed of quartz to allow UV light to pass through.

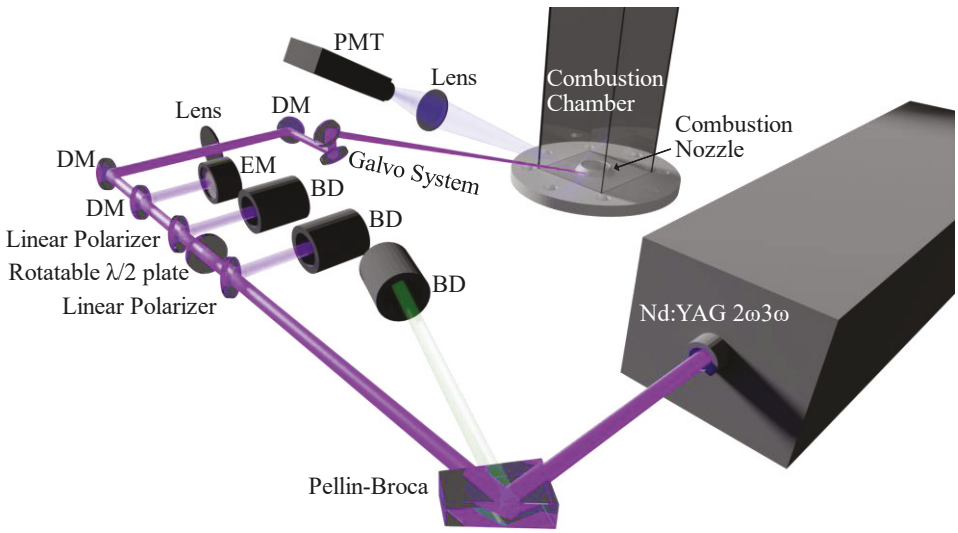

Figure 7.3: Phosphor thermometry setup. EM—Energy Meter, DM—Dichroic Mirror, BD—Beam Dump.

As shown in Figure 7.3, this work obtained surface-resolved temperatures by utilizing a galvo system to focus the excitation laser on different parts of the burner nozzle surface. A PMT was used to measure the phosphor's luminescence. The galvo system could scan the temperature measurement points throughout the burner's surface quickly and reproducibly. This allowed for many burner and pilot nozzle operating conditions without the need for cumbersome manual point-by-point temperature adjustments. As shown in Figure 7.4, the temperature was recorded at 33 separate spots on the nozzle surface, distributed at three different heights of the nozzle and across a quarter of the nozzle's circular sector. The signal-collection system was carefully designed so that all the nozzle measurement points could be imaged on the photocathode of the PMT. 50 decay curves were collected

at each measurement point. These decay curves were evaluated as single-shot data, and the average measured temperature is presented in Figure 7.4 and Figure 7.5.

The investigations for each fuel were carried out while the total amount of fuel and air fed into the combustion chamber remained constant and different percentages of air and fuel from the main were routed into the pilot. Figure 7.4 shows that the pilot flames are better connected to the nozzle for the H_2/CH_4 fuel (b) than for pure methane (a). This is due to hydrogen-enriched methane's wide flammability range, fast flame velocity, and hydrogen's strong diffusivity.

The local surface heating by the pilot flame for the H_2/CH_4 fuel can be seen in Figure 7.4 (b), where the surface temperatures in areas surrounding the fuel injectors are greater than those further away. The local surface heating with the pure CH_4 flame in Figure 7.4 (a) is small in comparison. The burner's lower heat output causes the lower overall temperature of the H_2/CH_4 fuel than with the CH_4 fuel. The H_2/CH_4/air mixtures has a lower equivalency ratio (0.52) and lower fueling rate (0.365 g/s) than the CH_4/air mixtures with an equivalence ratio of 0.72 and fueling rate of 0.567 g/s. This results in a thermal power of approximately 23 kW for the hydrogen-enriched methane fuel and 30 kW with the pure methane fuel.

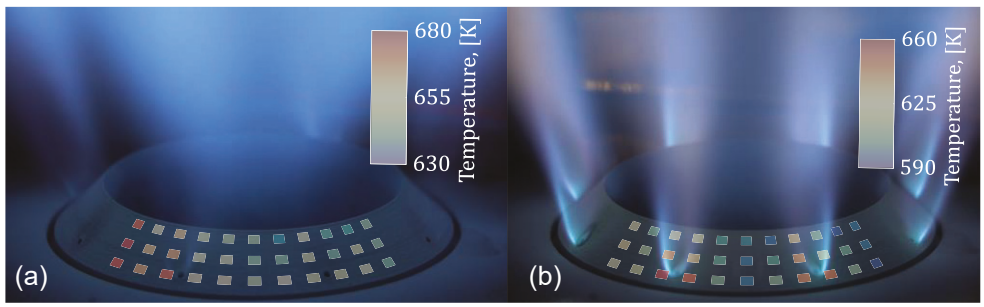

Figure 7.4: Time-averaged images of the combustion nozzle and measured surface temperature: Pilot injection strategy with 1 % of the total air flow and 6 % of the total fuel flow dedicated to the pilot injections for CH_4 (a) and H_2/CH_4 (b).

The surface temperature for the pilot injection strategy with 2 % of the total air flow and 2 % of the total fuel flow allocated to the pilot injections (Figure 7.5 (a)) is higher than the 2 % air and 6 % fuel for the pilots in Figure 7.5 (b). The H_2/CH_4 fuel was used in both pilot flow situations in Figure 7.5. The greater fuel flow rate in (b) than in (a) can explain the temperature difference, as the greater fuel flow rate results in longer mixing time requirements with the surrounding air. The longer mixing time in (b) than (a) results in longer pilot flames for (b). The long pilot flame length leads to less effective nozzle surface heating and lower surface temperatures, as seen in Figure 7.5.

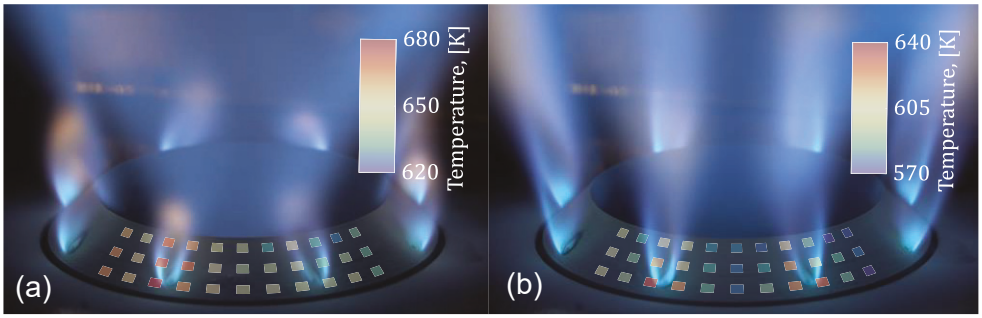

Figure 7.5: Time-averaged images of the combustion nozzle and measured surface temperature: Pilot injection strategy with 2 % of the total air flow and 2 % of the total fuel flow dedicated to the pilot injections in (a) and 2 % air and 6 % fuel for the pilots in (b) for H_2/CH_4 fuel.

H_2-enrichment of the methane fuel had two opposing effects on surface temperature. First, the lower equivalency ratio reduced flame temperature and heating from the main flame and lowered the surface temperatures. Second, the increased reactivity and diffusivity of H_2 aided in the attachment of pilot flames to pilot nozzles and supported an increase in nozzle surface temperature.

The balance between the cooling impact of the pilot air and fuel streams and the heating from the main and pilot flames determined the nozzle surface temperature. Because the pilot flames were not closely attached to the surface of the nozzle while using pure methane fuel, they delivered comparatively little local surface heating to the burner nozzle. With the H_2/CH_4 fuel the pilot flames were often more closely attached to the pilot nozzle leading to more local surface heating from the pilot flame.

8 Outlook

There are many potential avenues for future study within surface phosphor thermometry. The potential prospects suggested here are limited to the topics within this thesis's context.

The automated calibration procedure for high-temperature phosphor thermometry makes practical measurements on high-temperature surfaces (above 1600 K) very appealing and feasible. Also, demonstrating lifetime phosphor thermometry measurements above 2000 K would be a possible avenue for future work. Additionally, investigating cheaper experimental setups for high-temperature thermometry would be another avenue of development.

It would be interesting to investigate phosphors' decay time distribution changes due to excitation at a range of repetition rates, pulse durations [127], [138], and pulse power, as all these factors have been shown to affect the decay behavior of some phosphors. Additionally, acquiring the temperature-resolved decay time distribution of phosphors will allow more informed decisions on the fitting strategy for ascribing a single decay time to phosphors' decay. As has been shown in this thesis, analyzing the decay time distribution is an excellent tool to explain the decay time phenomenon better, as demonstrated in papers V, VII, VIII, and IX. This tool can surely be used in more contexts in the future.

With the upconversion lifetime phosphor thermometry study in paper IX, the next natural step is to apply the 8YSZ phosphors embedded in a TBC to validate their performance. Additionally, applying them in a system where temperature measurements beneath a TBC are attractive would be of great interest.

A study into the viability of using YVO_4:Tm and other phosphors as laser fluence sensors may be of interest. In paper V, YVO_4:Tm, at 400 K, was shown to have an approximately 40 times shorter lifetime when increasing the laser fluence from 0.01 mJ/cm^2 to 1 mJ/cm^2. Naturally, sensitivity around room temperature would be more attractive in this application, but the study did not investigate the sensitivity of phosphor luminescence to excitation pulse fluence at room temperature.

Performing more high-speed temperature measurements is of great interest and has become more commonplace in the phosphor thermometry community, as demonstrated by the reference in this thesis.

9 Acknowledgments

I look back at my time in the division of Combustion Physics with many fond memories, new experiences, and skills. First, I would like to thank my main supervisor Mattias Richter for his guidance throughout my PhD studies. The many informative and humorous team meetings were very enjoyable, and your hands-off approach allowed me a lot of liberty with my research within the confines of the research projects, which I am grateful for.

I would also like to thank everyone in Mattias Richter's research group, past and present, for all the intellectual and non-intellectual discussions that we have had. In particular, I would like to thank Christian Binder for introducing me to phosphor thermometry. I would also like to thank David Sanned for our fun discussions and our phosphor thermometry collaboration. Also, when Sebastian Nilsson joined the division in 2020, I gained a great colleague who not only made the phosphor thermometry work very productive but also very fun. I never knew that soldering connections pins to a trigger signal cable could be so much fun.

I have had two officemates since I started the division and I want to thank Elin Malmqvist for welcoming me to the division. It has also been fun sharing office space with Meena Raveesh for most of my time at the division, and hopefully, I was as welcoming to you as Elin was to me.

I would also like to thank Wubin Weng and Shen Li for our productive and fun collaboration with biomass combustion. Thanks to Arman Ahamed Subash and Francesco Pignatelli, working on the down-scaled gas turbine combustor was also fun and productive.

Per-Erik Bengtsson, I thank you for your work as head of the division; you provided a kind and productive work environment. I want to thank Minna Ramkull, Emelie Niléhn, and Cecilia Bille for helping me whenever issues arose and for all the times you helped me without me even knowing. Igor Buzuk, thank you for all your assistance over the years; you were always very helpful.

I also would like to give a very large thank you to Trivselgruppen for all the fun activities you hosted over the years.

10 References

[1] S. W. Allison and G. T. Gillies, “Remote thermometry with thermographic phosphors: Instrumentation and applications,” *Rev. Sci. Instrum.*, vol. 68, no. 7, pp. 2615–2650, 1997.

[2] International Energy Agency, “World Energy Statistics 2021,” Paris, 2021.

[3] International Energy Agency, “Net Zero by 2050,” Paris, 2021.

[4] A. W. Van Herwaarden and P. M. Sarro, “Thermal sensors based on the seebeck effect,” *Sensors and Actuators*, vol. 10, no. 3–4, pp. 321–346, 1986.

[5] S. Alaruri, L. Bianchini, and A. Brewington, “Effective spectral emissivity measurements of superalloys and YSZ thermal barrier coating at high temperatures using a 1.6 μm single wavelength pyrometer,” *Opt. Lasers Eng.*, vol. 30, no. 1–5, pp. 77–91, 1998.

[6] B. Kong, T. Li, and Q. Eri, “Normal spectral emissivity of GH536 (HastelloyX) in three surface conditions,” *Appl. Therm. Eng.*, vol. 113, pp. 20–26, 2017.

[7] C. Lempereur, R. Andral, and J. Y. Prudhomme, “Surface temperature measurement on engine components by means of irreversible thermal coatings,” *Meas. Sci. Technol.*, vol. 19, no. 10, 2008.

[8] H. Y. William M. Yen, Shigeo Shionoya, *Phosphor Handbook*, 2nd Editio. CRC Press, 2007.

[9] M. Aldén, A. Omrane, M. Richter, and G. Särner, “Thermographic phosphors for thermometry: A survey of combustion applications,” *Prog. Energy Combust. Sci.*, vol. 37, no. 4, pp. 422–461, 2011.

[10] M. D. Chambers and D. R. Clarke, “Doped Oxides for High-Temperature Luminescence and Lifetime Thermometry,” *Annu. Rev. Mater. Res.*, vol. 39, no. 1, pp. 325–359, 2009.

[11] J. Brübach, C. Pflitsch, A. Dreizler, and B. Atakan, “On surface temperature measurements with thermographic phosphors: A review,” *Prog. Energy Combust. Sci.*, vol. 39, no. 1, pp. 37–60, 2013.

[12] S. W. Allison, D. L. Beshears, M. R. Cates, M. B. Scudiere, D. W. Shaw, and A. D. Ellis, “Luminescence of YAG:Dy and YAG:Dy,Er crystals to 1700 °c,” *Meas. Sci. Technol.*, vol. 31, no. 4, 2020.

[13] M. R. Cates, D. L. Beshears, S. W. Allison, and C. M. Simmons, “Phosphor thermometry at cryogenic temperatures,” *Rev. Sci. Instrum.*, vol. 68, no. 6, pp. 2412–2417, 1997.

[14] C. P. Ding, R. Honza, B. Böhm, and A. Dreizler, “‘Simultaneous measurement of flame impingement and piston surface temperatures in an optically accessible spark

ignition engine,'" *Appl. Phys. B Lasers Opt.*, vol. 123, no. 4, pp. 1–11, 2017.

[15] T. P. Jenkins, C. F. Hess, S. W. Allison, and J. I. Eldridge, "Measurements of turbine blade temperature in an operating aero engine using thermographic phosphors," *Meas. Sci. Technol.*, vol. 31, no. 4, 2020.

[16] S. W. Allison, "A brief history of phosphor thermometry," *Meas. Sci. Technol.*, vol. 30, no. 7, p. 072001, 2019.

[17] M. H. V. Werts, "Making sense of lanthanide luminescence.," *Sci. Prog.*, vol. 88, no. Pt 2, pp. 101–131, 2005.

[18] G. H. Dieke, H. M. Crosswhite, and H. Crosswhite, *Spectra and Energy Levels of Rare Earth Ions in Crystals*. Interscience Publishers, 1968.

[19] W. T. Carnall, P. R. Fields, and B. G. Wybourne, "Spectral intensities of the trivalent lanthanides and actinides in solution. I. Pr3+, Nd3+, Er3+, Tm3+, and Yb8+ 1," *J. Chem. Phys.*, vol. 42, no. 11, pp. 3797–3806, 1965.

[20] W. T. Carnal, P. R. Fields, and K. Rajnak, "Electronic Energy Levels of the Trivalent Aquo Ions. I. Pr3+, Nd3+, Pm3+, Sm3+, Dy3+, Ho3+, Er3+, and Tm3+," *J. Chem. Phys.*, vol. 49, no. September, pp. 18–21, 1968.

[21] A. H. Khalid and K. Kontis, "Thermographic phosphors for high temperature measurements: Principles, current state of the art and recent applications," *Sensors*, vol. 8, no. 9, pp. 5673–5744, 2008.

[22] A. L. Heyes, "On the design of phosphors for high-temperature thermometry," *J. Lumin.*, vol. 129, no. 12, pp. 2004–2009, 2009.

[23] B. R. Judd, "Optical absorption intensities of rare-earth ions," *Phys. Rev.*, vol. 127, no. 3, pp. 750–761, 1962.

[24] G. S. Ofelt, "Intensities of crystal spectra of rare-earth ions," *J. Chem. Phys.*, vol. 37, no. 3, pp. 511–520, 1962.

[25] G. H. Dieke and H. M. Crosswhite, "The Spectra of the Doubly and Triply Ionized Rare Earths," *Appl. Opt.*, vol. 2, no. 7, pp. 675–686, 1963.

[26] M. Malinowski *et al.*, "Spectroscopic and laser properties of LiNbO3:Dy3+ crystals," *Acta Phys. Pol. A*, vol. 90, no. 1, pp. 181–189, 1996.

[27] S. Adachi, " Review—Mn 4+ -Activated Red and Deep Red-Emitting Phosphors ," *ECS J. Solid State Sci. Technol.*, vol. 9, no. 1, p. 016001, 2020.

[28] W. H. Fonger and C. W. Struck, "Eu +3 5D Resonance Quenching to the Charge-Transfer States in Y 20 2S, LazO 2S, and LaOCl," *J. Chem. Phys.*, vol. 52, no. 12, pp. 74–77, 1969.

[29] L. P. Goss, A. A. Smith, and M. E. Post, "Surface thermometry by laser-induced fluorescence," *Rev. Sci. Instrum.*, vol. 60, no. 3072, 1989.

[30] B. Fond, C. Abram, and F. Beyrau, "Characterisation of the luminescence properties of BAM:Eu2+ particles as a tracer for thermographic particle image velocimetry," *Appl. Phys. B Lasers Opt.*, vol. 121, no. 4, pp. 495–509, 2015.

[31] G. Särner, M. Richter, and M. Aldén, "Two-dimensional thermometry using temperature-induced line shifts of ZnO:Zn and ZnO:Ga fluorescence," *Opt. Lett.*, vol. 33, no. 12, p. 1327, 2008.

[32] C. D. S. Brites, S. Balabhadra, and L. D. Carlos, "Lanthanide-Based Thermometers:

At the Cutting-Edge of Luminescence Thermometry," *Adv. Opt. Mater.*, vol. 7, no. 5, pp. 1–30, 2019.

[33] A. O. Ojo, D. Escofet-Martin, J. Collins, G. Falconetti, and B. Peterson, "Experimental investigation of thermal boundary layers and associated heat loss for transient engine-relevant processes using HRCARS and phosphor thermometry," *Combust. Flame*, vol. 233, p. 111567, 2021.

[34] D. Witkowski and D. A. Rothamer, "Precise surface temperature measurements from 400 to 1200 K using the Pr:YAG phosphor," *Appl. Phys. B Lasers Opt.*, vol. 127, no. 12, pp. 1–10, 2021.

[35] P. Nau, Z. Yin, O. Lammel, and W. Meier, "Wall Temperature Measurements in Gas Turbine Combustors With Thermographic Phosphors," *J. Eng. Gas Turbines Power*, vol. 141, no. 4, pp. 1–9, 2019.

[36] H. Seyfried, G. Särner, A. Omrane, M. Richter, H. Schmidt, and M. Aldén, "Optical diagnostics for characterization of a full-size fighter-jet afterburner," in *Proceedings of the ASME Turbo Expo*, 2005, vol. 1, pp. 813–819.

[37] J. I. Eldridge and D. E. Wolfe, "Monitoring thermal barrier coating delamination progression by upconversion luminescence imaging," *Surf. Coat. Technol.*, vol. 378, no. August, p. 124923, 2019.

[38] J. I. Eldridge, S. W. Allison, T. P. Jenkins, S. L. Gollub, C. A. Hall, and D. G. Walker, "Surface temperature measurements from a stator vane doublet in a turbine afterburner flame using a YAG:Tm thermographic phosphor," *Meas. Sci. Technol.*, vol. 27, no. 12, 2016.

[39] A. O. Ojo, B. Fond, C. Abram, B. G. M. Van Wachem, A. L. Heyes, and F. Beyrau, "Thermographic laser Doppler velocimetry using the phase-shifted luminescence of BAM:Eu^2+ phosphor particles for thermometry," *Opt. Express*, vol. 25, no. 10, p. 11833, 2017.

[40] T. Cai, J. Han, M. Kim, and K. C. Kim, "Two-dimensional lifetime-based kHz surface temperature measurement technique using phosphor thermometry," *Appl. Phys. Lett.*, vol. 119, no. 24, 2021.

[41] S. V. Yap, R. M. Ranson, W. M. Cranton, and D. Koutsogeorgis, "Decay time characteristics of La2O2S:Eu and La2O2S:Tb for use within an optical sensor for human skin temperature measurement," *Appl. Opt.*, vol. 47, no. 27, pp. 4895–4899, 2008.

[42] C. M. Arndt, P. Nau, and W. Meier, "Characterization of wall temperature distributions in a gas turbine model combustor measured by 2D phosphor thermometry," *Proc. Combust. Inst.*, vol. 38, no. 1, pp. 1867–1875, 2021.

[43] T. Cai, D. Kim, M. Kim, Y. Z. Liu, and K. C. Kim, "Two-dimensional thermographic phosphor thermometry in a cryogenic environment," *Meas. Sci. Technol.*, vol. 28, no. 1, 2017.

[44] T. Kissel, E. Baum, A. Dreizler, and J. Brübach, "Two-dimensional thermographic phosphor thermometry using a CMOS high speed camera system," *Appl. Phys. B Lasers Opt.*, vol. 96, no. 4, pp. 731–734, 2009.

[45] A. Omrane, F. Ossler, and M. Aldén, "Two-Dimensional Surface Temperature Measurements of Burning Materials," *Proc. Combust. Inst.*, vol. 29, no. 2, pp. 2653–

2659, 2002.

[46] D. Peng, Y. Liu, X. Zhao, and K. C. Kim, “Comparison of lifetime-based methods for 2D phosphor thermometry in high-temperature environment,” *Meas. Sci. Technol.*, vol. 27, no. 9, 2016.

[47] A. O. Ojo, D. Escofet-Martin, and B. Peterson, “High-precision 2D surface phosphor thermometry at kHz-rates during flame-wall interaction in narrow passages,” *Proc. Combust. Inst.*, vol. 000, pp. 1–9, 2022.

[48] B. Heeg, “Precision of mono-exponential decay estimates from rapid lifetime determination in the presence of signal photon and background noise,” *Meas. Sci. Technol.*, vol. 25, no. 10, 2014.

[49] E. Hertle, L. Chepyga, M. Batentschuk, and L. Zigan, “Influence of codoping on the luminescence properties of YAG:Dy for high temperature phosphor thermometry,” *J. Lumin.*, vol. 182, pp. 200–207, 2017.

[50] N. Ishiwada, K. Tsuchiya, and T. Yokomori, “Applicability of Dy-doped yttrium aluminum garnet (YAG:Dy) in phosphor thermometry at different oxygen concentrations,” *J. Lumin.*, vol. 208, no. July 2018, pp. 82–88, 2019.

[51] N. Fuhrmann, J. Brübach, and A. Dreizler, “Spectral decomposition of phosphorescence decays,” *Rev. Sci. Instrum.*, vol. 84, no. 11, pp. 4–9, 2013.

[52] R. J. Woods, S. Scypinski, L. J. Cline Love, and H. A. Ashworth, “Transient Digitizer for the Determination of Microsecond Luminescence Lifetimes,” *Anal. Chem.*, vol. 56, no. 8, pp. 1395–1400, 1984.

[53] R. M. Ballew and J. N. Demas, “Error analysis of the rapid lifetime determination method for single exponential decays with a non-zero baseline,” *Anal. Chim. Acta*, vol. 245, no. C, pp. 121–127, 1991.

[54] J. Brübach, J. Janicka, and A. Dreizler, “An algorithm for the characterisation of multi-exponential decay curves,” *Opt. Lasers Eng.*, vol. 47, no. 1, pp. 75–79, 2009.

[55] N. Fuhrmann, J. Brübach, and A. Dreizler, “On the mono-exponential fitting of phosphorescence decays,” *Appl. Phys. B Lasers Opt.*, vol. 116, no. 2, pp. 359–369, 2014.

[56] A. Mendieta, B. Fond, P. Dragomirov, and F. Beyrau, “A delayed gating approach for interference-free ratio-based phosphor thermometry,” *Meas. Sci. Technol.*, no. April, 2019.

[57] N. Fuhrmann, J. Brübach, and A. Dreizler, “Phosphor thermometry: A comparison of the luminescence lifetime and the intensity ratio approach,” *Proc. Combust. Inst.*, vol. 34, no. 2, pp. 3611–3618, 2013.

[58] S. Petit, P. Xavier, G. Godard, and F. Grisch, “Improving the temperature uncertainty of Mg4FGeO6:Mn4 + ratio-based phosphor thermometry by using a multi-objective optimization procedure,” *Appl. Phys. B*, vol. 128, no. 3, p. 57, 2022.

[59] E. M. C. Jones, A. R. Jones, K. N. G. Hoffmeister, and C. Winters, “Advances in phosphor two-color ratio method thermography for full-field surface temperature measurements,” *Meas. Sci. Technol.*, vol. 33, no. 8, p. 85201, May 2022.

[60] B. R. Anderson, S. Livers, R. Gunawidjaja, and H. Eilers, “Fiber-based optical thermocouples for fast temperature sensing in extreme environments sensing in

extreme environments," *Opt. Eng.*, vol. 58, no. 9, 2019.

[61] J. Brübach, J. P. Feist, and A. Dreizler, "Characterization of manganese-activated magnesium fluorogermanate with regards to thermographic phosphor thermometry," *Meas. Sci. Technol.*, vol. 19, no. 2, 2008.

[62] M. Cates, S. W. Allison, S. Jaiswal, and S. Beshears, "YAG:Dy and YAG:Tm Fluorescence Above 1400 C," *Proc Int Instrum Symp 2003*, no. August 2014, p. 49:447~58, 2003.

[63] F. A. Nada, C. Knappe, X. Xu, M. Richter, and M. Aldén, "Development of an automatic routine for calibration of thermographic phosphors," *Meas. Sci. Technol.*, vol. 25, no. 2, 2014.

[64] H. Feuk and S. Nilsson, "Lifetime Surface Phosphor Thermometry MATLAB Code," *10-Feb-2023*. [Online]. Available: osf.io/xtzn4.

[65] A. A. Istratov and O. F. Vyvenko, "Exponential analysis in physical phenomena," *Rev. Sci. Instrum.*, vol. 70, no. 2, pp. 1233–1257, 1999.

[66] R. Esposito, C. Altucci, and R. Velotta, "Analysis of simulated fluorescence intensities decays by a new Maximum Entropy Method algorithm," *J. Fluoresc.*, vol. 23, no. 1, pp. 203–211, 2013.

[67] R. Esposito, G. Mensitieri, and S. De Nicola, "Improved maximum entropy method for the analysis of fluorescence spectroscopy data: Evaluating zero-time shift and assessing its effect on the determination of fluorescence lifetimes," *Analyst*, vol. 140, no. 24, pp. 8138–8147, 2015.

[68] N. S. Cheruvu, K. S. Chan, and R. Viswanathan, "Evaluation, degradation and life assessment of coatings for land based combustion turbines," *Energy Mater.*, vol. 1, no. 1, pp. 33–47, 2006.

[69] A. Yañez Gonzalez *et al.*, "Temperature sensing inside thermal barrier coatings using phosphor thermometry," *IET Conf. Publ.*, vol. 2014, no. 630 CP, 2014.

[70] M. M. Gentleman, V. Lughi, A. J. Nychka, and R. D. Clarke, "Noncontact Methods for Measuring Thermal Barrier Coating Temperatures," *Int. J. Appl. Ceram. Technol.*, vol. 3, no. 2, pp. 105–112, 2006.

[71] F. Abou Nada, A. Lantz, J. Larfeldt, N. Markocsan, M. Aldén, and M. Richter, "Remote temperature sensing on and beneath atmospheric plasma sprayed thermal barrier coatings using thermographic phosphors," *Surf. Coatings Technol.*, vol. 302, pp. 359–367, 2016.

[72] J. P. Feist and A. L. Heyes, "Photo-stimulated phosphorescence for thermal condition monitoring and nondestructive evaluation in thermal barrier coatings," *Heat Transf. Eng.*, vol. 30, no. 13, pp. 1087–1095, 2009.

[73] R. J. L. Steenbakker, J. P. Feist, R. G. Wellman, and J. R. Nicholls, "Sensor thermal barrier coatings: Remote in situ condition monitoring of EB-PVD coatings at elevated temperatures," *J. Eng. Gas Turbines Power*, vol. 131, no. 4, pp. 1–9, 2009.

[74] M. M. Gentleman, J. I. Eldridge, D. M. Zhu, K. S. Murphy, and D. R. Clarke, "Non-contact sensing of TBC/BC interface temperature in a thermal gradient," *Surf. Coatings Technol.*, vol. 201, no. 7 SPEC. ISS., pp. 3937–3941, 2006.

[75] Y. K. Voron'ko *et al.*, "Spectroscopy of Yb3+ in Cubic ZrO2 Crystals," *Inorg.*

Mater., vol. 40, no. 5, pp. 502–508, 2004.

[76] D. Wang, W. Wu, X. Tan, B. A. Goodman, S. Xu, and W. Deng, "Upconversion visible light emission in yb/pr co-doped yttria-stabilized zirconia (Ysz) single crystals," *Crystals*, vol. 11, no. 11, 2021.

[77] X. Wang, X. Tan, S. Xu, F. Liu, B. A. Goodman, and W. Deng, "Preparation and up-conversion luminescence of Er-doped yttria stabilized zirconia single crystals," *J. Lumin.*, vol. 219, no. November 2019, 2020.

[78] T. Wei *et al.*, "Optical spectroscopy and population behavior between ^4I_11/2 and ^4I_13/2 levels of erbium doped germanate glass," *Opt. Mater. Express*, vol. 4, no. 10, p. 2150, 2014.

[79] F. Huang, X. Liu, Y. Ma, S. Kang, L. Hu, and D. Chen, "Origin of near to middle infrared luminescence and energy transfer process of Er3+/Yb3+ co-doped fluorotellurite glasses under different excitations," *Sci. Rep.*, vol. 5, pp. 5–10, 2015.

[80] K. Pavani *et al.*, "Highly efficient upconversion of Er3+ in Yb3+ codoped non-cytotoxic strontium lanthanum aluminate phosphor for low temperature sensors," *Sci. Rep.*, vol. 7, no. 1, pp. 1–15, 2017.

[81] D. Gao, X. Zhang, and W. Gao, "Tuning upconversion emission by controlling particle shape in NaYF 4:Yb 3+/Er 3+ nanocrystals," *J. Appl. Phys.*, vol. 111, no. 3, pp. 3–8, 2012.

[82] X. Wang, Y. Bu, S. Xiao, X. Yang, and J. W. Ding, "Upconversion in Ho3+-doped YbF3 particle prepared by coprecipitation method," *Appl. Phys. B Lasers Opt.*, vol. 93, no. 4, pp. 801–807, 2008.

[83] D. Przybylska, A. Ekner-Grzyb, B. F. Grześkowiak, and T. Grzyb, "Upconverting SrF2 nanoparticles doped with Yb3+/Ho3+, Yb3+/Er3+ and Yb3+/Tm3+ ions – optimisation of synthesis method, structural, spectroscopic and cytotoxicity studies," *Sci. Rep.*, vol. 9, no. 1, pp. 1–12, 2019.

[84] S. R. Lüthi, M. Pollnau, H. U. Güdel, and M. P. Hehlen, " Near-infrared to visible upconversion in Er3+ -doped Cs3Lu2Cl9, Cs3Lu2Br9, and Cs3Y2I9 excited at 1.54 μm ," *Phys. Rev. B*, vol. 60, no. 1, pp. 162–178, 1999.

[85] C. C. Pilgrim, J. P. Feist, and a L. Heyes, "On the effect of temperature gradients and coating translucence on the accuracy of phosphor thermometry," *Meas. Sci. Technol.*, vol. 24, no. 10, p. 105201, 2013.

[86] Q. Fouliard, S. Haldar, R. Ghosh, and S. Raghavan, "Modeling luminescence behavior for phosphor thermometry applied to doped thermal barrier coating configurations," *Appl. Opt.*, vol. 58, no. 13, p. D68, 2019.

[87] Q. Fouliard, J. Hernandez, and M. Northam, "Doped 8 % Yttria-Stabilized Zirconia for Temperature Measurements in Thermal Barrier Coatings using Phosphor Thermometry," in *AIAA 2020-0631 Session: Turbines I*, 2020, no. January.

[88] G. Yang and C. Y. Zhao, "A comparative experimental study on radiative properties of EB-PVD and air plasma sprayed thermal barrier coatings," *J. Heat Transfer*, vol. 137, no. 9, 2015.

[89] J. I. Eldridge, "Determination of Scattering and Absorption Coefficients for Plasma-Sprayed Yttria-Stabilized Zirconia Thermal Barrier Coatings," *J. Am. Ceram. Soc.*, vol. 91, no. 5, pp. 1603–1611, 2008.

[90] F. Blanchard *et al.*, “A comparative study of the optical and microstructural properties of suspension and atmospheric plasma sprayed thermal barrier coatings,” *Surf. Coatings Technol.*, vol. 449, no. October, 2022.

[91] A. L. Heyes, S. Seefeldt, and J. P. Feist, “Two-colour phosphor thermometry for surface temperature measurement,” *Opt. Laser Technol.*, vol. 38, no. 4–6, pp. 257–265, 2006.

[92] A. Hashemi, A. Vetter, G. Jovicic, M. Batentschuk, and C. J. Brabec, “Temperature measurements using YAG : Dy and YAG : Sm under diode laser excitation (405 nm),” *Meas. Sci. Technol.*, vol. 26, no. 7, 2015.

[93] G. Jovicic, L. Zigan, S. Will, and A. Leipertz, “Luminescence properties of the thermographic phosphors Dy3+:YAG and Tm3+:YAG for the application in high temperature systems,” *Zeitschrift fur Phys. Chemie*, vol. 229, no. 6, pp. 977–997, 2015.

[94] N. Neal, J. Jordan, and D. Rothamer, “Simultaneous Measurements of In-Cylinder Temperature and Velocity Distribution in a Small-Bore Diesel Engine Using Thermographic Phosphors,” *SAE Int. J. Engines*, vol. 6, no. 1, pp. 300–318, 2013.

[95] J. Jordan and D. A. Rothamer, “Pr:YAG temperature imaging in gas-phase flows,” *Appl. Phys. B Lasers Opt.*, vol. 110, no. 3, pp. 285–291, 2013.

[96] A. R. Regmi, S. W. Allison, K. Olenick, and F. Sabri, “High temperature phosphor thermometry with YAG: Dy and LED excitation on flexible YSZ ceramic ribbons,” *MRS Commun.*, vol. 11, no. 3, pp. 322–329, 2021.

[97] P. Nau, S. Görs, C. Arndt, B. Witzel, and T. Endres, “Wall temperature measurements in a full-scale gas turbine combustor test rig with fiber coupled phosphor thermometry,” *J. Turbomach.*, vol. 143, no. 1, pp. 1–7, 2021.

[98] M. Prokić, “Effect of lithium co-dopant on the thermoluminescence response of some phosphors,” *Appl. Radiat. Isot.*, vol. 52, no. 1, pp. 97–103, 2000.

[99] W. Y. Kwong, A. Steinberg, and Y. H. Chin, “Effect of B^3+-N^3− on YAG:Dy thermographic phosphor luminescence,” *Opt. Lett.*, vol. 39, no. 21, p. 6166, 2014.

[100] L. M. Chepyga, G. Jovicic, A. Vetter, A. Osvet, C. J. Brabec, and M. Batentschuk, “Photoluminescence properties of thermographic phosphors YAG:Dy and YAG:Dy, Er doped with boron and nitrogen,” *Appl. Phys. B Lasers Opt.*, vol. 122, no. 8, pp. 1–10, 2016.

[101] J. Li, J. G. Li, S. Liu, X. Li, X. Sun, and Y. Sakka, “Greatly enhanced Dy3+ emission via efficient energy transfer in gadolinium aluminate garnet (Gd3Al5O12) stabilized with Lu3+,” *J. Mater. Chem. C*, vol. 1, no. 45, pp. 7614–7622, 2013.

[102] E. Hertle, L. Chepyga, M. Batentschuk, S. Will, and L. Zigan, “Temperature-dependent luminescence characteristics of Dy3+ doped in various crystalline hosts,” *J. Lumin.*, vol. 204, no. March, pp. 64–74, 2018.

[103] T. V. Gavrilović, D. J. Jovanović, V. M. Lojpur, V. Dordević, and M. D. Dramićanin, “Enhancement of luminescence emission from GdVO4:Er 3+/Yb3+ phosphor by Li+ co-doping,” *J. Solid State Chem.*, vol. 217, pp. 92–98, 2014.

[104] D. Avram, B. Cojocaru, I. Tiseanu, M. Florea, and C. Tiseanu, “Down-/Up-Conversion Emission Enhancement by Li Addition: Improved Crystallization or Local Structure Distortion?,” *J. Phys. Chem. C*, vol. 121, no. 26, pp. 14274–14284,

2017.

[105] D. Avram, I. Tiseanu, B. S. Vasile, M. Florea, and C. Tiseanu, “Near infrared emission properties of Er doped cubic sesquioxides in the second/third biological windows,” *Sci. Rep.*, vol. 8, no. 1, pp. 1–12, 2018.

[106] L. M. Chepyga, A. Osvet, C. J. Brabec, and M. Batentschuk, “High-temperature thermographic phosphor mixture YAP/YAG:Dy3+ and its photoluminescence properties,” *J. Lumin.*, vol. 188, no. December 2016, pp. 582–588, 2017.

[107] J. P. Feist, A. L. Heyes, and S. Seefeldt, “Oxygen quenching of phosphorescence from thermographic phosphors,” *Meas. Sci. Technol.*, vol. 14, no. 5, pp. N17–N20, 2003.

[108] Y. Li *et al.*, “Effect of oxygen partial pressure on the phosphorescence of different lanthanide ion (Ln3+)-doped yttria-stabilised zirconia,” *Sensors Actuators, B Chem.*, vol. 308, no. January, p. 127666, 2020.

[109] L. Yang *et al.*, “‘Oxygen quenching’ in Eu-based thermographic phosphors: Mechanism and potential application in oxygen/pressure sensing,” *Sensors Actuators, B Chem.*, vol. 254, pp. 578–587, 2018.

[110] T. Cai, J. Jung, D. Li, M. Kim, C. H. Jeon, and K. C. Kim, “Simultaneous sensing of oxygen concentration and temperature utilizing rise and decay of the phosphorescence of Y2O3:Eu3+ in high-temperature environments,” *Sensors Actuators B Chem.*, vol. 370, no. May, 2022.

[111] C. Knappe, J. Lindén, F. Abou Nada, M. Richter, and M. Aldén, “Investigation and compensation of the nonlinear response in photomultiplier tubes for quantitative single-shot measurements,” *Rev. Sci. Instrum.*, vol. 83, no. 3, 2012.

[112] C. Knappe, F. A. Nada, M. Richter, and M. Aldén, “Comparison of photo detectors and operating conditions for decay time determination in phosphor thermometry,” *Rev. Sci. Instrum.*, vol. 83, no. 9, 2012.

[113] F. Abou Nada, C. Knappe, M. Aldén, and M. Richter, “Improved measurement precision in decay time-based phosphor thermometry,” *Appl. Phys. B Lasers Opt.*, vol. 122, no. 6, pp. 1–12, 2016.

[114] N. Fuhrmann, E. Baum, J. Brübach, and A. Dreizler, “High-speed phosphor thermometry,” *Rev. Sci. Instrum.*, vol. 82, no. 10, 2011.

[115] D. H. Hartman, “Pulse mode saturation properties of photomultiplier tubes,” *Rev. Sci. Instrum.*, vol. 49, no. 8, pp. 1130–1133, 1978.

[116] R. L. Vander Wal, P. A. Householder, and T. W. Wright, “Phosphor thermometry in combustion applications,” *Appl. Spectrosc.*, vol. 53, no. 10, pp. 1251–1258, 1999.

[117] L. Yan, Y. Song, W. Liu, Z. Lv, and Y. Yang, “Phosphor thermometry at 5 kHz rate using a high-speed fiber-optic spectrometer,” *J. Appl. Phys.*, vol. 127, no. 12, 2020.

[118] N. Fuhrmann, C. Litterscheid, C.-P. Ding, J. Brübach, B. Albert, and A. Dreizler, “Cylinder head temperature determination using high-speed phosphor thermometry in a fired internal combustion engine,” *Appl. Phys. B*, vol. 116, no. 2, pp. 293–303, 2014.

[119] R. W. K. Leung, S.-C. A. Yeh, and Q. Fang, “Effects of incomplete decay in fluorescence lifetime estimation,” *Biomed. Opt. Express*, vol. 2, no. 9, p. 2517, 2011.

[120] Hamamatsu Photonics K. K., *Photomultiplier Tubes - Basics and Application*, 3a ed. Hamamatsu Photonics K. K., 2017.

[121] H. Feuk, D. Sanned, M. Richter, and M. Aldén, "Sources of error for single-shot PMT-based phosphor thermometry in harsh conditions," *Meas. Sci. Technol.*, vol. 32, no. 8, 2021.

[122] D. Witkowski and D. A. Rothamer, "Evaluation of 15-kHz high-speed Pr: YAG phosphor surface thermometry of a thermal barrier coating in a reciprocating IC engine," *Proc. Combust. Inst.*, vol. 000, pp. 1–9, 2022.

[123] A. O. Ojo, D. Escofet-Martin, C. Abram, B. Fond, and B. Peterson, "Precise surface temperature measurements at kHz-rates using phosphor thermometry to study flame-wall interactions in narrow passages," *Combust. Flame*, vol. 240, p. 111984, 2022.

[124] J. Lindén, N. Takada, B. Johansson, M. Richter, and M. Aldén, "Investigation of potential laser-induced heating effects when using thermographic phosphors for gas-phase thermometry," *Appl. Phys. B Lasers Opt.*, vol. 96, no. 2–3, pp. 237–240, 2009.

[125] C. Abram, B. Fond, and F. Beyrau, "High-precision flow temperature imaging using ZnO thermographic phosphor tracer particles," *Opt. Express*, vol. 23, no. 15, p. 19453, 2015.

[126] B. Fond, C. Abram, A. L. Heyes, A. M. Kempf, and F. Beyrau, "Simultaneous temperature, mixture fraction and velocity imaging in turbulent flows using thermographic phosphor tracer particles," *Opt. Express*, vol. 20, no. 20, p. 22118, 2012.

[127] S. W. Allison, "On the role of excitation pulse duration on luminescence measurements," *Meas. Sci. Technol.*, vol. 32, no. 6, 2021.

[128] W. Weng *et al.*, "Quantitative Measurement of Atomic Potassium in Plumes over Burning Solid Fuels Using Infrared-Diode Laser Spectroscopy," *Energy and Fuels*, vol. 31, no. 3, pp. 2831–2837, 2017.

[129] D. Hot, R. L. Pedersen, W. Weng, Y. Zhang, M. Aldén, and Z. Li, "Spatially and temporally resolved IR-DFWM measurement of HCN released from gasification of biomass pellets," *Proc. Combust. Inst.*, vol. 37, no. 2, pp. 1337–1344, 2019.

[130] Y. Liu *et al.*, "Measurement and kinetics of elemental and atomic potassium release from a burning biomass pellet," *Proc. Combust. Inst.*, vol. 37, no. 3, pp. 2681–2688, 2019.

[131] H. Fatehi and X. S. Bai, "A comprehensive mathematical model for biomass combustion," *Combust. Sci. Technol.*, vol. 186, no. 4–5, pp. 574–593, 2014.

[132] H. Lu, W. Robert, G. Peirce, B. Ripa, and L. L. Baxter, "Comprehensive study of biomass particle combustion," *Energy and Fuels*, vol. 22, no. 4, pp. 2826–2839, 2008.

[133] J. T. Kuo and C. L. Hsi, "Pyrolysis and ignition of single wooden spheres heated in high-temperature streams of air," *Combust. Flame*, vol. 142, no. 4, pp. 401–412, 2005.

[134] W. C. Park, A. Atreya, and H. R. Baum, "Experimental and theoretical investigation of heat and mass transfer processes during wood pyrolysis," *Combust. Flame*, vol. 157, no. 3, pp. 481–494, 2010.

[135] W. Weng, J. Borggren, B. Li, M. Aldén, and Z. Li, “A novel multi-jet burner for hot flue gases of wide range of temperatures and compositions for optical diagnostics of solid fuels gasification/combustion,” *Rev. Sci. Instrum.*, vol. 88, no. 4, 2017.

[136] J. Borggren, W. Weng, A. Hosseinnia, P. E. Bengtsson, M. Aldén, and Z. Li, “Diode laser-based thermometry using two-line atomic fluorescence of indium and gallium,” *Appl. Phys. B Lasers Opt.*, vol. 123, no. 12, pp. 1–10, 2017.

[137] W. J. Liu, W. W. Li, H. Jiang, and H. Q. Yu, “Fates of Chemical Elements in Biomass during Its Pyrolysis,” *Chem. Rev.*, vol. 117, no. 9, pp. 6367–6398, 2017.

[138] T. Cai, B. Chen, J. Han, M. Kim, E. Yeom, and K. C. Kim, “Effect of excitation duration on phosphorescence decay and analysis of its mechanisms,” *J. Lumin.*, vol. 252, no. May, p. 119423, 2022.

11 Summary of Papers

Paper I: Temporal temperature measurement on burning biomass pellets using phosphor thermometry and two-line atomic fluorescence

W. Weng, H. Feuk, S. Li, M. Richter, M. Aldén, and Z. Li.

This paper investigated the temporal behavior of burning biomass pellets with surface phosphor thermometry, two-line atomic fluorescence, and polycyclic aromatic hydrocarbons fluorescence. For the first time, the surface temperature of burning biomass pellets was measured with phosphor thermometry. The result showed that during the devolatilization stage, the surface temperature of the burning biomass pellets was approximately 700 K. The surface temperature increased rapidly during char conversion, but the surface temperature was still approximately 500 K lower than the hot gas environment.

I performed the phosphor thermometry measurements in the study, wrote the text, and did the data analysis for the phosphor thermometry measurements. I also contributed to the editing of the manuscript. Additionally, I presented the work at the online 2020 Combustion Institute Conference.

Paper II: Sources of error for single-shot PMT-based phosphor thermometry in harsh conditions

H. Feuk, D. Sanned, M. Richter, and M. Aldén.

The practical implications of detector nonlinearity of PMT-based lifetime phosphor thermometry measurements were evaluated with a range of phosphor decay times. This investigation aimed to see how phosphorescence intensity changes could lead to temperature measurement errors for a range of decay times. The study also investigated these factors with different detector gains and arrived at some general guidelines and methodologies to reduce and assess detector linearity.

I initiated the study to address knowledge gaps from previous studies of detector nonlinearities. I led the experimental activities which David and I conducted. Additionally, I did all the data analysis, data visualization, and I wrote the manuscript.

Paper III: Investigating photomultiplier tube nonlinearities in high-speed phosphor thermometry using light emitting diode simulated decay curves

H. Feuk, S. Nilsson, M. Aldén, M. Richter.

This paper was a continuation of Paper II in the context of high-speed phosphor thermometry. However, instead of using phosphor luminescence like Paper II, an LED was used to simulate different phosphor decay times and repetition rates of the luminescence signal. Using an LED had the benefit of quickly adjusting the repetition rate of the luminescence signal from 1 Hz to 10 kHz to enable studying PMT nonlinearities. The peak signal linearity was generally poor in the kHz repetition rate regime, but the impact on measured decay time was relatively minor. Using a gateable photocathode PMT in situations with a strong luminous background improved detector linearity at lower repetition rates, but at higher repetition rates above 1 kHz, when the gate is open for a longer fraction of the time, the linearity worsened.

I initiated the study to investigate detector nonlinearities relevant to high-speed lifetime phosphor thermometry measurements with a PMT. I performed all the experimental activities. I did all the data analysis, data visualization, and I wrote the manuscript.

Paper IV: Automated phosphor thermometry lifetime calibration of multiple phosphors and emission lines to above 1900 K

H. Feuk, S. Nilsson, and M. Richter

An automated procedure to calibrate multiple phosphors and emission lines simultaneously to temperatures above 1900 K was described. It was also the first time to the authors' knowledge the surface-coated phosphors were calibrated to over 1900 K. The potential calibration errors caused by the calibration procedure were evaluated.

Sebastian and I initiated the study together and conducted the experimental activities together. I did the data evaluation and data visualization. Sebastian made the experimental setup figure. I wrote the algorithm used to automate the data collection and I wrote the manuscript.

Paper V: Laser excitation effects in lifetime-based high-speed phosphor thermometry

H. Feuk, S. Nilsson, and M. Richter,

This paper was a continuation of Paper III. After investigating detector effects relevant to high-speed phosphor thermometry, potential sources of error due to laser excitation effects were investigated. Two phosphors, Mg_3FGeO_6:Mn (MFG) and YVO_4:Tm were used, and significant decay time measurement errors can occur for both phosphors. The dominant factor in measured decay time changes was laser irradiance for MFG and laser fluence for YVO_4:Tm.

I initiated the study. Sebastian and I did the experimental activities together. I did all the data evaluation and all figures. I wrote the manuscript.

Paper VI: Impact of Methane and Hydrogen-Enriched Methane Pilot Injection on the Surface Temperature of a Scaled-Down Burner Nozzle Measured Using Phosphor Thermometry

H. Feuk, F. Pignatelli, A. Subash, R. Bi, R. Szász, X. Bai, D. Lörstad, and M. Richter

Phosphor thermometry measurements were conducted on the combustion nozzle of a down-scaled gas turbine combustor with hydrogen-enriched methane (H_2/CH_4: 50/50 in volume %) and methane fuels. The surface temperature of the combustion nozzle with different pilot injection hardware, airflow, and fuel flow was investigated. In addition, OH LIF and flame luminosity images were acquired to couple the flame structure with the measured surface temperatures.

Arman, Francesco, Ruike, and I conducted the phosphor thermometry measurements together. I did all the data analysis for the phosphor thermometry measurements, and Francesco did the data analysis for the OH PLIF probability maps. I did all the data visualization. I did all the figures except Figure 1, which Francesco made. I wrote the manuscript except for the parts of the introduction and method sections that are not about phosphor thermometry.

Paper VII: High Temperature Thermographic Phosphors YAG:Tm,Li and YAG:Dy in Reduced Oxygen Environments

S. Nilsson, H. Feuk, and M. Richter

YAG:Tm,Li, and YAG:Dy were characterized for phosphor thermometry for high surface temperature measurements to temperatures over 1900 K. Sensitivity of the phosphors YAG:Dy and YAG:Tm,Li to gas oxygen environment was studied. Additionally, strategies were presented to reduce temperature measurement errors due to the oxygen gas environment. YAG:Tm,Li was found to be a very promising candidate for high-temperature phosphor thermometry.

Sebastian initiated the study. We conducted the experimental activities together. I wrote the algorithm for data collection. Sebastian did all data analysis except for the results based on the Maximum Entropy Method (MEM) analysis which I did. Sebastian made all figures and all the data visualization. Sebastian wrote the manuscript.

Paper VIII: Temperature Resolved Decay Time Components of Mg_4FGeO_6:Mn using the Maximum Entropy Method

H. Feuk, S. Nilsson, and M. Richter

The temperature-resolved decay time distribution of Mg_4FGeO_6:Mn was presented with and without a background luminescence signal. It was demonstrated that MEM could characterize the luminescence decay from two luminescent sources simultaneously. One can use the decay time distribution for thermometry, but the

main benefit of the MEM is that it can separate the various decay components of a decay signal, allowing a more in-depth analysis of decays.

Sebastian and I initiated the study. We conducted the experimental activities together. I wrote the algorithm for data collection and did the data analysis and data visualization. I made all the figures. Sebastian wrote the section about the Maximum Entropy Method, and I wrote the rest of the manuscript.

Paper IX: Upconversion Phosphor Thermometry for use in Thermal Barrier Coatings

H. Feuk, S. Nilsson, and M. Richter

The phosphors YSZ:Er,Yb and YSZ:Ho,Yb were characterized with both upconversion and downconversion luminescence. The phosphor characteristics were used in a Kubelka-Munk simulation to compare signal strength between the two phosphors and YSZ:Er. Up-conversion lifetime phosphor thermometry was shown to be promising for temperature measurements in an embedded phosphor-doped YSZ layer owing to the increased temperature sensitivity, reduced fluorescence background influence, and competitive signal strength.

I initiated the study. I conducted all the experimental activities. I did all data analysis, all data visualizations, and all figures. I wrote the manuscript.